Development of a High-Throughput Test System for Continuous Electrolysis Processes

Von der Fakultät für Mathematik und Naturwissenschaften der RWTH Aachen University
zur Erlangung des akademischen Grades eines
Doktors der Ingenieurwissenschaften genehmigte Dissertation

vorgelegt von

Deniz Dogan, M.Sc.

aus

Düsseldorf

Berichter: Univ.-Prof. Dr. rer. nat. Rüdiger-Albert Eichel

Univ.-Prof. Dr. rer. nat. Anna Mechler

Univ.-Prof. Dr. rer. nat. Marcellus Liauw

Tag der mündlichen Prüfung: 02.10.2025

Diese Dissertation ist auf den Internetseiten der Universitätsbibliothek verfügbar.

Eidesstattliche Erklärung

Ich, Deniz Dogan erkläre hiermit, dass diese Dissertation und die darin dargelegten Inhalte die eigenen sind und selbstständig, als Ergebnis der eigenen originären Forschung, generiert wurden.

Hiermit erkläre ich an Eides statt

1. Diese Arbeit wurde vollständig oder größtenteils in der Phase als Doktorand dieser Fakultät und Universität angefertigt;

2. Sofern irgendein Bestandteil dieser Dissertation zuvor für einen akademischen Abschluss oder eine andere Qualifikation an dieser oder einer anderen Institution verwendet wurde, wurde dies klar angezeigt;

3. Wenn immer andere eigene- oder Veröffentlichungen Dritter herangezogen wurden, wurden diese klar benannt;

4. Wenn aus anderen eigenen- oder Veröffentlichungen Dritter zitiert wurde, wurde stets die Quelle hierfür angegeben. Diese Dissertation ist vollständig meine eigene Arbeit, mit der Ausnahme solcher Zitate;

5. Alle wesentlichen Quellen von Unterstützung wurden benannt;

6. Wenn immer ein Teil dieser Dissertation auf der Zusammenarbeit mit anderen basiert, wurde von mir klar gekennzeichnet, was von anderen und was von mir selbst erarbeitet wurde;

7. Ein Teil oder Teile dieser Arbeit wurden zuvor veröffentlicht (siehe Publikationsliste).

$\overline{Aachen, MONTH\ YEAR}$
Deniz Dogan

List of publications

Part of this thesis is based on the following publications:

First-author publications:

A Well-Advanced High-Throughput Test System for Electrocatalytic Screening Applications under industrial relevant conditions – A Perspective to Accelerate Electrolysis Research and Development[1]

Deniz Dogan, Burkhard Hecker, Xuehuai Hou, Inka Dessel, Andreas Müller, Guido Wasserschaff, Simone S. Köcher, Violeta Karyofylli, Hans Kungl, Hermann Tempel, and Rüdiger-A. Eichel published in *Electrochemical Science Advances* (2024), e202400015.

D. Dogan is the main contributor to this publication and was responsible for the conceptualization, methodology, investigation, validation, and formal analysis. He conducted the data visualization and authored the original draft. B. Hecker provided advice throughout the entire publication process. Chapter 4 of this publication is a guest contribution authored by S. Köcher. Review and editing of the draft was accomplished with contributions from all co-authors.

In this thesis, **Section 1.1, 1.2** and **Chapter 6** are based on this publication.

Experimental Determination of Stray Currents in Parallel Operated Cells Exemplified on Alkaline Water Electrolysis[2]

Deniz Dogan, Burkhard Hecker, Bernhard Schmid, Hans Kungl, Hermann Tempel, and Rüdiger-A. Eichel published in *Electrochimica Acta* (2024), 500, 144767.

D. Dogan is the main contributor to this publication and was responsi-

ble for the conceptualization, methodology, investigation, validation, and formal analysis. He conducted the data visualization and authored the original draft. B. Hecker provided advice throughout the entire publication process. Review and editing of the draft was accomplished with contributions from all co-authors.

In this thesis, **Section 1.3** and **4.2** are based on this publication.

Co-author publications:

High-throughput technology in electrochemistry[3],

Andreas Müller, Fabian Schneider, Florian Huber, Michael Dejmek, Guido Wasserschaff, O. Püttmann, Jago Fechtmann, Daniel Zahlmann, C. Hose, F. Eversheim, Frank Huber, Burkhard Hecker, Deniz Dogan, Hermann Tempel, Rüdiger-A. Eichel, Christoph Kröger, Sandro Haug, Sef Coenen, Patrick Löb, Christian Hofmann, Athanassios Ziogas, and Hans-J. Kost published in *Conference Proceedings - The Role of Catalysis for the Energy Transition* (2022).

High-Throughput Experimentation in Electrochemistry for Alkaline Water Electrolysis[4],

Inka Dessel, Deniz Dogan, Rüdiger-A. Eichel, Burkhard Hecker, Christian Hofmann, Florian Huber, Asha Jakob, Hans-Joachim Kost, Patrick Löb, Andreas Müller, Sarifahnurliza Sahehmahamad, Volkmar M. Schmidt, Fabian Schneider, Hermann Tempel, Guido Wasserschaff, and Athanassios Ziogas published in *Chemie Ingenieur Technik* (2024), 96, 774-780.

First-author conference contributions:

Investigations and Computer-Aided Predictions of Shunt Current Formation in Parallel Operating Electrolysis Cells (poster),

Deniz Dogan, Burkhard Hecker, Hermann Tempel, and Rüdiger-A. Eichel presented at *GDCh Electrochemistry* (2022), Berlin, Germany.

Accelerating Electrocatalytic Research for the Energy Transition by Developing a New High-Throughput Technology (poster),

Deniz Dogan, Burkhard Hecker, Hermann Tempel, and Rüdiger-A. Eichel presented at *DGMK - The Role of Catalysis for the Energy-Transition* (2022), Ludwigshafen, Germany.

Experimental and Theoretical Investigations of Stray Currents between Parallel Operated Alkaline Water Electrolyzers (presentation),

Deniz Dogan, Burkhard Hecker, Bernhard Schmid, Hermann Tempel, and Rüdiger-A. Eichel presented at *244th ECS Meeting* (2023), Gothenburg, Sweden.

Contents

Abbreviations **xv**

Abstract **xvii**

Kurzfassung **xix**

1 Introduction **1**
1.1 Electrolysis technologies 2
1.2 High-throughput experimentation 6
1.3 Ionic stray current formation 8
1.4 Objective 11

2 Materials and methods **15**
2.1 Chemicals 15
2.2 Materials 16
2.2.1 High-throughput flow cell validation materials . . 16
2.2.2 Stray current investigation materials 17
2.2.3 Stainless steel contamination investigation materials 18
2.3 Methods 19
2.3.1 High-throughput flow cell validation methods . . . 19
Electrochemical measurements 19
Cell conditioning 19
Electrochemical impedance spectroscopy 19
Polarization measurements 20
Cyclic voltammetry 20

Four-terminal sensing 21
Conductive element 22
2.3.2 Stray current investigation methods 23
Experimental measurements 23
Modelling 25
2.3.3 Stainless steel contamination investigation methods 29

3 High-throughput flow cell **33**
3.1 Cell description 34
3.2 Validation and optimization experiments 38
3.2.1 Finite-gap alkaline water electrolysis 38
3.2.2 Zero-gap anion exchange membrane water electrolysis 45
3.2.3 Zero-gap alkaline water electrolysis 55
3.3 Cell modifications 58
3.3.1 Implemented modifications 58
Inlay chamfer 58
Flow field modification 61
Current collector precious metal coatings 62
3.3.2 Further potential modifications 64
Alternative current collector materials 65
Finite-gap electrode distance 66
Four-terminal sensing 69
3.4 Summary 69

4 Stray current investigations **73**
4.1 Motivation 74
4.2 Experimental investigations of stray currents 74
4.3 Equivalent circuit stray current modeling 84
4.3.1 Model validation 84
4.3.2 Model extension 85
4.3.3 Stray current reduction in 16-cell model 89
4.4 Summary and impact on system design 91

5 Stainless steel contamination investigations 95
5.1 Motivation 95
5.2 Experimental investigations of contamination risk 96
5.3 Summary and impact on system design 100

6 High-throughput test system 103
6.1 System design approach 104
6.1.1 High-throughput test system 104
6.1.2 4-cell system prototyping and validation 108
6.2 Design of experiments 110
6.3 Research potential 112
6.3.1 Acceleration 112
6.3.2 Variability 114
Application variability 115
Process variability 116

7 Conclusion 119

A High-throughput flow cell 127

B Stray current investigations 129

C Stainless steel contamination investigations 139

Bibliography 143

Abbreviations

2TS	two-terminal sensing
4TS	four-terminal sensing
AEM	anion exchange membrane
Bal	balance
CV	cyclic voltammetry
DoE	design of experiments
EC	electrochemical
ECM	equivalent circuit model
EIS	electrochemical impedance spectroscopy
GC	gas chromatograph
HER	hydrogen evolution reaction
HT	high-throughput
KPI	key performance indicator
LLM	large language model
OER	oxygen evolution reaction
PEIS	potentiostatic electrochemical impedance spectroscopy

PEM	proton exchange membrane
PPS	peak-to-peak separation
RE	reference electrode
S	sense electrode
TRL	technology readiness level
WE	water electrolysis
WE	working electrode

Abstract

The demand for economically viable electrolysis processes has increased significantly. The application of high-throughput (HT) research represents an efficient approach to significantly reduce development times. However, existing HT platforms in electrochemistry typically support only abstract experimental conditions or are limited to specific processes, significantly restricting their technological potential for research.

This work introduces an innovative HT test system for electrolysis processes, developed in collaboration between the Institute of Energy Technologies (IET-1, Forschungszentrum Jülich GmbH) and hte GmbH. The system enables fully automated, simultaneous screening in 16 parallel-operated flow cells. The extensive system instrumentation and a specially developed cell design, aligned with commercial standards, enable operation under industrially relevant conditions. Furthermore, the system is designed for high variability, supporting all relevant low-temperature water or CO_2 electrolysis processes and standard electrochemical measurement techniques.

In this thesis, scientific work packages were conceptualized, executed, and analyzed that decisively contributed to the development of the HT system. Validation experiments are conducted on a single cell prototype to validate main cell functions and configurations and to identify optimization potentials. The implementation of a four-terminal sensing method and application of precious metal coatings to the current collectors improves measured cell performance by 12.4 % and 10.6 %, respectively. Additionally, the impact of further optimizations, such as alternative current collector materials or reduced electrode spacing, is discussed. Model-based stray current estimations for the HT system with a common electrolyte supply for all 16 cells indicate that the total stray current can be reduced from 187 to less than 2 mA under the tested conditions. How-

ever, a comprehensive analysis reveals that fully separated electrolyte circuits are preferable due to various advantages. Corrosion studies with different electrolytes on austenitic stainless steel reveal a high contamination risk. Therefore, in the HT system only inert polymers are used for electrolyte-contacting components. Finally, main system functions are validated through the operation of a 4-fold system prototype. The 4-fold study demonstrates good reproducibility, with a standard deviation of the cell voltage during alkaline water electrolysis of only 14.7 mV at 500 mA/cm^2.

Kurzfassung

Der Druck, wirtschaftlich tragfähige Elektrolyseprozesse zu entwickeln, ist stark gestiegen. Die Hochdurchsatz (HT) -forschung bietet einen effizienten Ansatz zur signifikanten Reduktion von Entwicklungszeiten. Aktuelle HT-Plattformen in der Elektrochemie unterstützen jedoch meist nur abstrakte Versuchsbedingungen oder sind auf spezifische Prozesse beschränkt, was ihr technologisches Potenzial für die Forschung erheblich einschränkt.

In dieser Arbeit wird ein innovatives HT-Testsystem für Elektrolyseprozesse vorgestellt, das in Zusammenarbeit zwischen dem Institute of Energy Technologies (IET-1, Forschungszentrum Jülich GmbH) und der hte GmbH entwickelt wurde. Es ermöglicht das vollautomatisierte, simultane Screening in 16 parallel betriebenen Flusszellen. Die umfangreiche Systemausstattung und ein speziell entwickeltes Zelldesign, das sich an kommerzielle Standards orientiert, erlauben den Betrieb unter industrierelevanten Bedingungen. Zudem ist das System auf hohe Variabilität ausgelegt und unterstützt alle relevanten Niedertemperatur-Wasser- oder CO_2-Elektrolyseprozesse sowie elektrochemische Standardmessmethoden.

In dieser Arbeit wurden wissenschaftliche Arbeitspakete konzipiert, bearbeitet und analysiert, wodurch entscheidend zur Entwicklung des HT-Systems beigetragen wurde. Durch Validierungsexperimente am Einzelzellprototypen werden wesentliche Zellfunktionen und -konfigurationen validiert sowie Optimierungspotenziale identifiziert. Die Implementierung einer Vierleitermessung und Edelmetallbeschichtungen der Stromkollektoren verbessern die gemessene Zellleistung um 12,4 % bzw. 10,6 %. Zudem wird der Einfluss weiterer Optimierungen, etwa durch alternative Stromkollektormaterialien oder reduzierte Elektrodenabstände, diskutiert. Modellgestützte Streustromschätzungen im HT-System mit gemeinsamer Elektrolytversorgung der 16

Zellen zeigen, dass der Gesamtstreustrom unter den getesteten Bedingungen von 187 auf unter 2 mA reduziert werden kann. Eine umfassende Analyse ergibt jedoch, dass vollständig getrennte Elektrolytkreisläufe aufgrund diverser Vorteile vorzuziehen sind. Korrosionsstudien mit verschiedenen Elektrolyten an austenitischem Edelstahl weisen auf ein hohes Kontaminationsrisiko hin, weshalb für elektrolytkontaktierende Komponenten im HT-System ausschließlich inerte Polymere verwendet werden. Abschließend werden wesentliche Systemfunktionen durch den Betrieb eines 4-fach Systemprototypen validiert. Die 4-fach Studie zeigt zudem eine gute Reproduzierbarkeit der Ergebnisse mit einer Standardabweichung der Zellspannung bei alkalischer Wasserelektrolyse von nur 14,7 mV bei 500 mA/cm^2.

Chapter 1

Introduction

Parts of this chapter have been published in

Dogan, Deniz, et al. "A Well-Advanced High-Throughput Test System for Electrocatalytic Screening Applications Under Industrial Relevant Conditions - A Perspective to Accelerate Electrolysis Research and Development", Electrochemical Science Advances (2024): https://doi.org/10.1002/elsa.202400015[1]

and

Dogan, Deniz, et al. "Experimental determination of stray currents in parallel operated cells exemplified on alkaline water electrolysis", Electrochimica Acta (2024): https://doi.org/10.1016/j.electacta.2024.144767[2].

The author contributions are shown in the list of publications on page vii.

Fostering a sustainable energy system to mitigate climate change is one of the greatest challenges facing humanity. The transformation of the energy system is causally linked to a reduction in dependence on fossil fuels. A key aspect of of this transformation is the direct and indirect electrification of high-emission processes through the application of energy conversion and storage technologies.[5–7]

1.1 Electrolysis technologies

Among these energy conversion and storage technologies, the implementation of electrolysis processes will play an increasingly important role. The production of green hydrogen through water electrolysis will be crucial to fully decarbonize selected sectors. According to the 1.5 °C scenario of the International Renewable Energy Agency, the annual production of green and blue hydrogen would have to be increased to 125 million tons by 2030 and to 523 million tons by 2050[8].

Water electrolysis is a well-known process in which green electricity can be used to split water into its components hydrogen and oxygen via the hydrogen evolution reaction (HER) and oxygen evolution reaction (OER), respectively. Water electrolysis processes are available for different temperature levels. The main processes in the low-temperature range are alkaline water electrolysis (AWE), proton exchange membrane (PEM) water electrolysis (WE) and anion exchange membrane (AEM) WE.[7,9]

There are major differences between those three technologies. AWE and PEM WE have a higher technology readiness level (TRL). AWE is the most mature process, requires no precious metal catalysts and offers a high system lifetime. However, compared to PEM WE, the energy efficiency is lower and the system is less suitable for dynamic operation. The use of precious metals and fluorinated membranes in the PEM WE leads to higher investment and recycling costs. On the other hand, these materials, together with a more compact system design, enable higher efficiencies and higher current densities. In addition, PEM electrolyzers

can be better scaled, operated dynamically and in a larger partial load range.[10,11] The AEM WE is an innovative electrolysis technology that promises to combine the advantages of AWE and PEM WE. AEM electrolyzers utilize non-precious catalysts and a non-fluorinated membrane assembled in a compact system design. This enables high energy efficiencies despite the use of cost-effective materials. However, this electrolysis technology still has a low TRL. One of the main challenges that needs to be solved for a broad industrial application is to achieve long-term stability at high current densities.[12,13]

Even after the transformation of the energy system, climate-damaging emissions such as CO_2 will remain. Therefore, climate-energy policies are aiming to achieve net-zero CO_2 emissions.[14] This requires efficient carbon capture and utilization technologies. In recent years, electrochemical CO_2 reduction or CO_2 electrolysis has drawn a lot of attention, as it has the potential to directly convert climate-damaging CO_2 to a variety of value-added chemicals using green electricity[15].

The first pioneering work on CO_2 electrolysis was published in the mid 1980s[16]. However, progress initially remained relatively static. Since about 2010, the field has become the focus of a broad electrochemical community and interest in commercialization has increased significantly.[17] CO_2 electrolyzers reduce CO_2 at the cathode to hydrocarbons and oxygenates, whilst H_2O is oxidized at the anode to oxygen. Both half-cells are typically separated by an ion-conducting polymer membrane. Due to the low solubility of CO_2, mass transport in purely aqueous systems is limited at high current densities. Current electrolyzer concepts are therefore commonly based on CO_2 reactions at a three-phase boundary, which is enabled by the implementation of a gas diffusion electrode (GDE) and direct CO_2 gas feed. The CO_2 reduction reaction pathways of this technology are complex and involve different multi-proton and multi-electron associated reactions. Hence, a variety of different products can be produced, including C_1 products such as carbon monoxide and formic acid, or even C_{2+} products such as ethanol, ethylene, and 1-propanol.[18–20] Due to the complexity of CO_2 electrolysis, the

process and product distribution is significantly influenced by various parameters. These include, in particular, the properties of the catalysts (element/alloy, structure, morphology, surface oxidation state and particle size), type of electrolyte, applied electrode potential, temperature, pH value, pressure, and reactor design.[21,22]

The transformation of the energy system will only succeed with the help of economically viable electrolysis technologies. Important key performance indicators (KPI) that determine the economic viability of an electrolysis technology are current density, lifetime, energy efficiency, product purity, and transient operation (Figure 1.1). Transient operation is the ability to permit quick load response times during operation and the start-stop capability of a technology. Due to the enormous quantities of green hydrogen needed, already minor KPI optimizations of water electrolysis technologies would have a major impact on the global hydrogen economy to be developed. For this reason, even efforts to optimize AWE, the most mature electrolysis technology with more than 100 years of industrial application, have increased significantly in recent years.[23] Figure 1.1a shows an estimate of the relative optimization potential of each KPI for AWE in the coming years. The greatest optimization potential lies in the current density, energy efficiency, and lifetime. According to various references, AWE operates at a maximum of 800 mA/cm^2, but in some cases below 450 mA/cm^2, which is significantly lower than that of PEM WE. However, current densities of more than 2000 mA/cm^2 are expected to be achieved in the future. The energy efficiency of current AWE systems is between 60 - 70 %, but could be improved to over 70 %. Although AWE systems have a relatively long lifetime (up to 60,000 h), it has the potential to be further increased to up to 100,000 h by electrode developments.[24,25]

Among all CO_2 electrolysis technologies, the conversion of CO_2 to CO is the most developed process. However, there are still many challenges to be overcome before the technology is ready for commercial use. Figure 1.1b shows the relative optimization potential of CO_2-to-CO electrolysis for each KPI. Current densities of 200 to 500 mA/cm^2 have frequently

been demonstrated and thus reached a technically relevant level. However, the potential of this technology is even expected to be in the range of up to 1000 mA/cm^2. Although technically relevant current densities can be achieved, there are hardly any references demonstrating these conditions over longer operating times.[18,26] For commercial viability, however, lifetimes of up to 50,000 hours must be achieved. In terms of energy efficiency, the technology already shows good performance at over 50 % and is expected to improve to over 75 %.[17,27] CO_2-to-CO electrolysis currently already achieves very good Faradaic efficiencies of over 90 %. The competing HER can therefore be largely suppressed during operation. However, the product purity of the process suffers severely from low single-pass CO_2 conversion rates. By improving the CO_2 conversion rate, the product purity can be increased and thereby downstream costs reduced.[28] For economically viable application, electrolysis technologies must ideally enable good transient operation. Due to the low TRL of CO_2-to-CO electrolysis, there is unfortunately still hardly any data on this.

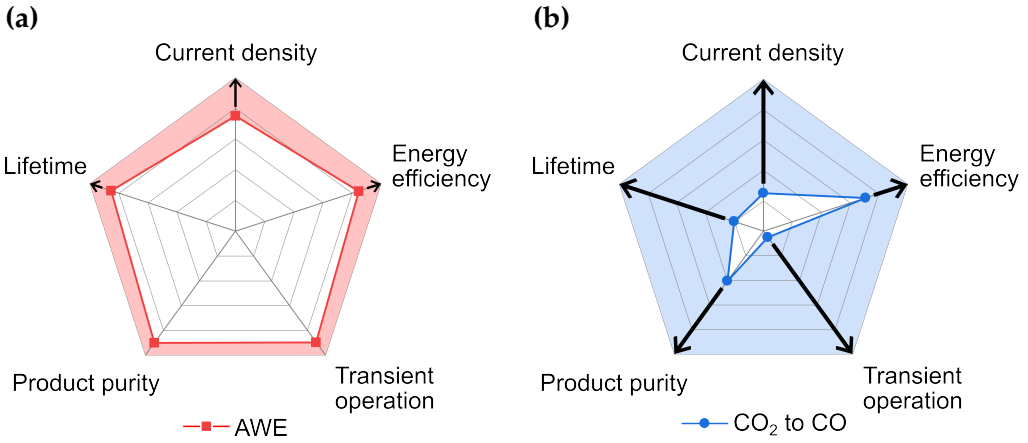

Figure 1.1: Optimization potentials (colored areas) of key performance indicators (KPI) for next generation alkaline water (AWE, red squares) and CO_2 to CO (blue circles) electrolyzers. Net charts indicate the technology-specific current status of the individual KPIs on the scale of the targeted optimization goals for: current density, lifetime, energy efficiency, product purity, and transient operation. State-of-the-art values are dimensionless plotted against KPI values expected in the future.[24,27]

Compared to traditional chemical processes, the development of electrolysis technologies is typically more complex due to the large number of different KPIs (Figure 1.1) and additional electrochemistry-specific process parameters. This increased complexity impedes rapid advancements in the development and optimization of these technologies. At the same time, the pressure to develop economically viable electrolysis technologies has increased considerably in recent years due to the verifiable reliance on these processes in the future. High-throughput (HT) experimentation that enables time-efficient research in such a complex and multidimensional field could make a decisive contribution to resolving this conflict.

1.2 High-throughput experimentation

HT experimentation refers to methods and systems designed to perform automated, accelerated testing and analyses of an increased number of samples or process conditions. It involves either rapid serial or parallel workflow processing, thereby significantly accelerating research efforts and, hence, minimizing the time-to-market for, e.g., novel catalysts, materials, compounds, or processes.[29,30] HT technology has its roots in pharmaceutical research[31] and was soon adopted in research and development in areas such as materials science[32] or heterogeneous catalysis[33]. For electrochemical processes, additional electrochemistry-related parameters substantially increase the complexity of the parameter space compared to conventional catalysis. To address this complexity, HT technologies are a promising experimental approach for research and development in electrochemical research.[34] However, the extended parameter space and complexity of electrochemical systems hampered the emergence of such technologies in this field[35,36]. The first electrochemical HT developments were batch systems with an array structure approach, for example, based on microtiter plates or wafers, with which the individual samples are automatically and serially scanned in X-Y direction[37–39].

They enable the testing of either one electrolyte vs. many electrodes[40–44] or one electrode vs. many electrolytes[45,46]. Other systems perform HT batch screening by running experiments in parallel[47–51]. HT batch systems are also commercially available[52–55]. The references listed report on static systems without convective electrolyte flow[40–55]. Later, HT systems with electrochemical flow cells were developed[56–60].

The electrocatalytic HT systems developed up until now have some major disadvantages. The batch cell systems described in the literature are strongly diffusion-controlled and typically provide only the testing of undivided cells. The maximum current densities are far below the range of interest for industrial applications. Flow cell systems, on the other hand, achieve higher current densities and have improved concentration gradients due to the electrolyte flow through the cell. However, due to miniaturization, they are characterized by laminar flow and, in some cases, also only provide undivided cells. Electrocatalysis on a production scale is generally practiced in divided flow cells at high current densities, in which turbulent mixing is common[34]. Compared to those industrial standards, previously developed HT systems in electrochemical research provide abstract experimental conditions. However, testing under industry-relevant conditions is crucial to evaluate the operational capability of processes or materials for industrial applications.

Another disadvantage is that previous electrocatalytic HT systems were developed specifically for certain applications or processes. This specific design typically impedes or even prevents the investigation of other applications or processes with these systems. This severely limits the variability of previous systems. Due to its high relevance, electrocatalysis is a highly dynamic research field. The focus of research is in constant discourse in science and politics and can therefore readily change. High system variability is essential to fully exploit the potential of a HT system in the diverse and dynamic field of electrochemical research.

Insufficient comparability of experimental results with literature data is a well-known issue in electrochemistry and hinders progress in elec-

trochemical process development[61–63]. An additional disadvantage of previous HT systems is that both abstract experimental conditions and application- or process- specific system designs impair the comparability of the data generated.

Abstract experimental conditions, limited system variability and impaired data comparability are major disadvantages of the previously developed HT systems in electrochemical research. These disadvantages arise primarily from their simplified design, which is typically intended to reduce development time and investment costs. Such systems have proven to be an effective solution for early-stage screening in particular pre-defined applications and processes. However, the disadvantages discussed hinder a HT platform from unleashing its full potential under the current requirements of electrochemical research.

1.3 Ionic stray current formation

Ionic stray current formation is a well-studied phenomenon in electrochemical bipolar cell stacks. Such cell stacks consist of multiple electrochemical cells that are galvanically connected in series with bipolar plates and commonly designed with a shared electrolyte feed.[64] Due to the bipolar structure and electrolyte conductivity, an electrochemical potential gradient is formed across the shared electrolyte feed. Under these conditions, ionic stray currents flow from one cell to the adjacent cell bypassing the bipolar plates (Figure 1.2a).[65–67]

As in bipolar stacks, similar conditions can theoretically also prevail in a system comprising individual cells operated in parallel with a common electrolyte feed. Although the cells in such a system are galvanically isolated, the individual cells would be ionically connected to each other through the electrolyte of the common feed. This ionically conductive cell-to-cell connection could again serve as a pathway for undesired stray current formation (Figure 1.2b). Simultaneous testing of parallel experiments is a common approach in HT research (cf. Section 1.2). A common

electrolyte supply can be advantageous in such systems as it could increase comparability between experiments and save costs[68].

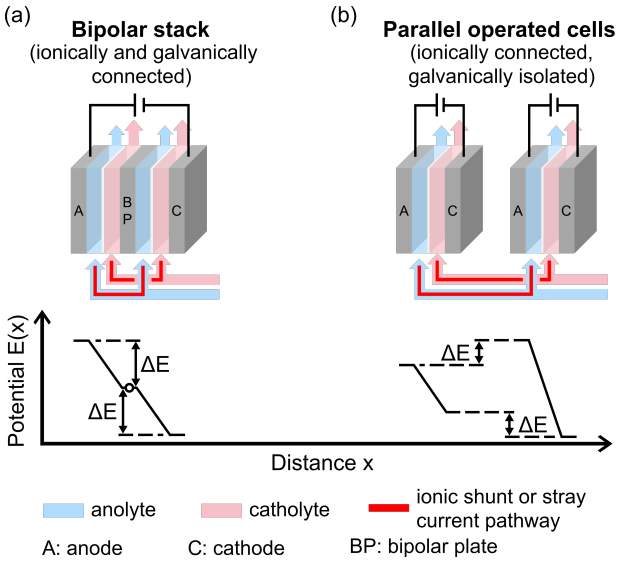

Figure 1.2: Stray current formation through parallel tubing for common electrolyte feed in two different electrochemical systems: (a) electrochemical stack with bipolar plate that galvanically connects two cells, thereby serially building up the total electrochemical stack potential and (b) parallel operating cells that are galvanically isolated with electric fields freely aligned with each other.

The magnitude of stray currents in an electrochemical system with common electrolyte supply depends on the total number of cells in the system, magnitude of cell voltages, electrolyte conductivity and geometry of the tube manifold.[69] Depending on the type of electrochemical system, stray currents can cause

- decrease in Faraday efficiency and overall energy efficiency[70],
- accelerated aging at electrode regions near to the electrolyte inlets and outlets particularly of the terminal electrodes induced by locally above-average current densities[71,72],
- non-uniform voltage and current distribution in stacks, leading to different cell performances depending on the cell position within

the stack[73],

- interference with instrumentation, undesirable gas formation or corrosion of metallic components[67,74,75], and

- explosive or flashover voltage hazard[76,77].

In the literature, two approaches can be found to quantify stray currents, i.e. a theoretical, model-based method and experimental approaches. The former was first pursued in the 1940s, where an equivalent circuit model (ECM) was proposed to describe an electrochemical system[78]. Using ECMs, stray currents can be determined based on Kirchoff's laws. In 1976, an ECM was developed for NASA to estimate stray currents in redox flow battery systems[79]. In the following decades, this approach was adapted and published for Fe/Cr redox flow battery[80–82] and fuel cell systems[83–86]. Further studies show ECM based stray current determination in Vanadium redox flow batteries[67,87,88]. For the quantification of stray currents, most studies are based on the theoretical approach. Few publications demonstrate the experimental determination of stray currents. For experimental quantification, for instance magnetic field detectors were used to measure the magnetic field generated by stray currents[89]. Only a few research groups determined the potential difference or directly stray currents through the electrolyte in the tube manifold[90,91]. One research group investigated experimentally and computationally the effect of stray currents on the primary and secondary current distribution at the electrodes in an undivided bipolar stack[92,93].

The cited literature on the theoretical or experimental determination of stray currents focuses almost exclusively on bipolar stack systems. Due to the serious effects of stray currents, it is important to similarly estimate and control their magnitude in other system configurations where stray currents may occur. The operation of individual electrochemical flow cells in parallel with a common electrolyte feed may be a well-suited configuration for the development of an electrocatalytic HT test system. However, ionic stray current formation between parallel operated cells

has hardly been studied.

1.4 Objective

The objective of this project is the development of an HT test system for electrochemical bench-scale flow cells. The project is a collaboration between the Institute of Energy Technologies – Fundamental Electrochemistry (IET-1, Jülich, Germany) and the industry partner hte GmbH (Heidelberg, Germany). This HT system is developed to offer a fully automated, advanced research platform that enables the parallel operation of 16 flow cells under industrially relevant conditions, thereby accelerating research activities on advanced electrolysis processes toward a higher TRL. Rather than focusing on one process or application, the system will be designed to operate with the most common applications and various processes in electrochemistry, offering a high degree of process and application variability. The system should generate reliable, reproducible, high-quality data in order to improve comparability between the flow cells operated in parallel.

In the course of this project, various scientific tasks or questions emerged during the engineering of the system. These tasks were structured into specific work packages. This thesis focuses on the detailed investigation, analysis, and discussion of these work packages, which played a pivotal role in driving the development of the HT system.

- The functionality of the HT system is critically dependent on the type and characteristics of the electrochemical flow cell operated. To meet all scientific and operational requirements, a new flow cell was specifically engineered and manufactured for the system. The flow cell was developed in collaboration between hte GmbH (Heidelberg, Germany), Fraunhofer Institute for Microengineering and Microsystems (IMM, Mainz, Germany), and Institute of Energy Technologies – Fundamental Electrochemistry (IET-1, Jülich, Germany). The objective of this work package is the experimental char-

acterization, validation, and optimization of the developed electrochemical HT flow cell. This work package is presented in Chapter 3.

- For the design of the electrolyte supply system of the HT system, a common feed was considered for the 16 flow cells via a tube manifold. In this supply system design, ionic stray currents can flow from one cell to the neighboring cell due to the electrolyte conductivity. The objective of this work package is the experimental and theoretical investigation of stray currents in systems with parallel flow cells and a common electrolyte supply. On the basis of the data obtained, a decision will be made for or against the implementation of a common electrolyte supply system in the HT system. This work package is presented in Chapter 4.

- The use of corrosion-resistant stainless steel system components offers economic advantages and can generally be implemented without concern in some parts of the HT system. However, due to the planned use of corrosive electrolyte solutions, the suitability of stainless steel for components in contact with the electrolyte remains uncertain. Chemical corrosion may lead to the release of metal ions into the electrolyte, resulting in contamination and potentially negatively impacting the process. The objective of this work package is to experimentally investigate the contamination risk caused by corrosion-resistant stainless steel in contact with various electrolyte solutions planned for the system. Based on the generated data, a decision will be made regarding the suitability of stainless steel components for the implementation in the electrolyte circuit. This work package is presented in Chapter 5.

- In Chapter 6, the finalized HT system is introduced. In addition to presenting the system design, first experimental data of a 4-fold prototype were recorded and are shown for system validation. Furthermore, the research potential of the developed HT system is discussed with respect to acceleration, process and application vari-

ability, as well as the application of Design of Experiment (DoE) methods.

Chapter 2

Materials and methods

The following chapter presents all chemicals, materials and methods used in the course of this work.

2.1 Chemicals

Table 2.1 lists all chemicals used for the electrolyte solutions tested in this work. The electrolyte solutions were prepared with deionized water ($\geq$18.2 MΩ cm) from a PURELAB®flex water purification system (Veolia Environnement S.A., Aubervilliers, France).

Table 2.1: Chemicals for electrolyte preparation.

Chemical	Purity	Supplier
Hydrogen chloride 37% (HCl)	p.a.	Carl Roth GmbH
Potassium bicarbonate ($KHCO_3$)	$\geq$99.5 %	Merck KGaA
Potassium hydroxide (KOH)	p.a.	Merck KGaA
Sodium chloride (NaCl)	Reag. Ph. Eur.	Merck KGaA
Sulfuric acid 96% (H_2SO_4)	Reag. Ph. Eur.	VWR Internat. Ltd.

2.2 Materials

2.2.1 High-throughput flow cell validation materials

The flow cell is an in-house development for the HT system in collaboration between hte GmbH (Heidelberg, Germany), Fraunhofer Institute for Microengineering and Microsystems (IMM, Mainz, Germany) and Institute of Energy Technologies – Fundamental Electrochemistry (IET-1, Jülich, Germany). The following material information refers to the single-cell experiments conducted at the IET-1. The reproducibility study with parallel-operated HT cells in the 4-fold prototype system was carried out on site at the project partner hte GmbH. All materials used for the validation of the HT flow cell in finite-gap AWE and zero-gap AWE configuration are listed in Table 2.2. The reference electrode was connected in finite-gap configuration using a Haber-Luggin capillary made of PEEK ($d_i = 0.5\,mm$).

Table 2.2: Materials for finite-gap and zero-gap AWE experiments.

Type	Specification	Supplier
Electrodes (finite-gap)	Ni foil (125 µm)	Thermo Fisher Scientific Inc.
Electrodes (zero-gap)	Ni mesh (300 µm)	Haver Boecker
Separator	Zirfon PERL UTP 220	Agfa-Gevaert N.V.
	ZrO_2	
	PPS fiber	
Reference electrode	RE-61AP	ALS Japan Co., Ltd.
	Hg/HgO (6 M KOH)	
Conductive elements	Ni, Pt, and Au wires	
	125 µm Ni foil	Thermo Fisher Scientific Inc.
	50 µm Ni mesh	Thermo Fisher Scientific Inc.

All materials used for the validation of the HT flow cell in zero-gap AEM WE configuration are listed in Table 2.3.

Due to the design of the HT flow cell, flat gaskets in various dimensions are required for assembly. The gaskets are used in different thicknesses of 120 and 250 µm (PTFE) or 300 and 500 µm (silicone). Variations in the thickness of the installed materials can therefore be compensated,

Table 2.3: Materials for zero-gap AEM WE experiments.

Type	Specification	Supplier
Anode	$NiFe_2O_4$	Dioxide Materials
	316L sintered stainless steel GDL	
Cathode	Ni	Dioxide Materials
	Ni fiber paper	
Membrane	PiperION® 20, 40, and 60 µm	Versogen
	Functionalized PAP	

ensuring optimal surface pressure necessary for effective electrode contact. All gasket types with specifications are listed in Table 2.4.

Table 2.4: Gaskets for HT flow cell assembly.

Material	Outer contour [mm]	Inner contour [mm]	Thickness [µm]	Supplier
Silicone	61 × 61	22.4 × 22.4	300, 500	Reichelt Chemietechnik GmbH
Silicone	61 × 61	44 × 44	300, 500	
Silicone	57 × 57	44 × 44	300, 500	
Silicone	44 × 44	–	500	
PTFE	61 × 61	44 × 44	120, 250	Bohlender GmbH

The HT flow cell is made almost entirely of PEEK. An EPDM flat gasket is placed between the two half-cell housings to ensure sealing. The current collectors and the metal contact frame on the inside of the half-cell housings are made of Ti grade 5. The composition of Ti grade 5 is shown in Table 2.5.

Table 2.5: Nominal composition of Ti grade 5 (Ti-6Al–4V) in wt. %.[94]

Element	Ti	Al	V	Fe	O	C	N	H
Composition	Bal.	6	3.5-4.5	0.4	0.2	0.1	0.05	0.015

2.2.2 Stray current investigation materials

Stray current experiments were conducted with commercially available Micro Flow Cells® from ElectroCell A/S (Tarm, Denmark). All installed materials used for experimental measurements are listed in Table 2.6.

Table 2.6: Materials for stray current experiments.

Type	Specification	Supplier
Electrodes	Ni foil (2 mm)	ElectroCell A/S
Reference electrodes	RE-61AP	ALS Japan Co., Ltd.
	Hg/HgO (6 M KOH)	
Separator	Zirfon PERL UTP 500	Agfa-Gevaert N.V.
	ZrO_2	
	PPS fiber	
Gasket	EPDM (0.5 mm)	ElectroCell A/S
Flow field frame	PTFE (1.5 mm)	ElectroCell A/S

2.2.3 Stainless steel contamination investigation materials

AISI 316Ti (EN 1.4571) was selected to investigate the risk of metal ion contamination of various electrolyte solutions in contact with stainless steel. This austenitic stainless steel is characterized by high corrosion resistance[95]. For the experiment a pipe with an inner and outer diameter of 4 and 6 mm was used. The material composition is shown in Table 2.7.

Table 2.7: Composition of AISI 316Ti austenitic steel (EN 1.4571, X6CrNiMo17-12-2) in wt. %.[96]

Element	Fe	Cr	Ni	Mo	Mn	Si	Ti	C	P	S
Min.	Bal.	16.5	10.5	2	2	-	5xC	-	-	-
Max.	Bal.	18.5	13.5	2.5	2	1	0.70	0.08	0.045	0.015

2.3 Methods

2.3.1 High-throughput flow cell validation methods

Electrochemical measurements

All validation experiments were measured with a multi-channel potentiostat type AUTM204.S combined with a 10 A Booster from Metrohm AG (Herisau, Siwtzerland). The experiments were conducted with either 6 M KOH (finite-gape AWE and zero-gap AWE) or 1 M KOH (zero-gap AEM WE) as anolyte and catholyte. In both electrolyte cycles, 150 mL of the solution was circulated separately using peristaltic pumps at a flow rate of 40 or 50 mL/min. For measurements at elevated temperatures, the electrolyte reservoirs were heated in a water bath. The electrolyte temperature was measured with temperature sensors directly in the reservoir using an ALMEMO® 710 data logger from Ahlborn Mess- und Regelungstechnik GmbH (Holzkirchen, Germany). A sequence of different electrochemical methods was applied to validate the performance of the HT flow cell, including preconditioning, electrochemical impedance spectroscopy, and polarization measurements.

Cell conditioning

The system was conditioned prior to each experiment to activate the electrocatalysts and achieve a steady state of the membrane[97,98]. For this purpose, chronopotentiometry was applied to the system for 1 h. A current density of 500 and 1000 to 2000 mA/cm^2 was applied for the AWE and AEM WE processes, respectively.

Electrochemical impedance spectroscopy

Electrochemical impedance spectroscopy (EIS) measurements were used to determine the ohmic cell resistance. The cell resistance was derived from the x-intercept of the Nyquist plot at high frequencies. Measurements were conducted in a wide frequency range from 0.1 to 100000 Hz

with an amplitude of 10 µA and a frequency step size of 10 points per decade. The EIS data were recorded prior to and after cell conditioning.

Polarization measurements

The recorded polarization curves provided important information about the cell performance of the AWE and AEM WE processes and formed an important basis for determining the optimization potential of the HT flow cell. The galvanostatic polarization measurements were carried out in the range from 0 to 500 mA/cm^2 (finite-gap/zero-gap AWE) and 0 to 2000 mA/cm^2 (zero-gap AEM-WE) with 50 mA/s scan rate and 20 mA step size.

Cyclic voltammetry

Cyclic voltammetry (CV) was used to validate the operation of the HT flow cell in 3 electrode setup with reference electrode. The CVs were recorded at different scan rates from 5 to 20 mV/s and a step size of 0.2 mV. Five CV cycles were measured per scan rate. The data from the third scan was used for analysis, while the initial scans served to stabilize the electrochemical system for reproducibility. The following scans were recorded to verify the continued stability of the measurement.

The peak-to-peak separation (PPS) was used as a characteristic quantity to analyze the CV diagrams. It can be used to evaluate the reversibility of an electrochemical system. The PPS determines the difference between oxidative and reductive peak potentials, which are influenced by external factors such as the CV scan rate[99].

For further analysis of the measured CV diagrams, the roughness factor f_R of the electrode surface can be estimated. It is defined as the ratio of the electrochemically active surface area A_{ECSA} to the geometric surface area A_{geo} (Equation 2.1). For that purpose, the cathodic charge Q_{cat} is divided by the charge required for one monolayer coverage of the electrode surface for a two-electron desorption Q_{des}. According to the literature, Q_{des} of 1 cm^2 geometric surface area is estimated to 420 $\mu C/cm^2$.[100,101]

$$f_R = \frac{A_{ECSA}}{A_{geo}} = \frac{Q_{cat}}{Q_{des}} = \frac{Q_{cat}}{420\,\mu C/cm^2 \cdot A_{geo}} \tag{2.1}$$

The cathodic charge Q_{cat} can be determined based on the reduction peak, which corresponds the integrated peak area divided by the CV scan rate v.

$$Q_{cat} = \frac{1}{v}\int_{\varphi_0}^{\varphi_1} I\, d\varphi \tag{2.2}$$

Four-terminal sensing

Figure 2.1 shows the different sensing methods applied during the validation of the HT flow cell in the course of this work.

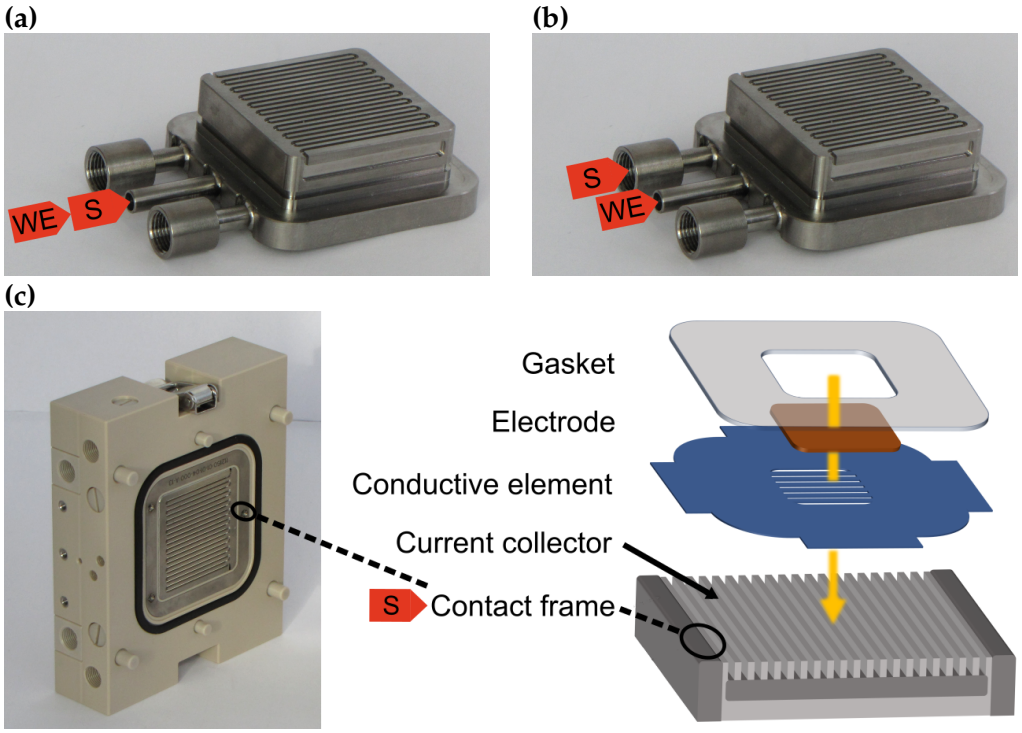

Figure 2.1: Sensing methods applied: (a) two-terminal sensing (2TS), (b) four-terminal sensing via heat exchanger inlet of the current collector ($4TS_{cc}$), and (c) four-terminal sensing via contact frame ($4TS_{frame}$). For clarity, only the working electrode (WE) and sense electrode (S) connections are depicted.

In a two-terminal sensing (2TS), the working electrode (WE) and the sense electrode (S), as well as the counter electrode (CE) and the reference electrode (RE), are not separated (Figure 2.1a). By separating the WE and S as well as the CE and RE connections of the potentiostat at the cell, the influence of specific components can be included or excluded from the measurement. This configuration is known as four-terminal sensing (4TS). In this work, two methods of 4TS have been developed for the HT cell. Figure 2.1b shows the first method, where S and RE are connected to the heat exchanger inlet of the current collector ($4TS_{cc}$) and thus are separated from the current-carrying wires. In the second method, S and RE are connected to a separate electrical connection, which directly connects S and RE to a metal contact frame ($4TS_{frame}$) on the inside of the cell housing (Figure 2.1c). With this method, a conductive element must be installed in the cell to contact the electrode with the contact frame.

Conductive element

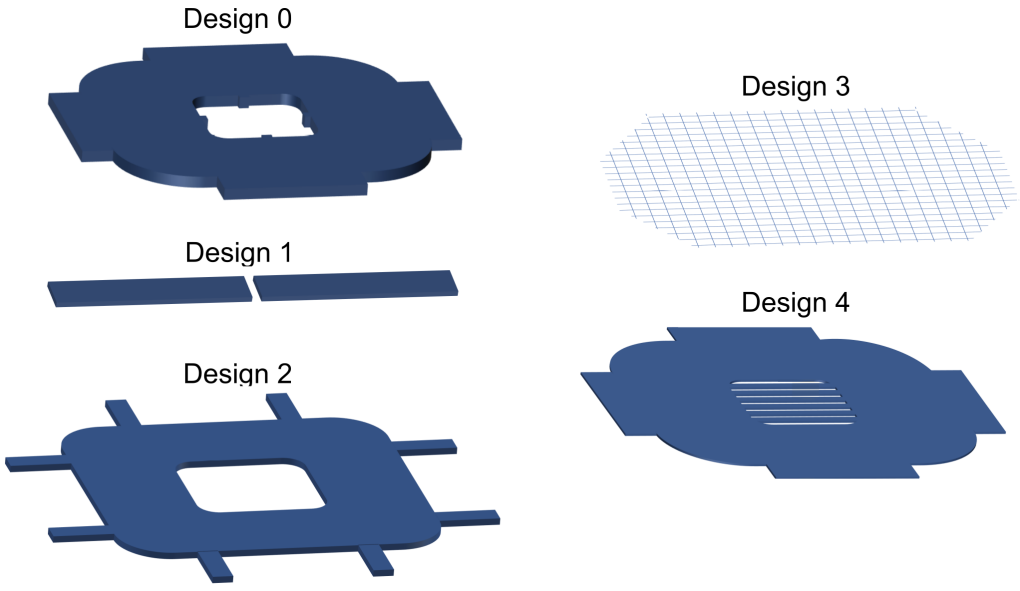

Figure 2.2: Schematic illustration of different designs of the conductive element. The conductive element is required for four-terminal sensing via the contact frame.

The conductive element is of key importance for the $4TS_{frame}$ method. The primary function of the conductive element is to provide electrical contact between electrode and contact frame. Various designs have been developed for this purpose, which differ in terms of geometry and material. All designs tested in this work are depicted in Figure 2.2. For Design 1, thin wires of Ni, Pt and Au were rolled into strips with a thickness of 160 - 200 µm. For Design 0, Design 2, and Design 4, a 125 µm Ni foil was used. Design 3 is based on a Ni mesh with a thickness of 50 µm (cf. Table 2.2).

2.3.2 Stray current investigation methods

Experimental measurements

An experimental setup has been developed for the measurement of ionic stray currents between parallel flow cells (Figure 2.3). Two flow cells were operated independently using individual channels of a VSP-300 potentiostat from Bio-Logic SAS (Seyssinet-Pariset, France). Both cells were galvanically isolated, and the anolyte and catholyte circuits were separated. The anolyte and catholyte for both cells are supplied from common reservoirs. Each of the electrolyte streams is split before entering the two flow cells and recombined downstream using tee connectors. An ionic 4-point measurement was implemented to determine the stray currents. For this purpose, modified flow fields with a 1 mm groove were installed in the cells (cf. Figure B.1). Haber-Luggin capillaries were inserted through the groove directly into the cell to the electrode. The reference electrodes were placed in external vessels filled with electrolyte. A total of 4 reference electrodes were used for the ionic 4-point measurement.

Two commercial Micro Flow Cells® from ElectroCell A/S (Tarm, Denmark) were used in the setup shown in Figure 2.3. Both cells were operated with AWE and built identically. The materials used are listed in Table 2.6. The geometric active electrode surface area was 10 cm^2 with an electrode-separator distance of 2 mm. A 6 M KOH solution was used

as anolyte and catholyte (cf. Table 2.1). 250 mL of the solution was filled into each of the separate reservoirs and circulated at 100 mL/min using a peristaltic pump. The hydrogen and oxygen produced were diluted and expelled with a 50 mL/min argon stream in the headspace of the reservoirs. FEP tubing with an inner diameter of 4 mm was used for the electrolyte supply system. The tubing adapters were made of PP.

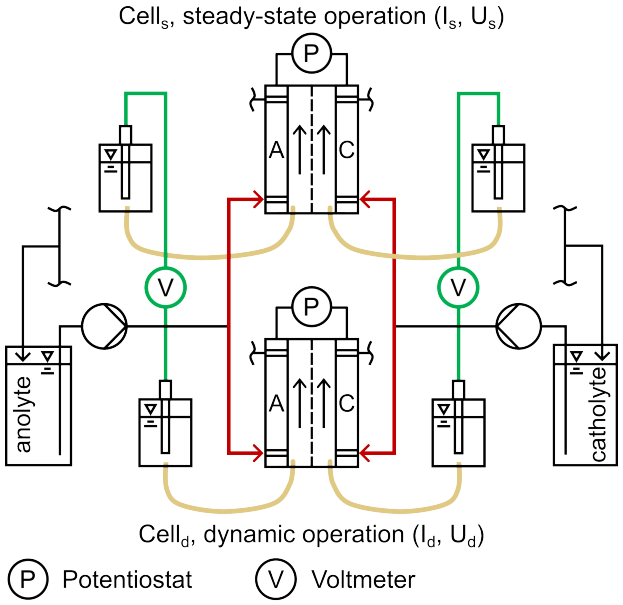

Figure 2.3: Schematic illustration of experimental setup for potential difference measurements between two electrochemical flow cells. An ionic 4-point measurement was developed by implementing four reference electrodes. Potential differences were measured between neighboring electrodes (green line) to determine stray currents (red line) between parallel operated cells.

For each experiment, one channel of the potentiostat was set to grounded mode and the second channel was set to floating mode. Operating the second cell in floating mode prevents the electrical circuits of both cells from being short-circuited via grounding.[2] One cell was operated constantly under steady-state conditions (cell$_s$) at 100 mA/cm^2, while the operating parameters of the second cell were dynamically varied (cell$_d$) between 1 and 500 mA/cm^2. Both cells were preconditioned for 1 h at 100 mA/cm^2 prior to each experiment.

Stray currents between both flow cells are determined by measuring the potential differences. The setup described above for ionic 4-point measurement using reference electrodes enables measurement of the potential difference between neighboring anodes and between neighboring cathodes. The measurements were carried out with a 175 True RMS multimeter from Fluke Corporation (Everett, USA) on the reference electrodes as shown in Figure 2.3. For each data point plotted, the average of three measurements was taken. All potential and potential difference measurements were IR drop corrected. In addition to the potential differences, the ohmic resistance of the tube manifolds between both cells is required to determine the stray currents. The manifold resistance was determined in situ and additionally validated ex situ by potentiostatic electrochemical impedance spectroscopy (PEIS). The resistance of the entire manifold supply system, including all four tube connections, was recorded in situ applying PEIS between cathode and cathode, as well as between anode and anode of both cells. For validation, the resistance of a single manifold tube connection between the cells was determined ex situ in a separate setup. The setup is shown in Figure B.5 in the appendix. All PEIS measurements were carried out in the frequency range from 0.1 Hz to 10^5 Hz at 0 V with an amplitude of 10 mV and 6 points per decade. The electrolyte flow rate during the measurements was set to 10 ml/min.

Modelling

Equivalent circuit model

An ECM was developed to estimate the stray currents in the 16-cell HT system in the case of a common electrolyte supply. First, such an ECM was built for two parallel cells, which corresponds to the setup of the experimental stray current determination (cf. Figure 2.3). Figure 2.4a shows a schematic representation of the setup used with all components relevant for stray current formation. The corresponding ECM consists mainly of ohmic resistors and is shown in Figure 2.4b. Both cells con-

sist of a cell resistance R_c and a DC voltage source. For estimations in extended models with additional cells, each of the four tube connections is divided into one tube channel per cell and a tube manifold connecting both channels. Tube channels and manifold are represented by the channel resistors R_{ch} and the manifold resistor R_m respectively.

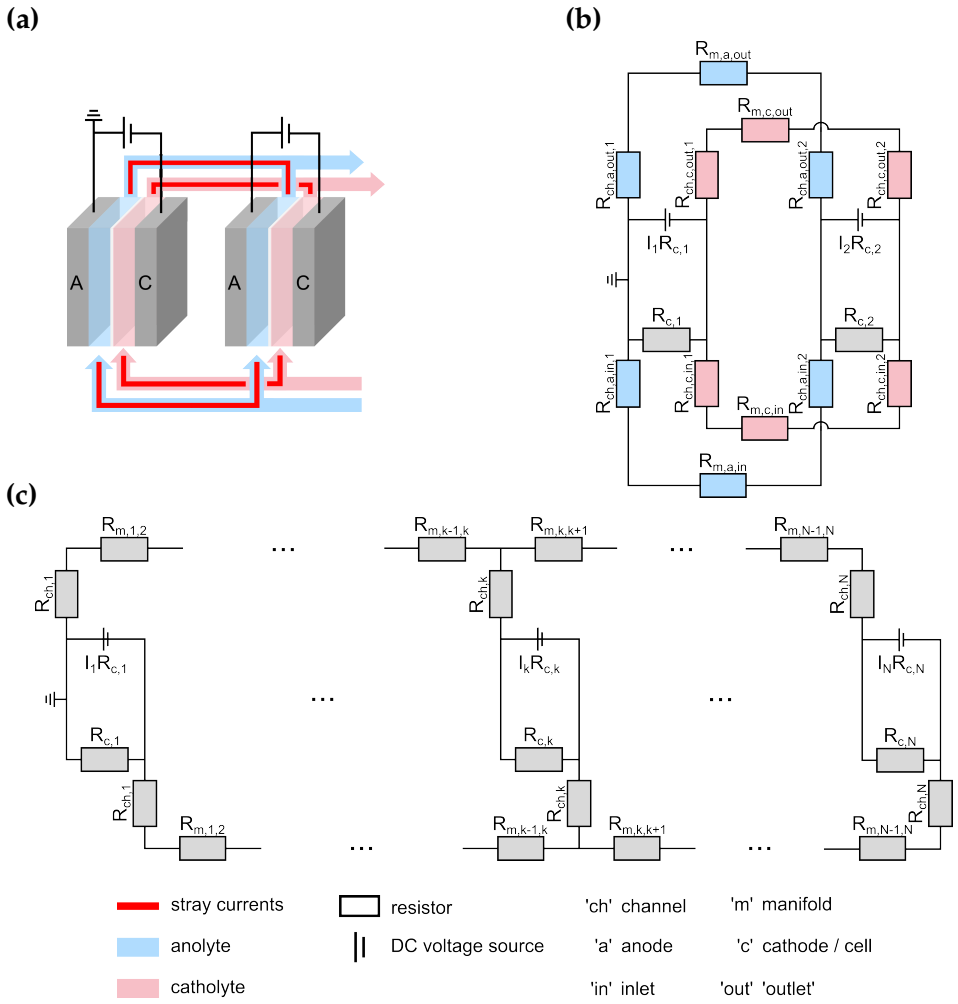

Figure 2.4: Schematic illustration of (a) two parallel, galvanically isolated flow cells with common electrolyte supply and (b) corresponding 2-cell equivalent circuit model. (c) Simplified equivalent circuit model for N parallel cells.

The 2-cell ECM can be extended by any number of cells to estimate stray currents in larger systems. Figure 2.4c shows a generalized,

extended ECM for N parallel cells. Due to the given symmetry of the setup, the inlet and outlet connections of both half-cells can be combined if the resistance values are adjusted accordingly.

Model equations

The magnitude of stray currents flowing in a parallelized system depends on the potential difference between the flow cells ΔE. The ECM developed in this work (Figure 2.4c) is based on the assumption that ΔE is primarily determined by the overvoltages generated by the ohmic cell resistances. Based on this simplification, the potential difference is obtained for two cells as

$$\Delta E = I_2 R_{\mathrm{c},2} - I_1 R_{\mathrm{c},1} \tag{2.3}$$

The ohmic overpotential of a cell is equal to the product of the cell current I and the cell resistance R_c. IR_c can be determined as

$$I R_{\mathrm{c}} = U(I) - E_{\mathrm{a}}(I) + E_{\mathrm{c}}(I) \tag{2.4}$$

E_a and E_c are the current-dependent potentials of the anode and cathode, and U is the cell voltage. Based on Ohm's law and Equation 2.3, the stray current between two cells can be calculated as

$$I_{\mathrm{sc}} = 4\frac{\Delta E}{R_{\mathrm{t}}} \tag{2.5}$$

R_t is the total tube resistance of one of the four identical connections between two cells. The tube resistance is divided into one channel resistance R_{ch} per cell and the manifold resistance R_m.

$$R_{\mathrm{t}} = 2R_{\mathrm{ch}} + R_{\mathrm{m}} \tag{2.6}$$

To determine the resistance between non-neighboring cells, further manifold resistances must be added accordingly.

$$R_{\mathrm{t,n}} = 2R_{\mathrm{ch}} + (n-1)R_{\mathrm{m}} \tag{2.7}$$

For the design of the tube connection various approaches can be utilized. To quantify the tube configuration, a design factor f_d is defined, representing the ratio of R_m to R_t.

$$f_{\mathrm{d}} = \frac{R_{\mathrm{m}}}{R_{\mathrm{t}}} \tag{2.8}$$

Model assumptions

The model validity for stray current estimations relies on the following assumptions

1. kinetic and mass transport overpotentials are negligible,
2. no gas crossover through the membrane,
3. system operates under isothermal conditions,
4. current distribution across the electrode surface is uniform, and
5. impact of generated gas bubbles is neglible.

The first assumption allows the simplification in Equation 2.3 to calculate the potential difference. However, this assumption cannot be made for the entire load range of a flow cell. In the range of very low or very high loads, kinetic and mass transport effects can play a dominant role. For this reason, the current density range of the ECM developed here must be constrained.

Based on the experimental studies (cf. Section 2.3.2), all stray current estimates are carried out for AWE. Taking into account the given process and system characteristics, the model validity was constrained to a current density range of 50 to 2000 $\mathrm{mA/cm^2}$. Implementation and modeling

of the developed ECM was done in the open source software Quite Universal Circuit Simulator© (QUCS, version 0.0.19).

2.3.3 Stainless steel contamination investigation methods

The setup shown in Figure 2.5 was developed to investigate the risk of metal ion contamination from stainless steel in contact with electrolyte solutions. The reservoir was filled with 100 mL of electrolyte. The solution was pumped through a stainless steel tube using a peristaltic pump. Austenitic steel type AISI 316Ti (EN 1.4571) was selected, which is known for its good corrosion resistance[95]. The composition of AISI 316Ti can be found in Table 2.7. The contact area of the stainless steel pipe with the electrolyte $A_{contact}$ was 20 cm^2. Hence, a pipe with inner diameter d_i of 4 mm was used and cut to a length l of 15.9 cm. After the steel pipe the electrolyte was returned to the reservoir. The peristaltic pump circulated the electrolyte solution continuously at 20 ml/min for 7 d. A reference sample of the electrolyte was taken before the start of the experiment.

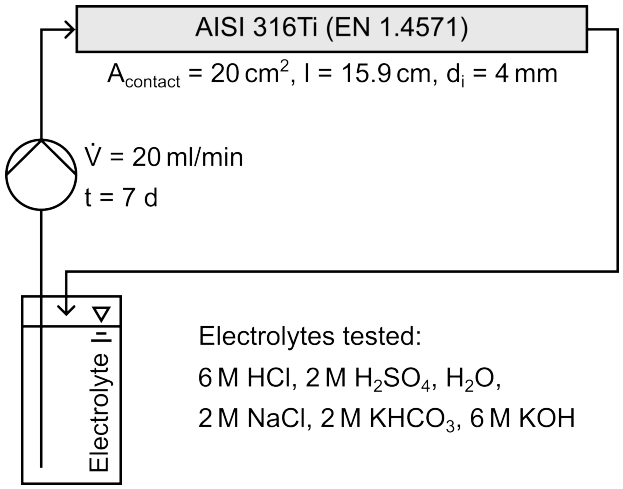

Figure 2.5: Schematic illustration of experimental setup for investigation of metal ion contamination risk of different electrolyte solutions in contact with stainless steel. The electrolytes were continuously circulated through a AISI 316Ti (EN 1.4571) stainless steel pipe with a contact area $A_{contact}$ of 20 cm^2 at 20 ml/min over 7 d.

Further 1 mL liquid samples were taken after 5 min, 1 h, 1 d, 2 d, 3 d, 5 d and 7 d. All samples were analyzed by ICP-OES for the concentration of Fe, Ni, Cr, Mo and Ti ions. The experiment was carried out with 6 M HCl, 2 M H_2SO_4, deionized H_2O, 2 M NaCl, 2 M $KHCO_3$, and 6 M KOH (cf. Table 2.1). All tubes and tube adapters used were made of FEP and PP.

Chapter 3

High-throughput flow cell

Parts of this chapter have been published in

Dogan, Deniz, et al. "A Well-Advanced High-Throughput Test System for Electrocatalytic Screening Applications Under Industrial Relevant Conditions - A Perspective to Accelerate Electrolysis Research and Development." Electrochemical Science Advances (2024): https://doi.org/10.1002/elsa.202400015.

The author contributions are shown in the list of publications on page vii.

Parts of the experimental data were obtained in the course of the Master's thesis 'Validation of a modular electrochemical test cell for application in the field of electrolysis screening' by Xuehuai Hou.

Key component for the operation of the high-throughput (HT) test system is the electrochemical flow cell. To meet all scientific and system-related requirements, a new HT flow cell was developed in collaboration between hte GmbH (Heidelberg), Fraunhofer Institute for Microengineering and Microsystems (IMM, Mainz), and Institute of Energy Technologies – Fundamental Electrochemistry (IET-1, Jülich). First, a comprehensive description of the flow cell and its functional features is provided. Subsequently, the results of the intensive experimental validation and characterization phase of the cell are presented. Finally, based on the findings of the experimental validation, design modifications for the flow cell are proposed to optimize its performance.

3.1 Cell description

The research conducted with the HT system will initially focus on water electrolysis (AWE and AEM WE) and CO_2 electrolysis processes (CO_2-to-CO, CO_2-to-HCOOH, and CO_2-to-C_{2+}), which requires the realization of different reactor concepts. A modular design has been developed to meet the varying requirements of the different processes and thus enable a variable operation. In the following section, the design of the HT flow cell is described in detail.

The cell consists of two symmetrical half-cells. Each half-cell housing has four fluid connections on the front, including inlet and outlet for the liquid electrolyte and additional connections for a gas phase (Figure 3.1a). Gas phase connections are required for gas diffusion electrodes, which play an important role in CO_2 electrolysis to increase the availability of CO_2[102]. At the rear of the housing, electrical and fluid connections for a heat transfer medium supply are provided (Figure 3.1b). Two electrical connections are available for each half cell. One connection leads directly to the current collector and the other to a metal contact frame attached to the inside of the cell housing (Figure 3.2b). The contact frame is intended to provide additional electrical contacting possibilities to extend

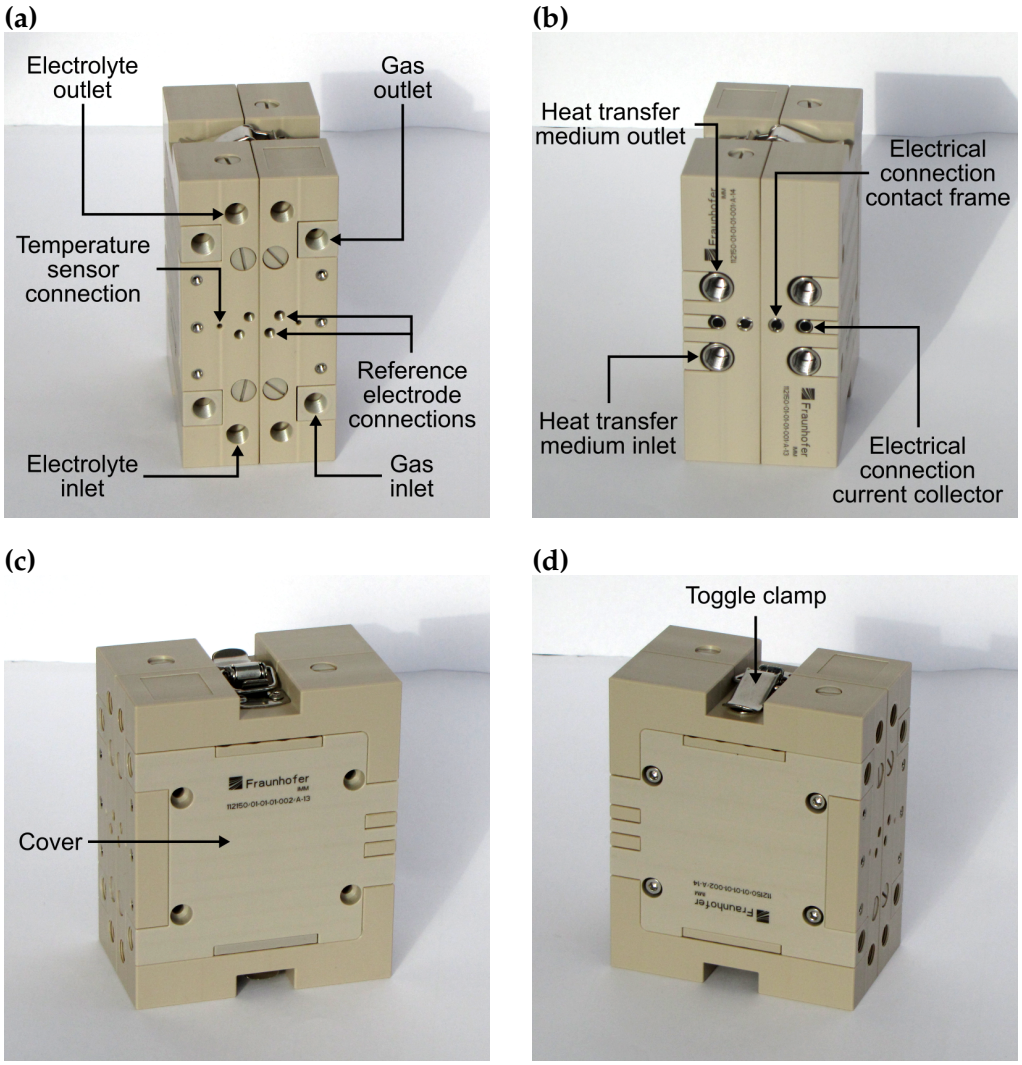

Figure 3.1: Images of the developed high-throughput flow cell: (a) front view, (b) rear view, and (c)+(d) side views.

the experimental capabilities of the HT cell. Use of the heat exchanger function is optional and is available to improve cell temperature control. The heat transfer medium is carried through the current collector via the respective connections.

Figure 3.1c and 3.1d show the side perspectives of the cell housing. The two symmetrical half-cell housings can be fastened together with a toggle clamp. Each half-cell housing can be opened by removing the

cover in order to install the current collector. Two different types of current collector were developed to enable the operation of different reactor configurations with the HT cell. The finite-gap current collector is used for foils or porous voluminous electrodes (foams). It also enables the participation of an additional gas phase and is therefore required for all GDE applications. Furthermore, the finite-gap configuration allows the implementation of a RE into the HT cell for 3-electrode applications. The zero-gap current collector is required for processes with membrane electrode assemblies (MEA) or thin mesh electrodes. Photos of the opened half-cells and schematic cross-sections of the finite-gap and zero-gap configuration are depicted in Figure 3.2.

For the application of RE in finite-gap configuration, each cell housing front is equipped with two additional threaded holes in which Luggin capillaries can be inserted into the cell via HPLC fittings (Figure 3.1a). The capillaries can be positioned either close to the electrode or close to the separator. A further small 1 mm hole is provided on the front, enabling a temperature sensor to be inserted into the current collector for precise in-cell temperature measurements.

The HT flow cell enables measurements with a geometric active electrode area of up to 19.4 cm^2. The active surface area can be individually reduced. In zero-gap configuration, area reduction is realized by customized flat gaskets. For finite-gap configuration, specially designed inlays are required to reduce the active area and electrolyte chamber accordingly. The assembled inlay can be seen in the photo of the open cell in Figure 3.2a.

The flow cell sealing concept is based on industry standard for stacked flow cells. Multiple cells are installed into a piston press, which exerts sufficient axial compression. This approach facilitates rapid installation of the flow cells into the system and uniform force distribution for improved electrode contacting. Furthermore, it enables the application of elevated process pressures up to 5 bar.

The housing, screw fittings, and inlays for electrode area reduction are made of inert polymers such as PEEK, PTFE or PP. The use of inert

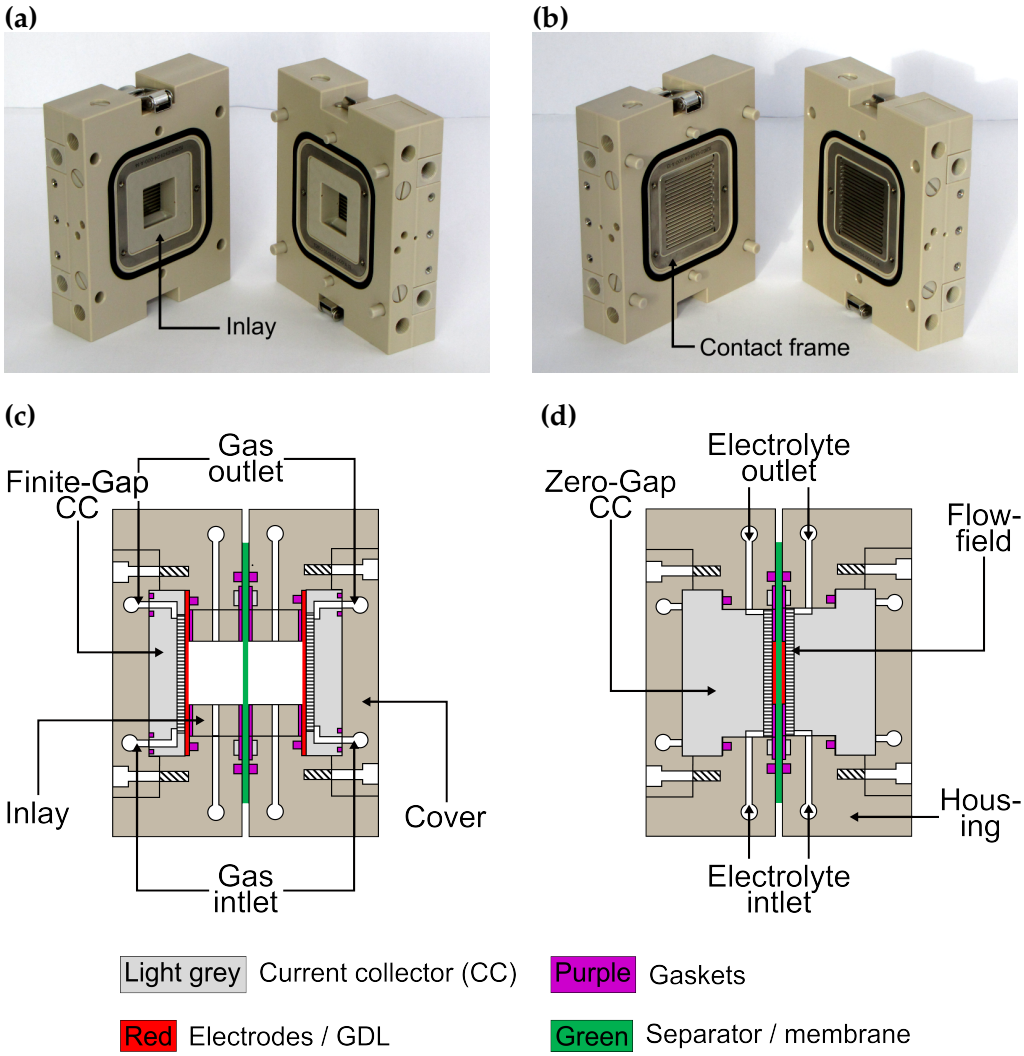

Figure 3.2: Image of the opened high-throughput flow cell in (a) finite-gap configuration and (b) zero-gap configuration. Schematic representation of the cross-section in (c) finite-gap configuration and (d) zero-gap configuration.

polymers allows the application of highly corrosive electrolyte solutions and thus increases the process variability. Current collectors and contact frames are made of Ti grade 5.

3.2 Validation and optimization experiments

This section presents the experimental results of the validation phase of the HT flow cell. The experimental validation serves to verify the different cell configurations and features by performing various common electrochemical methods. Furthermore, identifying optimization potentials to improve the cell performance and cell-to-cell comparability when operating multiple HT flow cells in parallel is of high priority. The section is divided into experiments in finite-gap configuration with AWE WE, zero-gap configuration with AEM WE and zero-gap configuration with AWE WE. Unless otherwise stated, all experiments were performed with an active electrode surface area of 5 cm^2, an electrolyte flow rate of 50 ml/min and electrochemical preconditioning for 1 h.

3.2.1 Finite-gap alkaline water electrolysis

The first experiments in finite-gap configuration involved testing the effects of diaphragm activation on AWE. Furthermore, the efficiency of the HT cell in finite-gap configuration is benchmarked to reference data of a commercial research cell. Prior to testing, the activated Zirfon separators were pre-saturated by immersion in 6 M KOH electrolyte for at least 24 h. A significant difference was observed between both measurements with and without the 24 h pre-saturation step of the Zirfon diaphragm. Figure 3.3a shows, that significantly lower voltages were measured, when the Zirfon diaphragm was pre-activated. The activation procedure led to a substantial decrease in cell voltage from 9.81 to 4.62 V at a current density of 500 mA/cm^2. The LSV results are supported by the EIS data (Figure 3.3b), which show a significant reduction in ohmic cell resistance from 2.80 to 0.82 Ω after Zirfon activation. However, a comparison with the reference data from a previously published paper still shows a large difference in efficiency. In this publication, a commercial flow cell (Micro Flow Cells® from ElectroCell A/S) was operated with AWE under similar conditions with 6 M KOH at 25 °C[2]. Nevertheless, the refer-

ence system shows a considerably lower maximum voltage of 2.98 V at 500 mA/cm^2.

The experimental results indicate that the lack of pre-activation severely impairs the performance of the cell. Insufficient or no pre-activation of the Zirfon separators promotes the accumulation of gases on the separator surface and the intercalation of gas molecules into the separator, leading to a gas-blanketing effect.[103,104] The activation of the diaphragm also reduced the noise in the polarization curve. The reduced noise may indicate a more stable ion transport due to the removal of gas bubbles from the diaphragm pores and pre-activation with electrolyte solution. The high ohmic losses in the HT cell compared to the reference system are likely caused by the electrolyte due to the large electrode spacing of 24 mm. In comparison, the reference data of the Micro Flow Cell® was measured with a significantly smaller electrode spac-

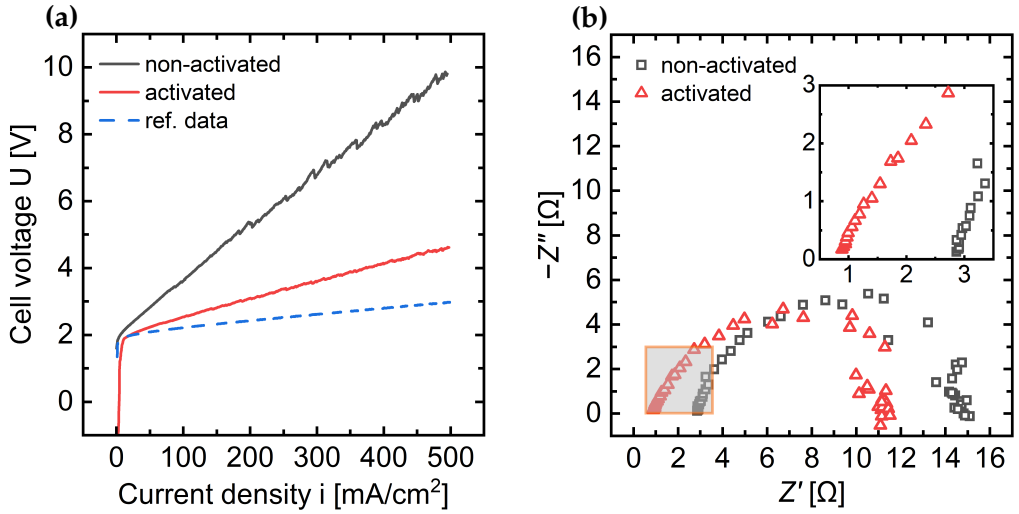

Figure 3.3: Effect of diaphragm activation tested with Zirfon UTP 220 and AWE in finite-gap configuration: (a) polarization curves and (b) electrochemical impedance spectroscopy data with activated (24 h pre-saturation in 6 M KOH) and non-activated diaphragm. Measurements were conducted at 20 °C with 6 M KOH and a flow rate of 50 mL/min. Prior to each measurement, the cell was conditioned at 0.5 A for 1 h. Reference data were recorded with a commercial flow cell under comparable conditions[2].

ing of approximately 4 mm. This spacing results from the thickness of two flow field frames and four compressed EPDM gaskets (cf. Table 2.6). High ohmic losses require high cell voltages, which cause additional heat losses. With increased current densities, this can lead to strong heat generation, which can be particularly critical in the field of catalyst research. Research into new gas diffusion electrodes for CO_2 electrolysis, which are particularly sensitive and have a limited durability, could therefore pose a challenge with the current finite-gap configuration design. To avoid such issues, the electrode distance in the current finite-gap design may be optimized.

The use of flat gaskets in the cell is required and serves various functions, depending on their position. First, they may have a sealing effect for the cell and protect against electrolyte leakage. Second, the active electrode surface size can be adjusted. Finally, the gasket thicknesses may be adjusted to achieve a proper press fit between the HT cell components and assembled materials with varying thicknesses. This ensures that sufficient electrode pressure and contact can be maintained. All gaskets required to assemble the flow cell in finite-gap configuration are depicted in purple in the schematic cross-section in Figure 3.4a. Due to its position, the labeled gasket between electrode and PEEK inlay is primarily used to adjust the press fit and does not seal against electrolyte leakage. The absence of this gasket could therefore help to achieve a proper press fit. The following study was intended to test the effect of the absence of the gasket on the cell performance during operation.

The effect of the absence of the flat gasket on cell performance was analyzed by polarization curve measurements (Figure 3.4b). The experiment was conducted with and without the gasket under otherwise identical conditions. Without the gasket, the cell voltage dropped from 4.78 to 4.62 V at 500 mA/cm^2. The decrease in cell voltage is consistent throughout the entire linear ohmic range and indicates a decrease in ohmic cell resistance. The polarization data show noise at elevated current densities, likely due to gas bubbles generated during the process adhering to the electrode surface. As these bubbles are removed by the electrolyte

flow, the removal causes transient availability of active reaction sites, resulting in time-dependent current fluctuations.

The significance of the use of the flat gasket is directly evidenced by the polarization data. The observed reduction in cell voltage in the absence of the gasket suggests electrolyte leakage between PEEK inlay and electrode, which increases the active electrode surface area in contact with the electrolyte. This enlarged surface area increases the number of reaction sites on the electrode surface, thereby decreasing the electron transfer per active area. Hence, the actual current density is reduced for a constant absolute cell current, lowering the overvoltages associated with the kinetic barriers of redox reactions, as described by the Tafel equation.[105] The gasket between electrode and inlay is therefore essential to accurately define the electrode surface area, which is crucial for precise investigation of e.g. electrode activity. Hence, operation of the HT flow cell without the flat gasket marked in Figure 3.4a is not recommended.

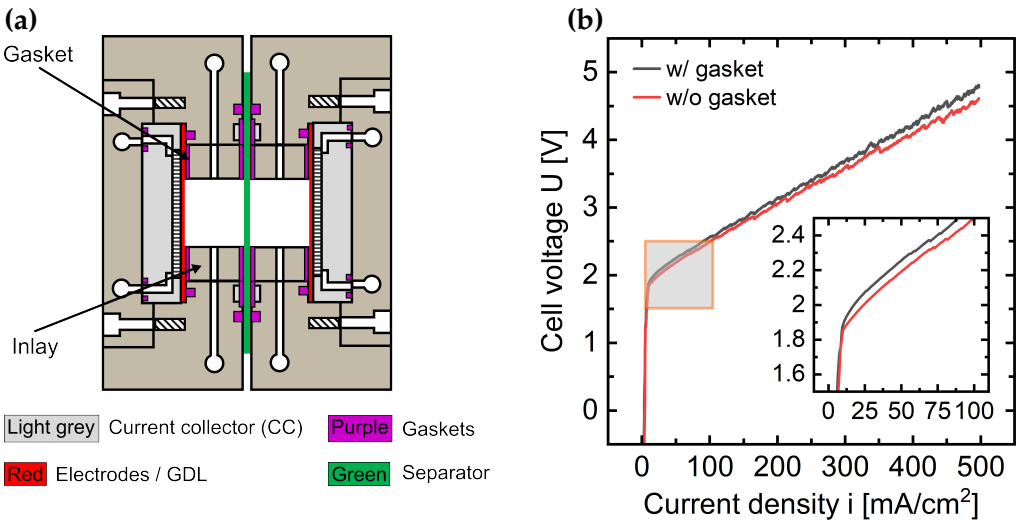

Figure 3.4: Effect of flat gasket usage: (a) schematic cross-section with labeled flat gasket and (b) polarization curves with and without flat gasket. Measurements were conducted at 20 °C with a flow rate of 50 mL/min. Prior to each measurement, the cell was conditioned at 0.5 A for 1 h.

Next, the finite-gap configuration was tested at increased operating temperatures. For this purpose, the HT cell was operated at 20, 40, and

60 °C (Figure 3.5). According to the polarization curve results presented in Figure 3.5a, the cell voltage decreased from 4.77 to 4.18 and 3.68 V with increasing temperature at 500 mA/cm^2. The cell voltage reduction is due to a decrease in the onset voltage as well as a decrease in the slope of the polarization curves, indicating a drop in cell resistance. Furthermore, a reduction in the polarization curve data noise is observed with increasing temperature. The ohmic cell resistance was obtained from the x-axis intercept at high frequencies extracted from the EIS results (Figure 3.5b). The reduction in cell resistance is confirmed by the EIS data, which show a decrease from 0.84 to 0.68 and 0.57 Ω at 20, 40, and 60 °C, respectively. The cell resistance $R_{c,EIS}$ obtained from EIS was compared with the resistances derived from the slope in the linear ohmic range of the polarization curves $R_{c,pol}$ and plotted in Figure 3.5c. Both resistance data sets show a linear decrease with increasing temperature. Figure 3.5d presents the difference between the resistance data sets ΔR_c, indicating a similar linear correlation.

An increase in operating temperature enhances the cell performance by increasing electrolyte conductivity, lowering Nernst voltages, and accelerating both redox and charge transport kinetics[106,107]. The onset voltage of the cell decreases as reaction kinetics and thermodynamic properties improve, as described by the Nernst equation[108]. Higher temperatures reduce the dynamic viscosity and lower the surface tension of the electrolyte, which decreases the critical diameter for gas bubbles to departure from the catalyst surface, which in turn lowers the signal noise of the polarization curve measurements[109,110]. The resistance difference declines with increasing temperature, suggesting that cell resistances derived from the polarization curve slopes capture a partial resistance component not reflected in the cell resistance from EIS. This resistance component is likely associated with the charge transfer resistance of kinetically controlled redox reactions, which decreases as temperature increases (Figure 3.5b).

So far, the cell has been tested only in 2-electrode configuration. However, the 3-electrode configuration, including a RE, is an important ap-

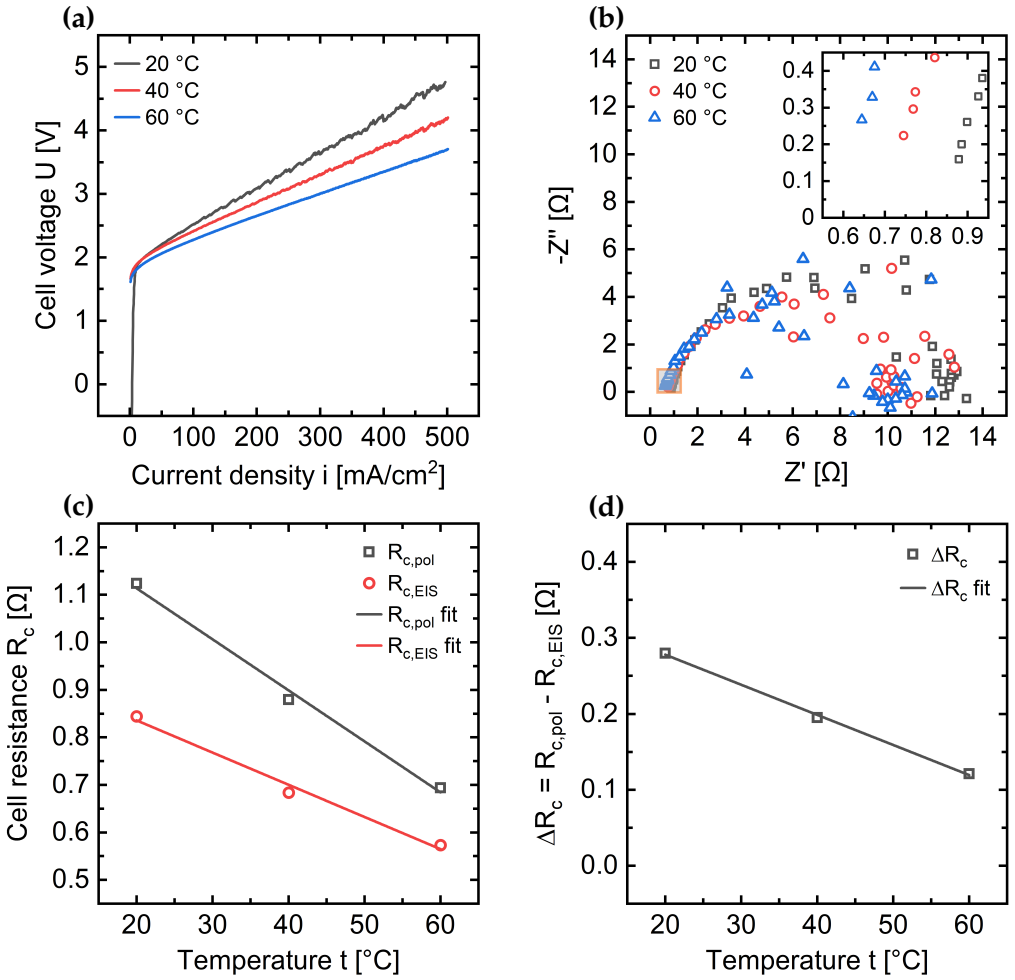

Figure 3.5: Finite-gap AWE tested at elevated operating temperatures. (a) polarization curves, (b) electrochemical impedance spectroscopy data, (c) temperature-dependent cell resistances derived from polarization curves $R_{c,pol}$ and electrochemical impedance spectroscopy results $R_{c,EIS}$, and (d) difference between cell resistance data sets ΔR_c. Measurements were conducted at 20, 40, and 60 °C with 6 M KOH and a flow rate of 50 mL/min. Prior to each measurement, the cell was conditioned at 500 mA/cm^2 for 1 h.

proach for catalyst and electrode research. The finite-gap configuration was designed to support the 3-electrode setup (Section 3.1), which was validated here with a Hg/HgO RE, Ni foil electrodes and Zirfon UTP 220 in 6 M KOH (Figure 3.6). CV measurements were conducted at different

scan rates from 5 to 20 mV/s and a step size of 0.2 mV at potentials in the range of the HER (Figure 3.6a) and in the range of OER (Figure 3.6b). The HER starts below -1.1 $V_{Hg/HgO}$ at the WE, which then serves as the cathode. The OER starts above 0.55 $V_{Hg/HgO}$ at the WE, which then serves as the anode. The CV scans show the expected oxidation and reduction

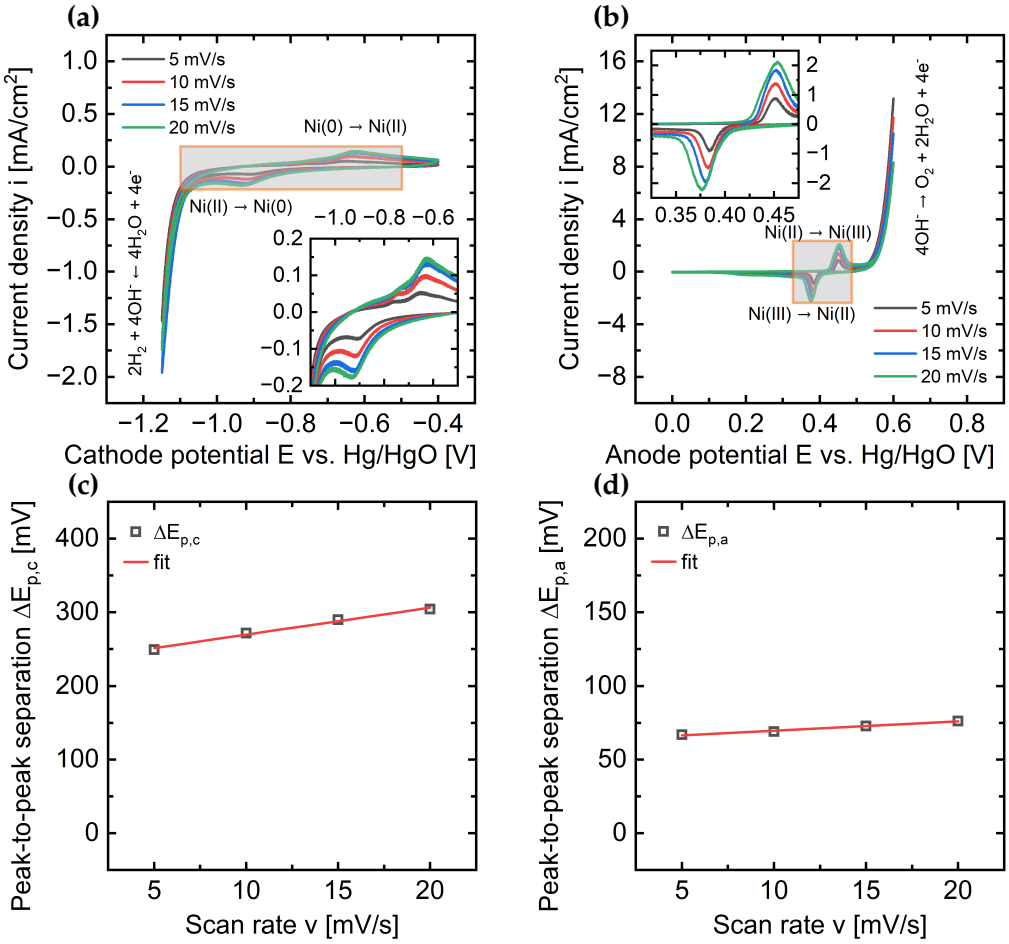

Figure 3.6: Finite-gap AWE operated in 3-electrode configuration. Cyclic voltammetry (0.2 mV step size) conducted within the (a) cathode potential range and (b) anode potential range at different scan rates of 5, 10, 15, and 20 mV/s. Oxidation and reduction peak-to-peak separation of scans within (c) cathode potential range and (d) anode potential range. Measurements were conducted using Hg/HgO reference electrode and Zirfon UTP 220 in 6 M KOH at 25 °C.

peaks: Ni(0) to Ni(II) and Ni(II) to Ni(0) at the cathode as well as Ni(II) to Ni(III) and Ni(III) to Ni(II) at the anode. As the scan rate increases, two phenomena can be observed in both CV scans, within the cathodic and anodic potential ranges. First, the magnitudes of the peak currents decrease. Second, the oxidation and reduction peak potentials shift, leading to an increase in peak-to-peak separation (PPS). The PPS were derived and plotted for all scans within the cathodic potential range (Figure 3.6c) and all scans within the anodic potential range (Figure 3.6d). The PPS analyzes reveal an increase from 249 to 304 mV at the cathode and from 67 to 74 mV at the anode.

CVs are a powerful method which was frequently applied in the literature, since parameters such as the heterogeneous electron transfer rate constant can be derived[111]. Therefore, the PPS constitutes a well-suitable quantity to validate the results of the 3-electrode measurements in comparison with literature data. Previous studies in comparable systems yielded approximately 90 mV at 10 mV/s at the anode[112] or 340 mV at 100 mV/s at the cathode[113]. Both results are in good agreement with the data presented in Figure 3.6c and 3.6d of the HT cell. Another commonly investigated quantity derived from CV data is the roughness factor f_R, which was calculated based on the reduction peaks of the anodic CV scans (Ni(III) to Ni(II) transition) according to Equation 2.1 and 2.2[101]. Based on the generated CV data, a roughness factor of 9.81 is calculated at 20 mV/s. This value is in good agreement with the literature, which provides values of $f_R < 10$ for smooth Ni foils[114]. The results of the roughness factor determination for all scan rates and the corresponding interim results are listed in Table A.1 in the appendix.

3.2.2 Zero-gap anion exchange membrane water electrolysis

After testing the HT flow cell in finite-gap configuration, the operation in zero-gap configuration was validated. All experiments in this section were conducted with AEM WE using commercial materials (cf. Ta-

ble 2.3). The zero-gap tests were initially performed with a conventional two-terminal sensing (2TS) method. The polarization curve recorded shows a remarkably high cell voltage of 4.02 V at 2 A/cm^2 (Figure 3.7a). Considering that the data was recorded in zero-gap configuration, the high overvoltages reported here cannot be caused by increased ohmic electrolyte losses as observed in finite-gap configuration (cf. Figure 3.3). To optimize the measured cell performance, two variants of a four-terminal sensing (4TS) were developed. First, the $4TS_{cc}$ was conducted via the current collectors. Second, the $4TS_{frame}$ was conducted via the contact frame. Ni foil strips (Design 1) were used as conductive element to contact the electrode with the contact frame. Detailed information on both variants of the 4TS and the conductive element used herein can be found in Section 2.3.1. The $4TS_{cc}$ significantly reduced the cell voltage at 2 A/cm^2 to 3.60 V. Sensing through the contact frame ($4TS_{frame}$) further reduced the terminal voltage to 3.11 V. The shapes of the polarization curves indicate, that the cell performance was improved by decreasing the measured ohmic resistance, which was supportively analyzed by EIS measurements (Figure 3.7b). The cell resistances were derived from both the polarization curve slopes $R_{c,pol}$ (Figure 3.7c) and the high frequency x-intercepts of the EIS data $R_{c,EIS}$ (Figure 3.7d). $R_{c,pol}$ shows a decrease from 0.22 to 0.18 and 0.13 Ω for 2TS, $4TS_{cc}$, and $4TS_{frame}$, respectively. The $R_{c,EIS}$ results confirm the observed trend with a reduction from 0.12 to 0.09 and 0.08 Ω.

The 2TS results, presented in Figure 3.7, revealed a notably high partial ohmic resistance in the current collectors. Such high resistance components are particularly critical for cell configurations with actually very low resistance, such as the zero-gap setup. The 2TS would therefore impede the conduction of e.g. membrane screenings, as small material-related resistance deviations can hardly be measured ($R_{PiperION} \cdot A = 0.026\,\Omega \cdot cm^2$ at 20 °C[115]). The resistance reduction when switching the sensing method from 2TS to $4TS_{cc}$ is likely associated with a shorter distance between the sensing probe and the electrodes. Furthermore, Ti tends to form surface oxide-based passivation layers, which

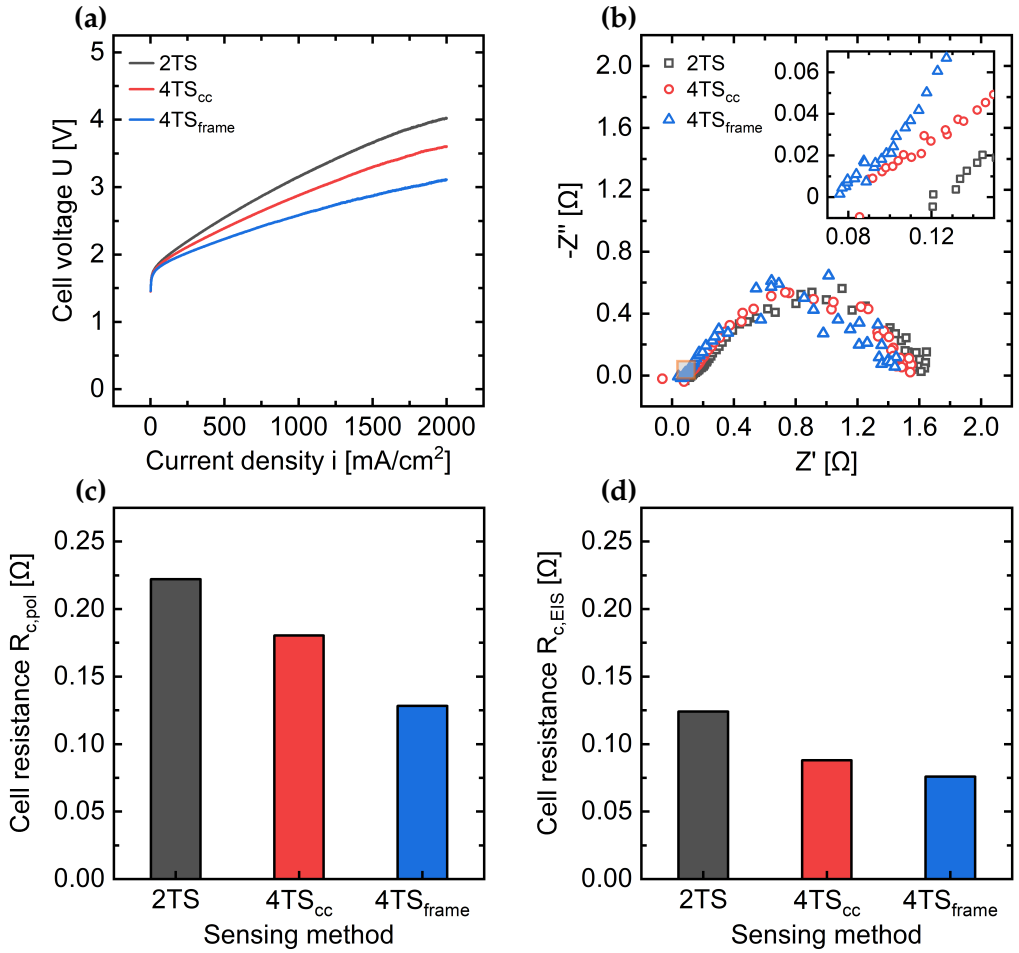

Figure 3.7: Zero-gap AEM WE tested with different sensing methods: two-terminal sensing (2TS), four-terminal sensing via current collectors ($4TS_{cc}$), and four-terminal sensing via contact frame ($4TS_{frame}$) with conductive element $D_{1,Ni/Ni}$. (a) Polarization curves, (b) electrochemical impedance spectroscopy data, (c) cell resistances derived from polarization curves $R_{c,pol}$, and (d) cell resistances derived from electrochemical impedance spectroscopy data $R_{c,EIS}$. Measurements were conducted at 20 °C with 1 M KOH and a flow rate of 40 mL/min. Prior to each measurement, the cell was conditioned at 1000 mA/cm^2 for 1 h.

cause high contact resistances[116–118]. The data indicate that the current collectors of the HT cell have formed such passivation layers on the surface causing high contact resistances. This contact resistance differs from current collector to current collector and depends on the individual his-

tory of the respective component. Thus, cell-to-cell comparability in the final HT system would be severely impaired. With the $4TS_{frame}$ this contact resistances are bypassed in the measure circuit, which further reduce the measured ohmic resistance and improves comparability.

The zero-gap configuration was further tested with the developed 4TS via the contact frame using contact element Design D_1 (cf. Figure 2.2). Instead of Ni strips in both half cells ($D_{1,Ni}$), Au strips were now used as conductive elements on the cathode side ($D_{1,Au/Ni}$). The setup was tested at increasing temperatures from 20 to 60 °C (Figure 3.8). Polarization curves were recorded and are depicted in Figure 3.8a. Increasing the temperature leads to the expected improvement in cell efficiency, resulting in a decrease in voltage at 2 A/cm^2 from 2.88 to 2.45 and 2.27 V at 20, 40 and 60 °C, respectively. In addition, EIS measurements were carried out for further analysis (Figure 3.8b). The EC impedance spectra show a shift of the high-frequency x-intercept, which indicates a reduction of the ohmic cell resistance with increasing temperature and confirms the observed trend of decreasing slope in the linear ohmic range of the polarization curves. The cell resistance values were determined both from the slope of the polarization curve ($R_{c,pol}$) and from the EIS data ($R_{c,EIS}$) and are shown in Figure 3.8c and 3.8d as a function of temperature. The 2TS, $4TS_{cc}$, and $4TS_{frame}$ $D_{1,Ni}$ data were additionally included in both data sets for a better overview. The data show a significant reduction in the ohmic cell resistances $R_{c,pol}$ and $R_{c,EIS}$ over the entire temperature range by optimizing the sensing method from 2TS over $4TS_{cc}$ to $4TS_{frame}$. The substitution of Ni strips with Au strips in the cathodic half-cell further reduced the cell resistance from 0.128 to 0.111 Ω ($R_{c,pol}$) or from 0.076 to 0.046 Ω ($R_{c,EIS}$) at 20 °C.

Both, the hydroxide conductivity of the PiperION®membrane and the electrolyte conductivity of 1 M KOH increases with increasing temperature[115,120], leading to the observed temperature-dependent drop in cell resistance in Figure 3.8. The application of Au as cathodic conductive element reduces the cell resistance due to the lower electrical resistivity. At 20 °C, the electrical resistivity of Au is $2.21 \cdot 10^{-8}$ Ω·m com-

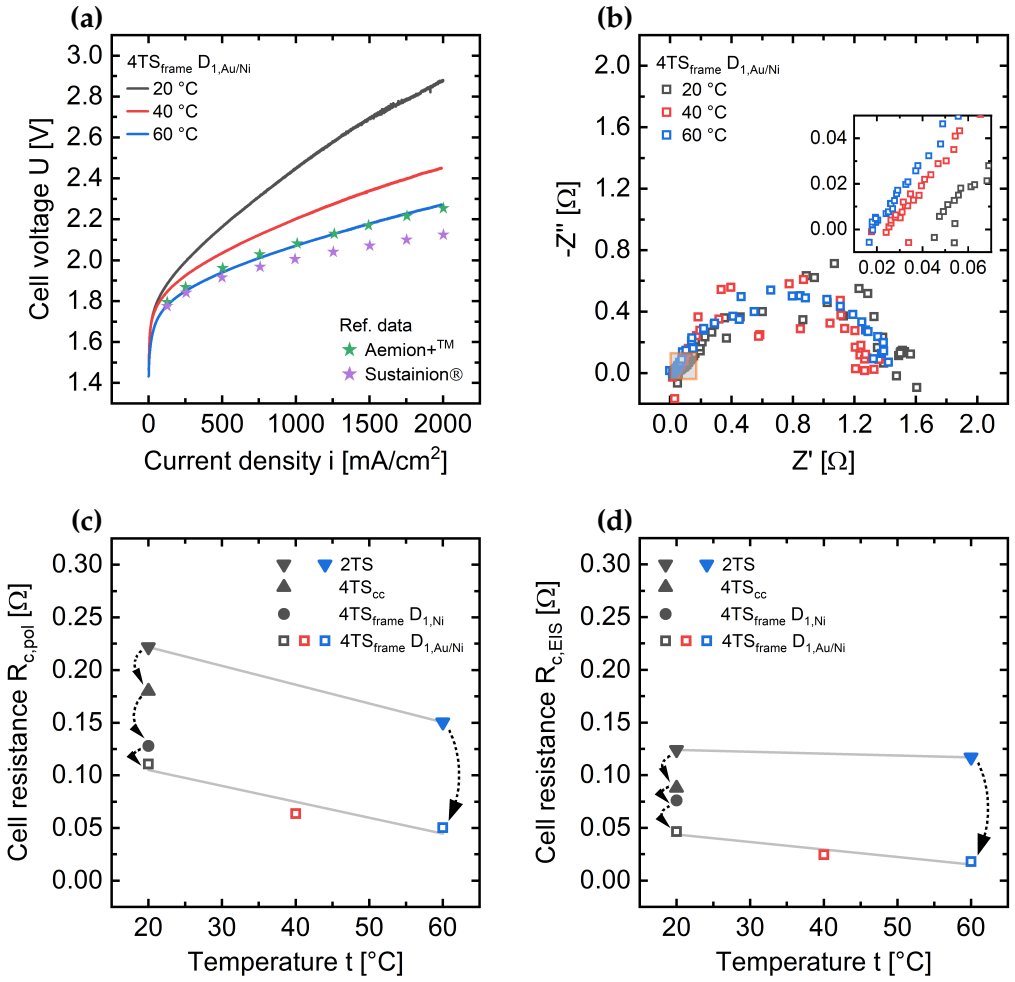

Figure 3.8: Zero-gap AEM WE tested at elevated operating temperatures using $4TS_{frame}$ with conductive element $D_{1,Au/Ni}$. (a) Polarization curves, (b) electrochemical impedance spectroscopy data, (c) cell resistances derived from polarization curves $R_{c,pol}$, (d) and cell resistances derived from electrochemical impedance spectroscopy data $R_{c,EIS}$. Measurements were conducted at 20, 40, and 60 °C with 20 µm PiperION membrane, 1 M KOH, and a flow rate of 40 mL/min. Prior to each measurement, the cell was conditioned at 2000 mA/cm² for 1 h. Reference polarization curves were recorded at 60 °C with 1 M KOH and Aemion+™ or Sustainion® membrane[119].

pared to $6.93 \cdot 10^{-8}$ of Ni[121]. Figure 3.8a additionally shows reference data from the literature. The reference polarization curves were recorded

under comparable conditions (1 M KOH, 60 °C) with different commercial membranes in a flow cell purchased from Dioxode Materials[119]. The benchmarking proves that the developed $4TS_{frame}$ method enables a competitive efficiency operating the HT flow cell compared to the literature references.

Repeat experiments showed that the data reproducibility of the current conductive element design D_1 was challenging. However, reliable reproducibility with the HT flow cell is required to ensure good cell-to-cell comparability, which is a prerequisite for the application in the HT system. Furthermore, the strip shape of the conductive elements causes a non-uniform force distribution on the electrodes. In prolonged experiments, this can lead to mechanical failure of the membrane or damage to other components[122]. Despite the improved efficiency already achieved with the developed $4TS_{frame}$, this sensing approach must therefore be further optimized by testing different materials and designs for the conductive element. Details of the designs tested can be found in Figure 2.2. Polarization curves and EC impedance spectra were recorded for all conductive element designs and the cell resistances were calculated from both data sets for further analysis (Figure 3.9). D_0 was tested in pre-studies prior to D_1 and yielded significantly higher voltages, as there is very limited surface contact with the electrode (Figure 3.9a). With D_0 the electrode contact is achieved by a narrow overlap with the conductive element, which led to an increased contact resistance, as depicted in Figure 3.9b. As previously shown in Figure 3.8, the cell performance was improved with D_1 measurements by using Au instead of Ni due to the lower electrical resistance. D_2 was tested in zero-gap configuration with AWE and is therefore not shown here. D_3 and D_4 were developed to further optimize the conductive element. Both designs have a large electrode contact surface area and a structure that ensures improved force distribution on the electrode. The resulting cell voltages (Figure 3.9a) and derived cell resistances (Figure 3.9c and 3.9d) of D_3 and D_4 are competitive with the D_1 results. The deviations between $D_{1,Au/Ni}$, D_3 and D_4 are in the range of 30 mV and likely associated with experimental errors.

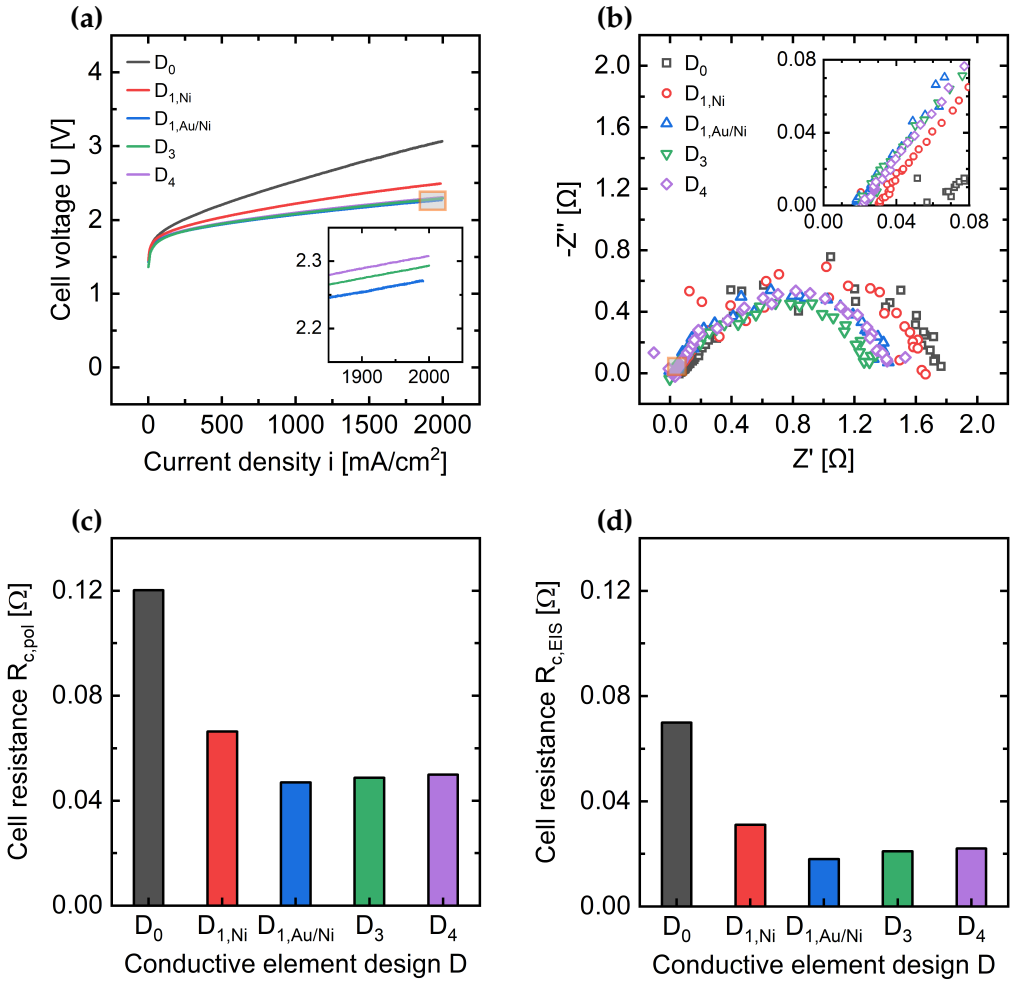

Figure 3.9: Zero-gap AEM WE using $4TS_{frame}$ tested different conductive element designs. (a) Polarization curves, (b) electrochemical impedance spectroscopy data, (c) cell resistances derived from polarization curves $R_{c,pol}$, and (d) cell resistances derived from electrochemical impedance spectroscopy data $R_{c,EIS}$. Measurements were conducted at 60 °C with 1 M KOH and a flow rate of 40 mL/min. Prior to each measurement, the cell was conditioned at 2000 mA/cm² for 1 h.

D_3 and D_4 differ primarily in their material structure. For D_3, a 50 µm thin Ni mesh was used. One concern here is that the thin mesh structure can deform, hampering the reproducibility of the data or the reuse of the conductive element. The conductive element D_4 is made of Ni foil and was developed to have a more stable structure that ensures reliable

electrode surface contacting, uniform force distribution, and mechanical stability to reduce contact resistance while minimizing mechanical stress on the electrode and maximizing durability of the conductive element. Therefore, the $4TS_{frame}$ using D_4 was applied for all subsequent measurements.

Insufficient reproducibility was a major issue with the previous conductive element designs. In this study, it was verified whether the reproducibility of the data could be evidentially improved with the optimized design D_4. For this purpose, the experiment was repeated, with the conductive elements being replaced in each trial. Figure 3.10 shows the average polarization curve of a total of three different independently recorded data sets. The HT cell achieves an average cell voltage of 2.30 V with a standard deviation of around 11 mV at 2 A/cm^2 and 60 °C, corresponding to a relative deviation of only 0.5 %. The experimental results confirm that the conductive element D_4 ensures improved reproducibility of the measurement data while providing a uniform force distribution on the electrode as well as low electrical contact resistance.

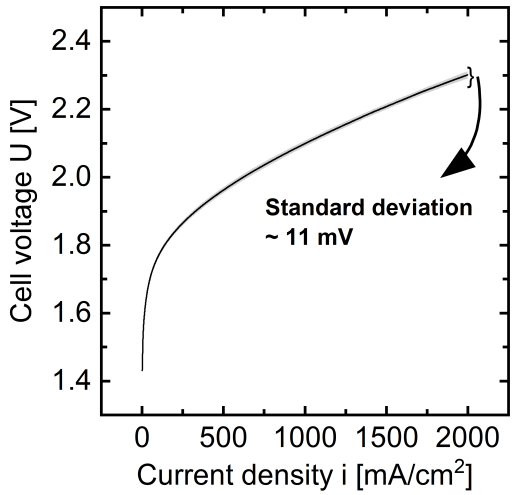

Figure 3.10: Zero-gap AEM WE reproducibility study using $4TS_{frame}$ with D_4. Polarization curve represents the mean of three individual experiments. Measurements were conducted at 60 °C with 1 M KOH and a flow rate of 40 ml/min. Prior to each measurement, the cell was conditioned at 2000 mA/cm^2 for 1 h.

High resistances caused by secondary components such as the current collectors, do not only impair the cell-to-cell comparability in the final system and negatively affect the efficiency. If these resistances are predominate in the flow cell, the cell design may be unsuitable for certain research applications, as small changes e.g. in material resistance are hardly measurable. The $4TS_{frame}$ method was developed to bypass the high resistance of the Ti grade 5 current collectors. A membrane screening was performed to validate that the optimized sensing method provides a sufficiently low cell resistance to detect measurable changes in the electrical signals.

For this purpose, PiperION® membranes of different thicknesses from 20 to 60 µm were tested. The polarization curves are presented in Figure 3.11a and show a clear improvement in cell performance with decreasing membrane thickness. At 2 A/cm^2, the voltage reduces from 2.49 to 2.38 to 2.29 V. In the respective EC impedance spectra (Figure 3.11b), a shift of the high-frequency X-intercept can be observed, which confirms that the reduction of the cell voltage is due to a decreasing cell resistance. The cell resistances $R_{c,pol}$ (Figure 3.11c) and $R_{c,\,EIS}$ (Figure 3.11d) were calculated from the two data sets and plotted as a function of membrane thickness. Both $R_{c,pol}$ and $R_{c,EIS}$ increase linearly with increasing membrane thickness d_{mem}, demonstrating the expected ohmic resistor property of the membranes.

$\Delta R_{c,pol}/\Delta d_{mem}$ and $\Delta R_{c,EIS}/\Delta d_{mem}$ show a similar slope with a mean difference of 30 mΩ. The slope of the cell resistance can be used to calculate the specific membrane resistance $\rho_{PiperION}$, which is 25.6 and 21.5 Ω·cm, respectively. Based on the specific membrane resistance a specific hydroxide conductivity $\sigma_{PiperION}$ of 39.1 and 46.5 mS/cm is derived. These values are in a similar range to the literature values of comparable systems ($\sigma_{PiperION,literature}$ = 155 mS/cm at 60 °C[123]).

The data presented in Figure 3.11 confirm that the measured resistance of the optimized sensing method using conductive element D_4 could be reduced to a satisfactory level. Material-related changes to the cell resistance in the mΩ range led to clearly measurable alterations to

the electrical signals, enabling further analysis. The membrane screening validation demonstrated the suitability of the HT cell for material or process parameter screenings.

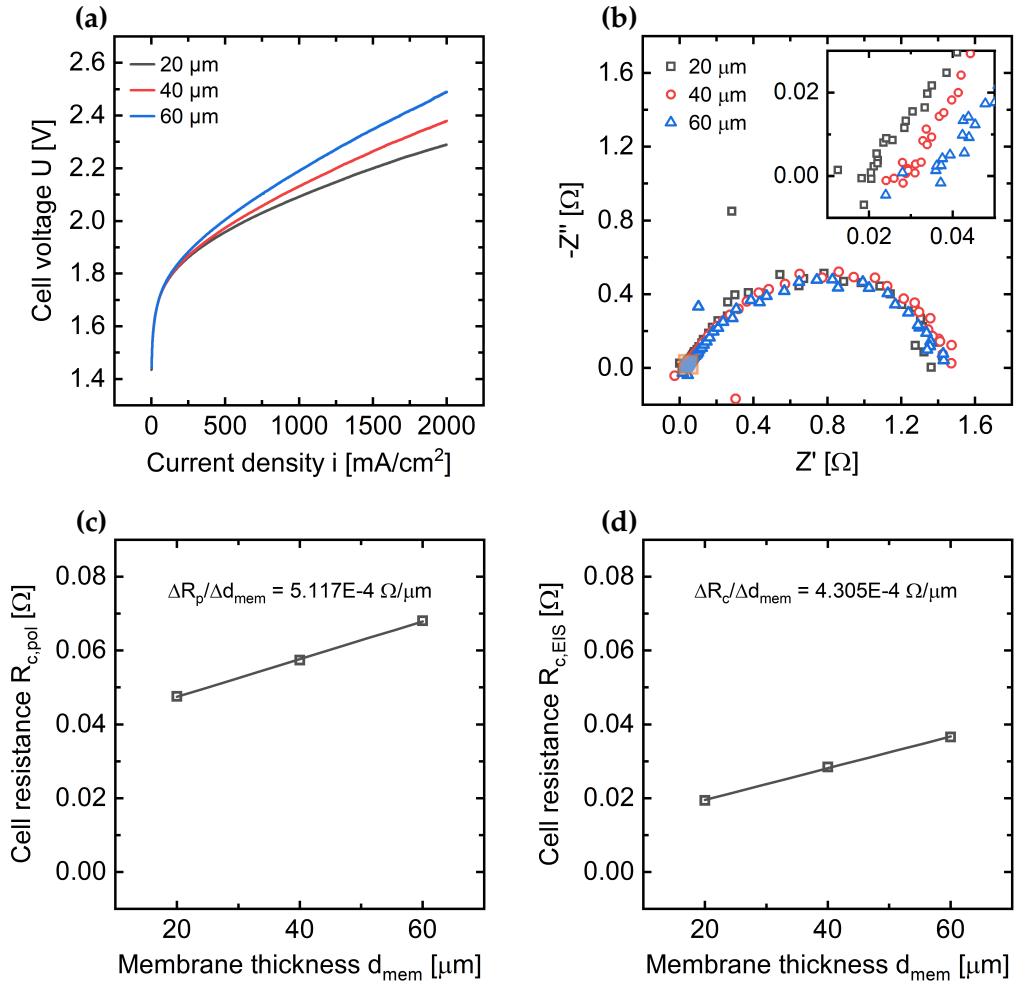

Figure 3.11: Zero-gap AEM WE PiperION membrane screening using $4TS_{frame}$ with D_4. (a) Polarization curves, (b) electrochemical impedance spectroscopy data, (c) cell resistances derived from polarization curves $R_{c,pol}$, (d) and cell resistances derived from electrochemical impedance spectroscopy data $R_{c,EIS}$. Measurements were conducted with 20, 40, and 60 µm PiperION membrane at 60 °C with 1 M KOH and a flow rate of 40 mL/min. Prior to each measurement, the cell was conditioned at 2000 mA/cm² for 1 h.

3.2.3 Zero-gap alkaline water electrolysis

For further cell validation and testing of the previously developed $4TS_{frame}$, the optimized sensing method was tested in this section with AWE in zero-gap configuration. Details on the commercial materials that were used for the following experiments can be found in Table 2.2.

To test the effect of the $4TS_{frame}$ D_4 on the AWE zero-gap configuration, the optimized sensing method was compared to the 2TS and $4TS_{cc}$. The high resistance of the current collectors leads to an increased cell voltage of 2.76 V at 500 mA/cm^2 when using 2TS. The HT cell shows an improved performance with the $4TS_{cc}$ reaching 2.52 V. With the $4TS_{frame}$ method, the maximum cell voltage is further reduced to 2.42 V. The cell resistances $R_{c,pol}$ derived from the recorded polarization curves are presented in Figure 3.12b. The cell resistance data show a decrease in cell resistance from 0.26 to 0.18 and 0.14 Ω by switching the sensing method.

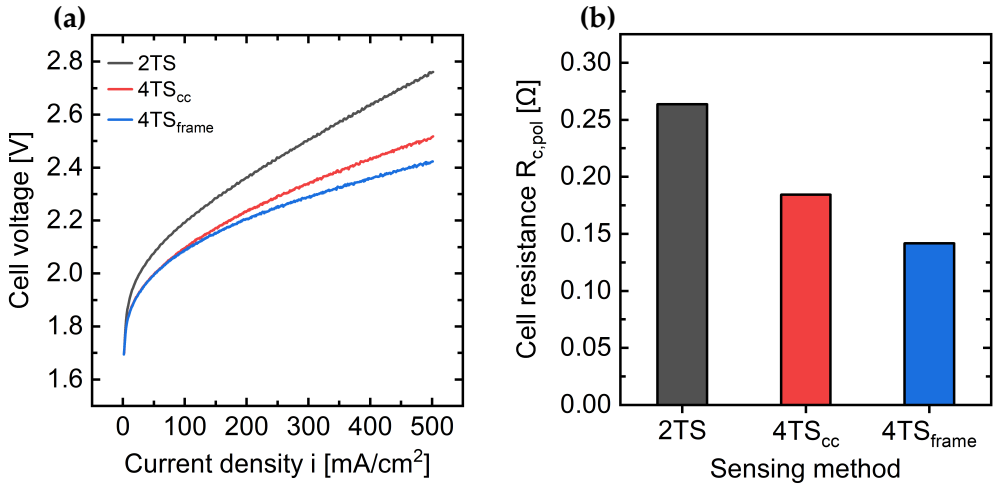

Figure 3.12: Zero-gap AWE tested with different sensing methods: two-terminal sensing (2TS), four-terminal sensing via current collectors ($4TS_{cc}$), and four-terminal sensing via contact frame ($4TS_{frame}$) with conductive element D_4. (a) Polarization curves and (b) cell resistances derived from polarization curves $R_{c,pol}$. Measurements were conducted at 20 °C with 6 M KOH and a flow rate of 50 mL/min. Prior to each measurement, the cell was conditioned at 500 mA/cm^2 for 1 h.

With the optimized sensing method high current collector resistances are bypassed. When switching from 2TS to $4TS_{cc}$, the electrical signals are still measured through the current collector. However, the distance between the sensing point and the electrode is shortened, which significantly reduces the electrical resistance while measuring through the Ti grade 5 current collectors ($\rho_{\mathrm{Ti\,Gr\,5}} = 178 \cdot 10^{-8}\,\Omega\cdot$m). Ti surfaces tend to form passivation layers on the surface, which cause high contact resistances[116–118]. They can lead to aging-related resistance differences between the parallel flow cells and significantly impair comparability when operating the HT system. When sensing through the contact frame, the contact resistance of the current collector is bypassed, which ultimately improves the comparability of the system.

The AWE zero-gap configuration was then tested at elevated temperatures. For this purpose, polarization curves and EC impedance spectra were recorded at 20, 40 and 60 °C. The experimental results are shown in Figure 3.13. The polarization curves show a decrease in cell voltage with increasing temperature from 2.42 to 2.37 and 2.31 V (Figure 3.13a). The voltage decrease is due to the reduction of the onset potential and the reduction of ohmic losses, which is characterized by the decreasing slope in the linear region. Further analysis is enabled by plotting the EC impedance spectra (Figure 3.13b). The slight shift of the high-frequency x-intercept confirms that the reduction in ohmic losses is due to a reduction in cell resistance. The cell resistance was calculated from the slope of the polarization curves in the linear ohmic loss region ($R_{c,pol}$, Figure 3.13c) and from the high-frequency x-intercept of the EIS data ($R_{c,EIS}$, 3.13d). Both $R_{c,pol}$ and $R_{c,EIS}$ decrease with increasing temperature. $R_{c,pol}$ decreases from 0.142 (20 °C) to 0.124 Ω (60 °C), while $R_{c,EIS}$ decreases from 0.038 to 0.026 Ω in the same temperature range. The constant deviation of both quantities of approximately 0.1 Ω is likely associated with temperature-independent transport effects.

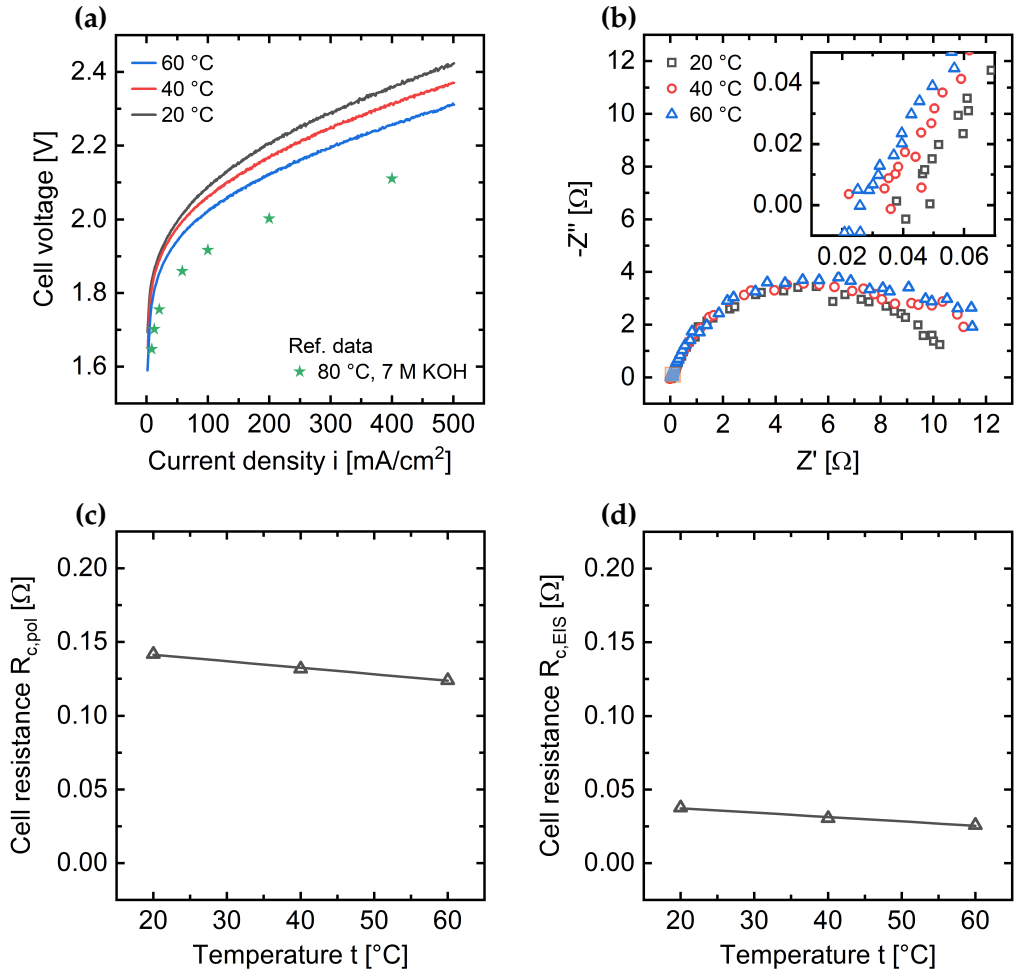

Figure 3.13: Zero-gap AWE tested at elevated operating temperatures using $4TS_{frame}$ with D_4. (a) Polarization curves, (b) electrochemical impedance spectroscopy data, (c) cell resistances derived from polarization curves $R_{c,pol}$, and (d) cell resistances derived from electrochemical impedance spectroscopy data $R_{c,EIS}$. Measurements were conducted at 20, 40, and 60 °C with 6 M KOH and a flow rate of 50 mL/min. Prior to each measurement, the cell was conditioned at 500 mA/cm² for 1 h. The reference polarization curve was recorded with a comparable system at 80 °C with 7 M KOH[124].

The data in Figure 3.13 show that temperature-induced changes in the cell resistance lead to clearly measurable alterations in the electrical signals (I-U and EIS signals), confirming the suitability of the HT cell for

process temperature screenings using $4TS_{frame}$ with D_4. In addition to the polarization curves recorded, Figure 3.13a shows a reference plot from literature. The literature data were recorded at a slightly higher temperature and a higher KOH concentration. Considering the temperature and electrolyte concentration difference, the HT cell developed in this work shows a competitive performance compared to the literature data when using the optimized sensing method.

3.3 Cell modifications

During the experimental validation (Section 3.2), the performance of the HT flow cell was validated by testing different cell configuration and processes using common electrochemical methods. The identification of optimization potential was a further integral part of the validation phase. This chapter discusses modifications to optimize the performance and cell-to-cell comparability of the developed flow cell.

3.3.1 Implemented modifications

This section discusses component modifications that were implemented and tested in the course of this work. First, inlays with a modified design for the finite-gap configuration were tested. Subsequently, optimization of the current collector flow field design is discussed. Finally, experimental data of current collectors with precious metal coatings are presented.

Inlay chamfer

During the experimental validation of the finite-gap configuration, noise in the polarization data was found to increase with rising current density (cf. Figure 3.4b). This noise is likely associated with a disturbed removal of the generated gas bubbles from the electrode surface. To reduce the noise when using the inlays, a modified design was developed and tested. Figure 3.14a presents the original inlay design, in which the inlet

and outlet channels were drilled into the inlay frame without any further modifications. The geometry of the inlay creates a 90° angle between the active electrode surface and the inlay frame. Using the original design, the generated gas bubbles gather at this edge and agglomerate during operation. A modified inlay design was developed in which the inlet and outlet channels are equipped with a chamfer (Figure 3.14b). The chamfer increases the 90° angle between the electrode and the inlay frame, which should improve the removal of bubbles from the electrode surface and prevent large bubble agglomerations. The modified inlay design was fabricated in three variants with chamfer angles of 15, 30 and 45°.

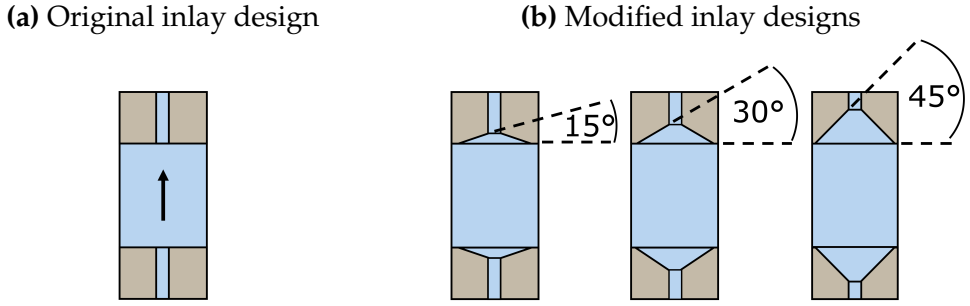

Figure 3.14: Schematic cross-section of PEEK inlays. (a) Original inlay design and (b) modified inlay designs. Modified inlays are provided with a chamfer of 15, 30, or 45°.

The three modifications of the inlay design were tested in finite-gap configuration with AWE and compared with data recorded with the original design. The experimental results are shown in Figure 3.15. It can be observed that the polarization curves already show a reduction in noise with a chamfer angle of 15°, confirming the hypothesis that the gas bubbles generated can be better removed in inlays with chamfer. Increasing the chamfer to 30 or 45°does not result in any further noticeable improvement in noise reduction. However, the polarization curves indicate a second chamfer-induced effect. As the angle increases, the cell voltage decreases, resulting in a voltage drop from 4.81 to 4.68, 4.57 and 4.49 V at 500 mA/cm^2. The cell resistance was derived from the slopes of the polarization curves in the linear ohmic loss range and plotted as a function

of chamfer angle (Figure 3.15b). The cell resistance decreases from 1.12 to 0.99 Ω with increasing chamfer angle.

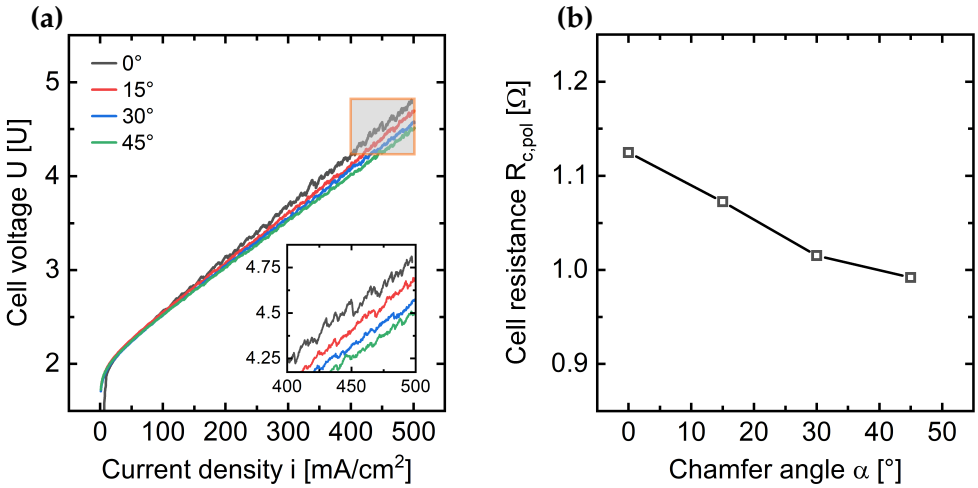

Figure 3.15: Effect of modified PEEK inlays on signal noise with finite-gap AWE. (a) Polarization curves and (b) cell resistances derived from electrochemical spectroscopy data $R_{c,EIS}$. Measurements were conducted with original and modified inlays with different chamfer angles of 15, 30, and 45°at 20°C with 6 M KOH and a flow rate of 50 mL/min. Prior to each measurement, the cell was conditioned at 500 mA/cm² for 1 h.

When using the original design, the electric field lines permeate straight through the electrolyte between both electrodes. In the modified design the chamfer temporarily increases the cross-section of the electrolyte chamber allowing the field lines to expand into the additional electrolyte volume. Therefore, the relevant cross-sectional area of the flow cell becomes larger than the geometric area of the electrode. As the relevant cross-sectional area increases, lower cell voltage is required at constant current. With increasing chamfer angle, the additional electrolyte volume and thus the expansion of the field increases leading to a further decrease in cell voltage. This effect must be further investigated and considered when using PEEK inlays with chamfer in the HT flow cell.

Flow field modification

The original flow field design of the current collectors provides parallel channels (Figure 3.16a). A disadvantage of this design is that individual channels are completely covered when the active area is reduced (red channels). The fluid in the covered channels does not flow past the electric field permeating through the electrolyte chambers and therefore cannot participate in the reaction. Only the fluid flowing through the uncovered channels (green) can be electrochemically converted. However, in processes such as electrochemical CO_2 reduction, it is important

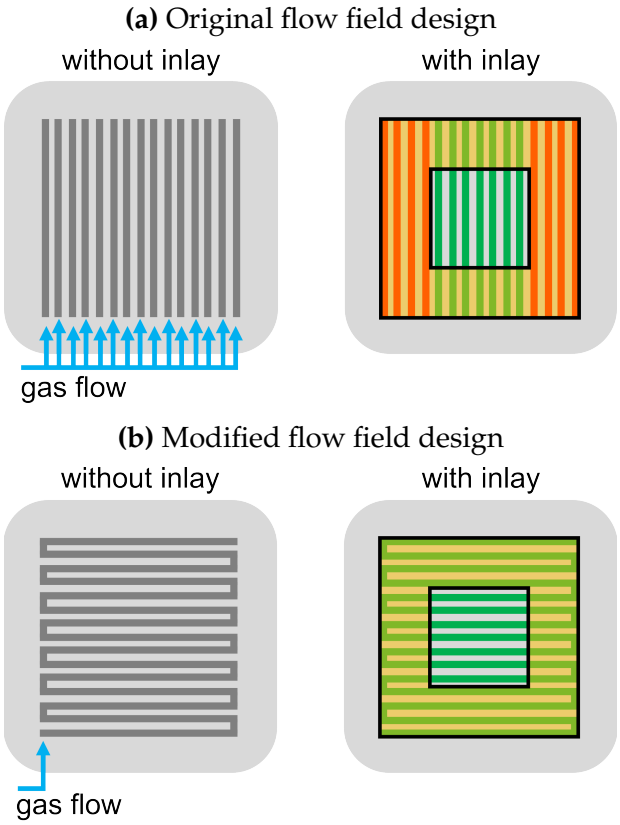

Figure 3.16: Schematic illustration of (a) original flow field design providing parallel fluid channels and (b) modified flow field design providing a single meandering fluid channel. Modified design prevents fluid in flow field channels to be excluded from the reaction by PEEK inlay (right).

to analyze how much of the supplied feed gas has been converted to the desired product. The application of the original flow field design considerably complicates the determination of such conversion rates. To solve this issue, a modified design was developed (Figure 3.16b), which provides only a single meandering channel for the fluid. The meandering channel structure ensures that the entire fluid flows past the electric field, even if the active electrode surface area is reduced. Application of the modified flow field design simplifies the determination of conversion rates and is therefore particularly recommended for processes with gas diffusion electrodes in finite-gap configuration, such as the electrochemical CO_2 reduction.

It should be noted that the meandering channel structure has further effects. First, for a given input gas flow rate, the flow velocity in the flow field with one channel is higher than with multiple parallel channels. Second, the channel length and therefore the pressure loss across the flow field is greater with one channel. These effects must be taken into account and their impact on the electrochemical CO_2 reduction must be validated.

Current collector precious metal coatings

During the validation experiments (cf. Section 3.2), a significantly high cell resistance was identified. The material from which the current collectors of the HT cell were fabricated (Ti grade 5) is prone to form oxide passivation layers on the surface. It was hypothesized that the passivation layers formed on the current collector surfaces cause high contact resistances, which would impair the comparability between parallel operated flow cells in the HT system. By developing the $4TS_{frame}$, it was possible to bypass the current collectors and significantly reduce the measured resistance. Due to the complexity of the 4TS developed here, this approach does not represent an ideal long-term solution for the system. Therefore, the aim is to minimize the current collector contact resistance to enable direct measurement through the current collectors without impairing the

cell-to-cell comparability. In order to reduce the contact resistance, the Ti grade 5 surfaces were electroplated. For this purpose, the precious metals platinum and gold were selected for the anode and cathode sides, respectively (Figure 3.17).

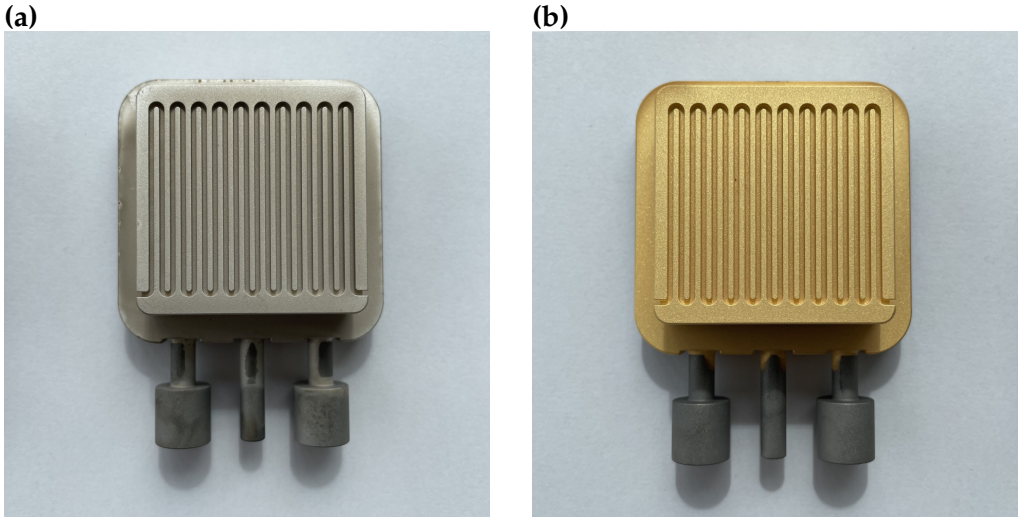

Figure 3.17: Images of precious metal coatings on the current collectors. (a) Pt was coated on anodic current collector and (b) Au was coated on cathodic current collector.

Comparative measurements were carried out with the coated current collectors in zero-gap configuration with AEM WE. The polarization curves are shown in Figure 3.18 with the previously recorded 4TS measurements via the uncoated current collectors and via the contact frame as well as benchmarking data from the literature. It can be observed that the cell voltage could be reduced from 2.29 to 2.19 V at 2 A/cm^2 when measuring via 4TS$_{cc}$ through the coated current collectors (red solid line) compared to the measurement via the contact frame 4TS$_{frame}$ (black dashed line). Thus, the previously measured minimal terminal voltage of the HT cell with AEM WE at 2 A/cm^2 was further improved by 100 mV. The direct comparison with the 4TS$_{cc}$ results of the uncoated current collector (black solid line) clearly shows the effect of the precious metal coating. Due to the contact resistance of the distinct passivation layers formed on the uncoated Ti grade 5 surfaces, 260 mV additional overvolt-

age is required at 2 A/cm^2. The literature data shown in Figure 3.18 were recorded under comparable conditions (1 M KOH and 60 °C). Instead of the PiperION® AEM tested here, Aemion+^{TM} and Sustainion® AEMs were investigated in the presented reference data. It can be observed that the optimized current collectors enable competitive measurement results with the HT cell. The data show that the precious metal coatings have significantly reduced the passivation layer and thus minimized the contact resistance. This enables the application of the 4T sensing directly through the current collectors. Besides improving the performance of the developed flow cell, this also enhances the comparability between the parallel operated cells in the HT system.

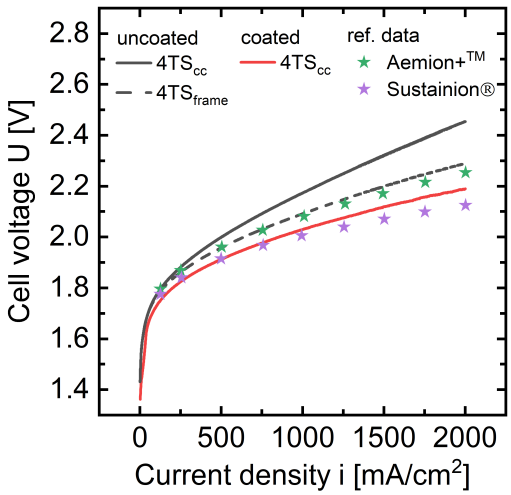

Figure 3.18: Precious metal-coated current collectors tested with zero-gap AEM WE using 4TS$_{cc}$. Measurements were conducted at 60 °C with PiperION® membrane, 1 M KOH, and a flow rate of 40 mL/min. Prior to each measurement, the cell was conditioned at 2000 mA/cm^2 for 1 h. Reference polarization curves were recorded under comparable conditions at 60 °C with 1 M KOH and Aemion+^{TM} or Sustainion® membrane[119].

3.3.2 Further potential modifications

In the following section, component modifications are presented and discussed that can be implemented in the future in order to further optimize the flow cell performance and comparability in the final HT system. First,

different current collector materials are analyzed as alternatives for the currently used Ti grade 5. Second, modifications of the cell housing are proposed to minimize the electrode distance in the finite-gap configuration. Finally, the implementation of additional electrical connections to the cell is discussed in order to improve the 4TS.

Alternative current collector materials

The current collectors currently used are made of Ti grade 5. The experimental development of the 4TS revealed a high electrical resistance of the Ti grade 5 in addition to the contact resistance at the surface. This observation is confirmed by literature resistance values of Ti grade 5 and other metals relevant for current collectors in electrochemistry, which are shown in Figure 3.19[121,125]. At 25 °C, Ti grade 5 has an electrical resistance of $178 \cdot 10^{-8}$ Ωm, which is significantly higher than the electrical resistance of alternative metals such as Pt, Ni or Au with 10.7, 7.1 and $2.3 \cdot 10^{-8}$ Ωm, respectively. Pure Ti (39 Ωm, 0 °C) or Ti grade 1 (47 Ωm, 20 °C) also show lower electrical resistivities compared to Ti grade 5.

The application of a current collector material with lower electrical resistance would further improve the cell efficiency for future applica-

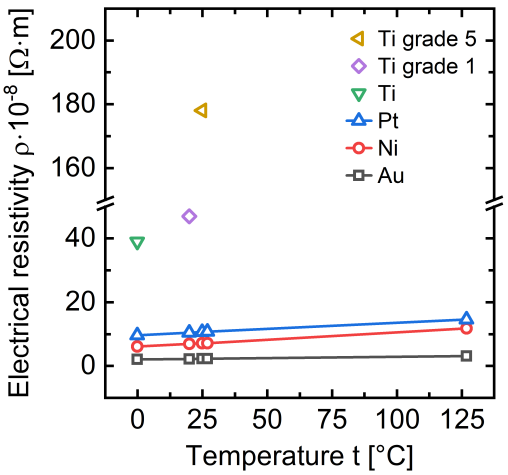

Figure 3.19: Overview of literature data on electrical resistivity of metals relevant for current collectors in electrochemistry[121,125].

tions. In the long term, the implementation of process-specific current collector materials is favorable. Ni is particularly suitable for all alkaline water electrolysis applications (AWE and AEM WE). Compared to Ti grade 5, the electrical resistance of Ni is 96 % lower. Furthermore, no surface coating would be required, as the oxide layers formed on Ni are much thinner and therefore the contact resistance of Ni surfaces not critical[126]. However, Ni is not suitable for CO_2 electrolysis applications. Fabricating additional current collectors from Au and Pt is not economical. For a set of CO_2 electrolysis-specific current collectors, the use of pure Ti or Ti grade 1 would be preferable to Ti grade 5. Both materials would also require a surface coating to avoid high contact resistance. However, the performance of the cell would be further improved due to their lower electrical resistivity.

Finite-gap electrode distance

The experimental validation of AWE in finite-gap configuration (cf. Section 3.2.1) revealed a notably high cell resistance, which caused very high cell voltages during the experiments. It was hypothesized that the cell resistance is primarily caused by the large distance between the electrodes. As the electrode distance extends, the electrolyte resistance increases. In the original housing design of the HT cell, the distance between electrode and separator is 12 mm (Figure 3.20a). To improve the efficiency of the cell, the design should be modified and the electrode distance significantly reduced to e.g. 2 mm as shown in Figure 3.20b.

The increase in efficiency that can be achieved by reducing the electrode distance was theoretically calculated. For this purpose, the cell resistance in the linear ohmic loss range was derived from the polarization curve of the actual finite-gap AWE data (cf. Section 3.2.1). For an electrode area of 5 cm^2, the specific, distance-dependent electrolyte resistance of 6 M KOH is 0.351 Ω/cm[120]. The reduction in distance was converted into an ionic electrolyte resistance, and the previously derived cell resistance was reduced accordingly. Assuming a constant onset voltage, the

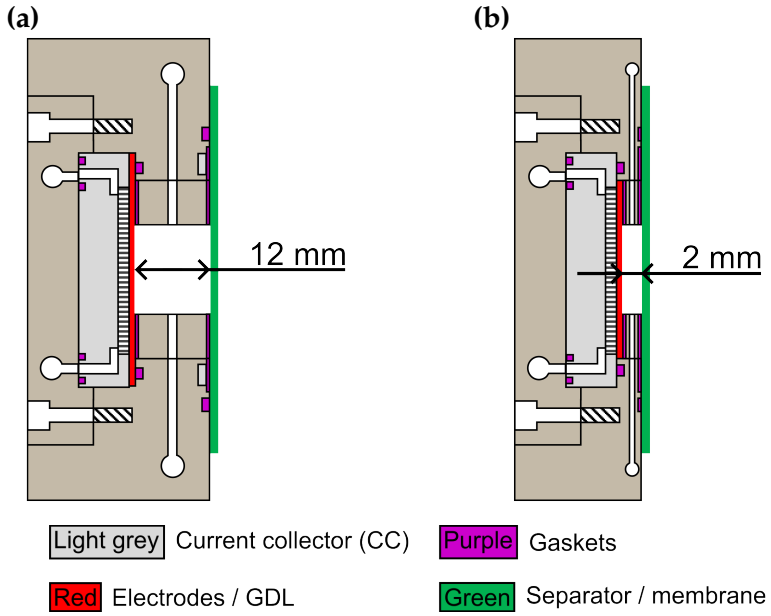

Figure 3.20: Schematic cross-sections of finite-gap design. (a) Original housing with 12 mm and (b) modified housing with 2 mm electrode-separator distance.

course of the polarization curve was plotted for the linear ohmic range for an electrode-separator distance of 5 and 2 mm. The comparison with the actual cell performance is shown in Figure 3.21. It can be observed that a reduction to 5 mm could already lead to a reduction of the cell voltage from 4.77 to 3.53 V at 500 mA/cm^2 . At a distance of 2 mm, the voltage would further drop to 3.00 V. Figure 3.21 additionally shows a reference AWE polarization curve of a commercial cell under similar conditions. The data was recorded with a Micro Flow Cell® from ElectroCell A/S at 25 °C in 6 M KOH[2].

The advantage of the extended electrode distance in finite-gap configuration is a homogeneous electric field throughout the electrolyte, which improves the quality of measurements in the 3-electrode setup. However, a large electrode distance negatively affects the cell efficiency. The data in Figure 3.21 demonstrate that the cell voltage can be significantly reduced by modifying the electrode distance. With an electrode-separator

distance of 2 mm, the HT cell achieves an efficiency level that is competitive with commercially available cells. Modifying the electrode distance requires the entire design of the HT flow cell to be redesigned, as this affects other components and is therefore associated with high costs. However, the current design holds risks for future research applications. The high ohmic losses are converted into heat. At high current densities, this can lead to high heat generation in the flow cell. This can be particularly problematic when researching new catalysts, e.g. in CO_2 electrolysis, as the activity and durability can be negatively affected. Reducing the electrode distance would thus also enhance the comparability of the finite-gap configuration and is therefore recommended despite the increased costs. It should be noted that the technical feasibility of the electrode distances analyzed here has not been verified for the HT cell design.

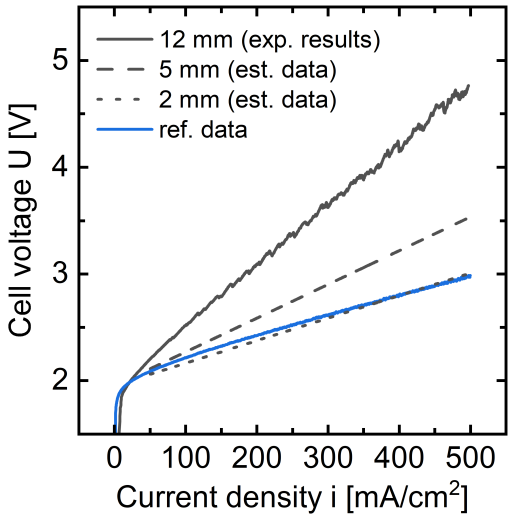

Figure 3.21: Effect of modified finite-gap design on cell performance. Cell voltages were estimated for an electrode-separator distance of 5 and 2 mm based on experimental results. Experimental measurement was conducted at 20 °C with 6 M KOH and a flow rate of 50 mL/min. Reference polarization curve was recorded at 25 °C with 6 M KOH[2].

Four-terminal sensing

During the validation phase, a four-terminal sensing (4TS) was developed to optimize the HT cell (cf. Section 3.2). First, the best results were achieved by measuring through the contact frame due to the high contact resistance of the passivation layer of the Ti grade 5 current collectors. Subsequent precious metal surface coatings have reduced the contact resistance improving the performance of the $4TS_{cc}$ via the current collector (cf. Section 3.3.1). To implement the $4TS_{cc}$, the cables of the reference and sense electrodes had to be connected to the heat exchanger fluid inlets. However, this arrangement is only an interim solution, as the heat exchanger function cannot be put into operation. For long-term application of the HT cell, it is recommended to modify the design of the current collector and provide an additional electrical connection for appropriate application of the $4TS_{cc}$. A modification of the current collectors also requires a modification of the cell housing and is therefore associated with increased effort. The modification of the electrical connections should therefore be implemented along with the reduction of the electrode distance (cf. Section 3.3.2).

3.4 Summary

For operation in the 16-fold HT system, a flow cell is required that provides reliable, reproducible results to ensure that the data generated is comparable between all experiments running in parallel. Furthermore, the flow cell must be operated variably in different cell configurations with various processes and support the application of all important electrochemical methods. For this purpose, a new electrochemical flow cell was developed in collaboration between hte GmbH (Heidelberg), Fraunhofer Institute for Microengineering and Microsystems (IMM, Mainz), and Institute of Energy Technologies – Fundamental Electrochemistry (IET-1, Jülich).

This chapter introduced the newly developed HT flow cell. First,

the modular design, all cell components and possible features were described. The cell prototype was then intensively tested in single-cell experiments to validate important processes and methods. The results of the experimental validation were presented and discussed. Based on the experimental data, optimization potentials of the HT flow cell were identified and possible modifications were derived.

A high resistance was detected in the current collectors, mainly caused by passivation layers formed on the Ti grade 5 current collector surfaces. This resistance impaired the efficiency of the developed flow cell and the comparability in parallel operation. The current collector contact resistance was effectively bypassed by developing a four-terminal sensing method through the electrical contact frame of the cell housing. Using the developed sensing method, the measured cell performance was significantly improved and competitive efficiencies were achieved.

Furthermore, additional modifications were tested and discussed. First, the inlays were modified to improve the noise in the voltage signal, however the integrated chamfer in the inlays resulted in a non-quantifiable increase in the relevant cell cross-section. Second, the current collectors were coated with precious metals, which significantly reduced the contact resistance and enabled four-terminal sensing directly through the current collector with very good cell efficiencies. Finally, the flow field design was modified to optimize the fluid distribution. Further suggestions for cell optimization were presented and discussed, which could further improve cell performance for future research applications.

Chapter 4

Stray current investigations

Parts of this chapter have been published in

Dogan, Deniz, et al. ”Experimental determination of stray currents in parallel operated cells exemplified on alkaline water electrolysis.” Electrochimica Acta (2024): https://doi.org/10.1016/j.electacta.2024.144767.

The author contributions are shown in the list of publications on page vii.

4.1 Motivation

The design of the electrolyte supply system for parallel operation in the HT system can either provide a common supply for all cells via a tube manifold or separate cycles for each cell individually. A common electrolyte supply has significant economic advantages due to savings in capital and operating costs[68], however, at the same time provides the systemic requirements that stray currents can flow between the parallel cells under particular operating conditions (cf. Section 1.3). With fully separated electrolyte cycles, stray current formation is prevented. This approach in turn limits synergies and increases the capital and operating costs of the HT system. Stray currents between parallel cells with a common electrolyte supply have hardly been studied so far. The aim of this study is the quantitative investigation of stray currents between parallel cells. The research results provide the basis for a data-driven, cautious consideration between the implementation of a common electrolyte supply or fully separated electrolyte cycles in the HT system.

First, stray currents between two parallel cells with a common electrolyte supply are experimentally investigated. Details of the experimental setup can be found in Figure 2.3. Subsequently, an ECM is developed with which stray currents can be simulated (cf. Figure 2.4). Based on the experimental results, the ECM is validated for two cells. Finally, the ECM is extended to 16 cells in order to quantitatively investigate the stray current formation in the HT system in case of a common electrolyte supply.

4.2 Experimental investigations of stray currents

Parallel operated electrolysis cells can measurably interfere with each other if they are operated with a common electrolyte supply. These interferences are shown in Figure 4.1, where the effect of an increasing cell voltage difference between the dynamic and the static cell $\Delta U = U_d - U_s$

on the cell current I_s of $cell_s$ was measured. $Cell_s$ was operated under steady state conditions at a constant low voltage with $U_s = 1.5\,V$ during the entire experiment. I_s was recorded as U_d was incrementally increased. Initially, both cells were operated at constant voltages of $U_d = U_s = 1.5\,V$ ($\Delta U = 0$) for 1 h. After the conditioning period, U_d is increased from 1.5 V in 0.1 V increments every 15 min until U_d reaches 2.5 V after 3.5 h. After one hour with the increase in ΔU, a sudden drop in I_s can be observed. This effect gradually diminishes with each further increase in the cell voltage difference. Furthermore, starting from $\Delta U = 0.3\,V$ the I_s signal becomes noisy. The noise intensity amplifies with an increase in cell voltage difference. At high values of ΔU, I_s approaches 0.13 mA as shown by the moving average (red line, Figure 4.1). After 3.5 h, the cell voltage difference is reset to 0 V and maintained for 15 min. Due to the sudden cell voltage difference reset, the current I_s in $cell_s$ rises abruptly and reaches 0.21 mA after 3.75 h. Furthermore, the noise stops immediately and the current signal continues undisturbed. The voltage dependent current of the dynamic cell I_d can be obtained approximately from Figure B.2 in the appendix.

In conventional single-cell operation, the electric field is formed within the cell between the anode and cathode. In the setup presented here (cf. Figure 2.3), the tube manifolds provide ionically conductive connections between the two cells operated in parallel. This arrangement leads to more complex electric field formations. The electric fields of the individual cells can expand through the tube manifolds and superpose each other. Furthermore, secondary electric fields can be formed between adjacent electrodes of the two parallel cells. The weak electric field of $cell_s$ operated at low cell currents is interfered by these complex electric field formations. As observed, even small differences in cell voltage of the adjacent dynamic $cell_d$ can therefore change the current in $cell_s$ and lead to noise in the current signal (Figure 4.1). As the cell current I_s increases, the influence of the electric field of the adjacent cell decreases. Measurement data at higher start cell voltages are shown in the appendix (Figure B.3 and B.4). As both interference effects disappear immediately when the

cell voltage difference is reset ($\Delta U = 0$), it can be excluded that the interferences are caused by other phenomena such as adsorption or foreign gas bubbles.

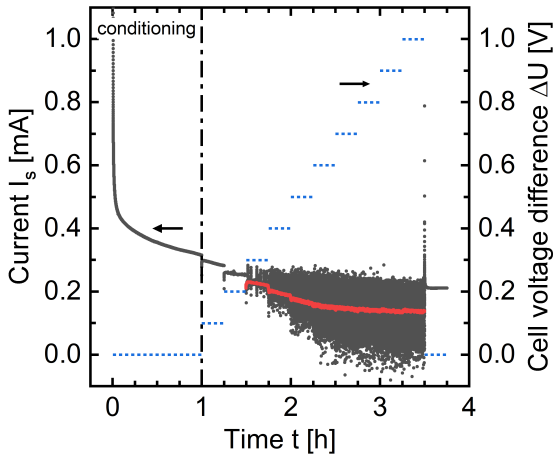

Figure 4.1: Effect of deliberately increased cell voltage difference $\Delta U = U_d - U_s$ on cell current I_s. I_s (left axis) at a constant cell voltage $U_s = 1.5\,V$ at all times with moving average (red line) and ΔU (right axis) are depicted as a function of time t. $Cell_d$ voltage U_d was increased by $\Delta U_d = \Delta U = 0.1\,V$ every 15 min starting from $U_d = U_s = 1.5\,V$ up to $U_d = 2.5\,V$. After 3.5 h ΔU was reset to 0 V.

Next, the potential differences between the electrodes of the parallel commercial cells were measured. In Figure 4.2, the voltmeter measurements between the reference electrodes located in the vicinity of the two anodes ΔE_{aa} and between the reference electrodes located in the vicinity of the two cathodes ΔE_{cc} (cf. Figure 2.3) are depicted as a function of the applied current density of the dynamic cell i_d. During the entire experiment, the steady state cell was operated at $100\,mA/cm^2$. ΔE_{aa} and $-\Delta E_{cc}$ show a linear course for $i_d \geq 50 mA/cm^2$ and a nonlinear course for $i_d < 50\,mA/cm^2$. In the linear region, the correlation $\Delta E_{aa} = -\Delta E_{cc}$ can be observed. For a current density value of $i_d = i_s = 100\,mA/cm^2$, the potential difference ΔE_{aa} and $-\Delta E_{cc}$ are both approximately zero. As i_d increases, ΔE_{aa} and $-\Delta E_{cc}$ increase linearly and reach a potential difference of about 280 mV at $500\,mA/cm^2$. In the non-linear region, both quantities show a divergent course. Deviating from the linear course, ΔE_{aa}

decreases more rapidly and shows a steep drop as i_d approaches 0 mA. Opposed to this, the curve of $-\Delta E_{cc}$ initially becomes flatter in the low current range as the current density decreases. For very small values of i_d, $-\Delta E_{cc}$ increases slightly.

As can be observed, ΔE_{aa} and $-\Delta E_{cc}$ are asymmetric at low current densities ($i_d < 50\,mA/cm^2$). This asymmetry in the measurement of potential differences is an indicator of an increased gas crossover. In water electrolysis, gas crossover describes the transport of hydrogen and oxygen in the cell through the separator to the opposite electrolyte compartment and is caused by different mechanisms. In the system of this study, the predominant mechanism for this effect is the differential pressure of the gases in the respective electrolytes.[127] Due to the mixing in the electrolyte reservoir and common electrolyte supply, the hydrogen differential pressure in the catholyte and therefore the hydrogen gas crossover through the separator into the anolyte is equal in both cells. The same applies to the oxygen crossover. Thus, at low current densities ($i_d < 50\,mA/cm^2$), the gas crossover rate in the dynamic cell is relatively high. Since the hydrogen is partially oxidized at the anode and the oxy-

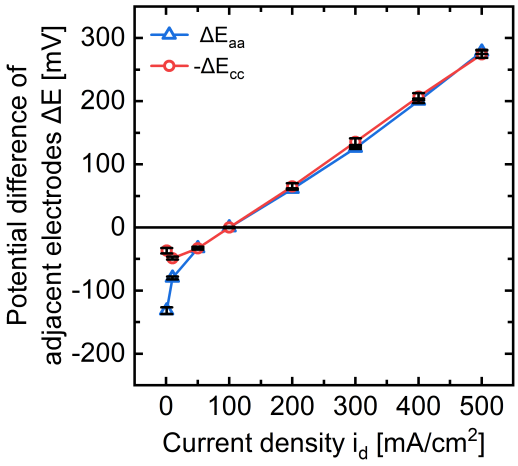

Figure 4.2: Potential difference of adjacent anodes ΔE_{aa} (blue line) and adjacent cathodes $-\Delta E_{cc}$ (red line). Current density i_d of $cell_d$ was stepwise increased from 1 up to 500 mA/cm^2. $Cell_s$ was constantly operated at $i_s = 100\,mA/cm^2$. Measurements were conducted at 25 °C.

gen is partially reduced at the cathode, this effect results in an additional charge transfer from the steady state cell to the dynamic cell. At very low current densities of the dynamic cell, this charge transfer affects the measured potential differences ΔE_{aa} and ΔE_{cc} and causes the asymmetric curve. Detailed explanations of this hypothesis with corresponding calculations are provided in the appendix B.

The distance-dependent electrochemical potential E(x) within the cells is schematically depicted in Figure 4.3. The potential profile is divided into five regions (I - V). The overpotentials characteristic for these regions are shown for the steady state cell (solid line) and dynamic cell (dotted line). The depicted curves are based on the data for the operating conditions $i_s = 100\,mA/cm^2$ and $i_d = 10\,mA/cm^2$ (a) as well as $i_s = 100\,mA/cm^2$ and $i_d = 500\,mA/cm^2$ (b). The anode overpotential drops in the vicinity of the anode surface (I). The electrode overpotential is composed of the activation and concentration overpotential. Both overpotentials are merged and shown as one curve in Figure 4.3. However, under the selected operating conditions, the activation overpotential predominates, as the process is not mass transport limited (Figure B.2a). The overpotentials over the anolyte (II) and the separator (III) are characterized by ohmic drops. The same overpotentials of the anode side occur on the cathode side (IV, V). Due to the symmetrical cell structure, the potential profile is almost rotation-symmetrical. Only the electrode overpotentials deviate from each other (Figure B.2b). The dimensions of distance x of the individual regions I - V in Figure 4.3 are not true to scale for improved visualization.

With increasing current density, the individual overpotentials I - V increase. Therefore, the potential profiles of the steady state and the dynamic cell differ in Figure 4.3. The potential difference between the potential in the steady state cell $E_s(x)$ and the potential in the dynamic cell $E_d(x)$ increases towards the respective electrodes. It can be seen that the contribution of the ohmic overpotentials to this effect is greater than that of the electrode overpotentials. It should be noted that this assumption is only valid for the operating conditions shown (no mass transport limi-

tation). The measurement of the potential differences ΔE_{aa} and ΔE_{cc} was conducted between two reference electrodes in the vicinity of the respective electrodes. The measured values ΔE_{aa} (red line) and ΔE_{cc} (blue line) are highlighted in color. Since measurements were not conducted between reference electrode and cathode or anode, but between both reference electrodes, changes of the difference of the electrode overpotentials are not taken into account. However, the effect of the changes caused by the electrode overpotentials on the measurement is negligible as discussed.

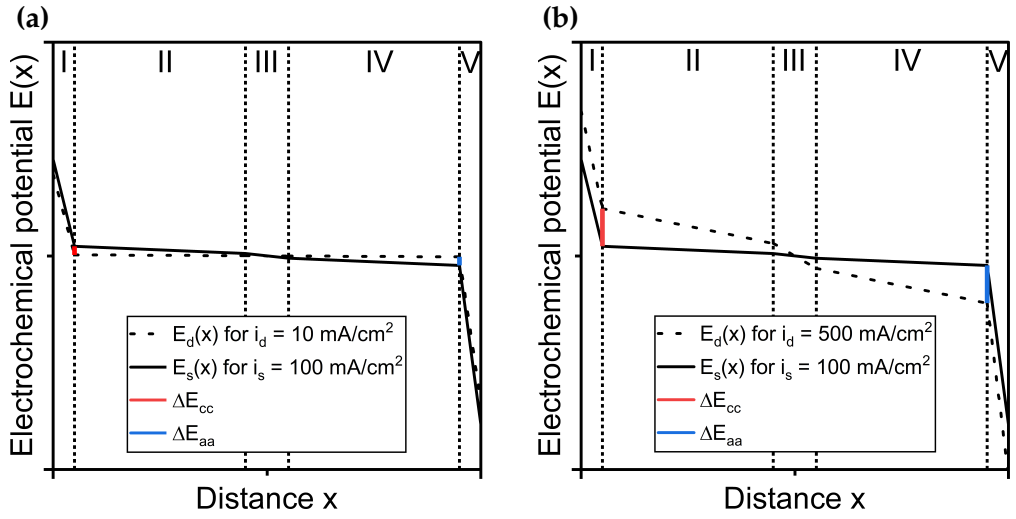

Figure 4.3: Schematic representation of the distance-dependent electrochemical potential E(x) for different operating conditions showing measured potential differences between adjacent cathodes (red solid line) and adjacent anodes (blue solid line). The potential distributions are shown for the steady state cell $E_s(x)$ (black solid line: (a) & (b) $i_s = 100\,mA/cm^2$) and dynamic cell $E_d(x)$ (black dashed line: (a) $i_d = 10\,mA/cm^2$ and (b) $i_d = 500\,mA/cm^2$). The potential distribution is composed of the electrode overpotentials I - V.

Figure 4.4 shows the results of the investigation of the temperature effect on the measured potential differences. Depicted are the anode and cathode potential differences ΔE_{aa} (a) and ΔE_{cc} (b) as a function of current density i_d at 25, 40 and 60 °C. Both the potential difference of the anodes and of the cathodes show a similar temperature behavior. The

experimental results indicate that an increase in temperature leads to a decrease in the absolute potential difference $|\Delta E|$. At $i_d = 500\,mA/cm^2$, ΔE_{aa} and ΔE_{cc} reach a potential difference of about 280, 220 and 170 mV at 25, 40 and 60 °C, respectively.

With increasing temperature, the ionic mobility increases resulting in lower ionic resistance of the electrolyte, i.e. the ionic cell resistance gradient dE/di decreases. As a result, the measured potential differences ΔE_{aa} and $-\Delta E_{cc}$ between both cells decrease with increasing temperature. The decrease of ΔE_{aa} and $-\Delta E_{cc}$ at constant current density is approximately proportional to the temperature increase. Apart from the ionic resistance of the electrolyte within the cells, the activation overpotentials are also affected by the temperature change.[128–130] However, these effects are negligible and were not measured with the herein applied approach.

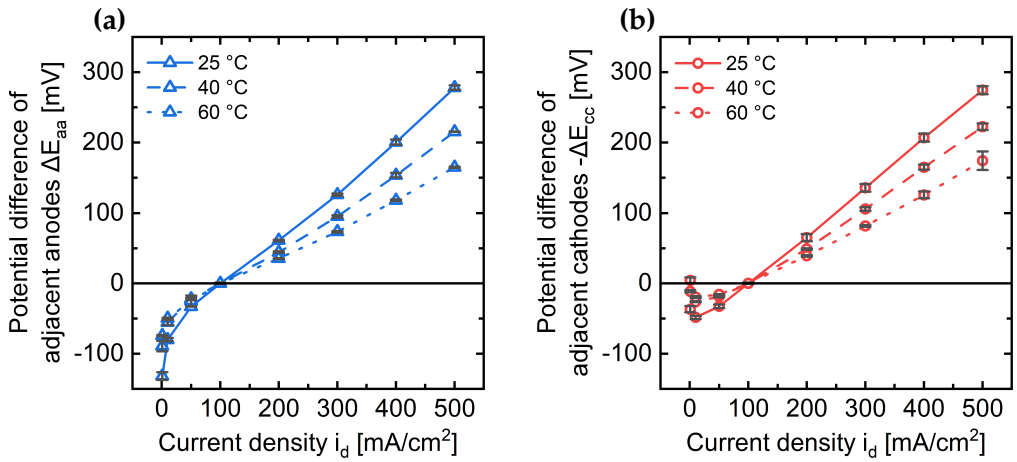

Figure 4.4: Potential difference of (a) adjacent anodes ΔE_{aa} and (b) adjacent cathodes ΔE_{cc} at elevated operating temperatures. Current density i_d of $cell_d$ was stepwise increased from 1 up to $500\,mA/cm^2$. $Cell_s$ was constantly operated at $i_s = 100\,mA/cm^2$. Measurements were conducted at 25, 40, and 60 °C.

In order to calculate the stray current I_{sc} using the measured potential differences, the ionic resistance of the electrolyte within the tube manifold R_t is required. For this purpose, tube extensions with a defined length $l_{t,ext}$ of 10, 20 and 30 cm were installed between the electrolyte inlets and out-

lets of the cells (cf. Figure B.5) and the ionic resistance was determined with EIS. The experimental data (squares) for one of the four identical tube manifolds are depicted in Figure 4.5a and show the expected linear dependence between the tube extension length and its ionic resistance. Reference data on KOH conductivity[120] was used to calculate the theoretical value of the length-dependent ionic resistance $dR_t/dl_{t,ext}$ for the given dimensions of the tube extension (12.7 Ω/cm at 25 °C). The calculated length-dependent ionic resistance was used to implement a linear fit on the experimental data (solid line). The experimental data are in very good agreement with the reference data. As the total cell-to-cell resistance was measured but plotted against the tube extension length, the data do not pass through the origin. The intersection with the ordinate at 277 Ω corresponds to the resistance of the tube connectors. The vertical dash-dotted line shows the experimental condition for the potential difference

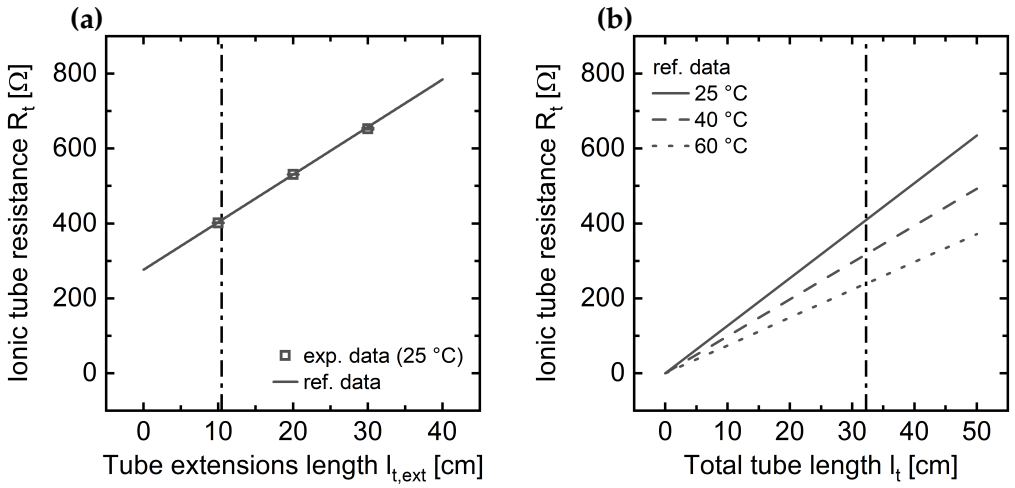

Figure 4.5: Ionic tube resistance R_t as a function of (a) tube extension length $l_{t,ext}$ and (b) total tube length l_t at elevated operating temperatures. Ionic tube resistance R_t was experimentally determined for $l_{t,ext}$ values of 10, 20 and 30 cm (a, squares) at 25 °C. Theoretical values of R_t at 25, 40 and 60 °C (b) were calculated based on specific conductivity values ρ of 6 M KOH taken from literature[120]. During the experiment, $R_t = 410\,\Omega$ was measured with the experimental setup (cf. Figure 2.3) of this study (dashed-dotted line).

measurements of this study. Given the very good agreement with the literature, R_t at elevated temperatures was subsequently calculated using the reference data[120]. Figure 4.5b shows the ionic tube resistance as a function of total tube length l_t for 25, 40 and 60 °C. The length-dependent ionic tube resistance is 9.9 and 7.4 Ω/cm at 40 and 60 °C, respectively. The total ionic resistance in the experimental setup for one of the four identical tube manifolds corresponds to a total tube length of 32.25 cm (dashed-dotted line).

Stray currents were determined based on the potential difference measurement results and ionic tube resistance data (cf. Figure 4.4 and 4.5). The total stray current I_{sc} is calculated by summing the respective partial stray currents of the common inlet and outlet manifolds of both the anode and cathode side. The results are depicted in Figure 4.6, showing the total stray current as a function of current density at 25, 40 and 60 °C. When both cells are operated at the same current density ($i_d = i_s = 100\,mA/cm^2$), the potential difference between the anodes and cathodes is zero and no stray currents are flowing. With increasing current density in $cell_d$, the stray current increases linearly and reaches 2.75 mA at $500\,mA/cm^2$. For current densities lower than $100\,mA/cm^2$, I_{sc} decreases linearly to negative values. It can be observed that a change in the process temperature has no major effect on the total stray current in the system.

The stray current curve is determined by the potential difference that was measured between the anodes and cathodes. In the low current range, the non-linearity of ΔE_{aa} and ΔE_{cc} compensate each other due to their opposite trends and lead to a linear progression of the total stray current in that region. Both the electrode potential difference ΔE (Figure 4.4) and the ionic tube resistance R_t (Figure 4.5) decrease with increasing process temperature due to the increasing conductivity of the electrolyte. The temperature effect on both parameters neutralize each other. The temperature has therefore no relevant influence on the stray current in the system.

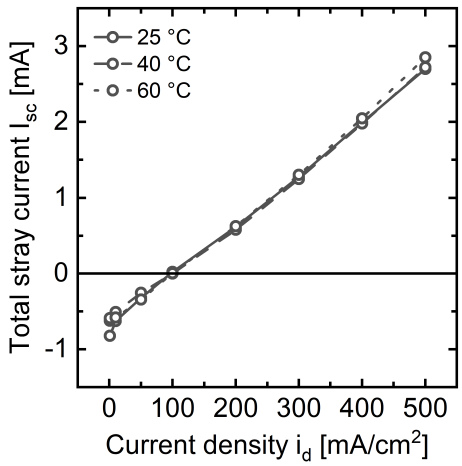

Figure 4.6: Total stray current I_{sc} between two commercial cells operated with AWE. Current density i_d of $cell_d$ was stepwise increased from 1 up to 500 mA/cm^2. $Cell_s$ was constantly operated at $i_s = 100$ mA/cm^2. I_{sc} was determined based on ΔE measurements and R_t data at 25, 40, and 60 °C.

Since the stray current is inversely proportional to the ionic tube resistance, I_{sc} is affected both by the conductivity of the electrolyte and by the tube geometry. Figure 4.7 shows the influence of the tube length l_t and the inner tube diameter d_i on the stray current. The presented stray current data are valid for the oparting conditions $i_s = 100$ mA/cm^2 and $i_d = 500$ mA/cm^2. The results indicate that the limit of $I_{sc}(l_t, d_i)$ is infinity as the tube length approaches zero or the inner tube diameter approaches infinity. The limit of $I_{sc}(l_t, d_i)$ is zero as the tube length approaches infinity or the inner tube diameter approaches zero. The manifold tubings of the setup for the potential difference measurements had a total tube length of 32.25 cm and an inner tube diameter of 4 mm. The corresponding experimental conditions are marked in Figure 4.7 (red triangle).

Decreasing the total tube length to zero or increasing the inner tube diameter to infinity will result in infinitely large stray currents, since these conditions correspond to a short circuit of the cells. Full isolation ($I_{sc} = 0$) is achieved by infinitely long tubing or an inner diameter of zero. The results show that both an increase in tube length and a decrease in tube diameter are appropriate measures to reduce the stray current present in

the system.

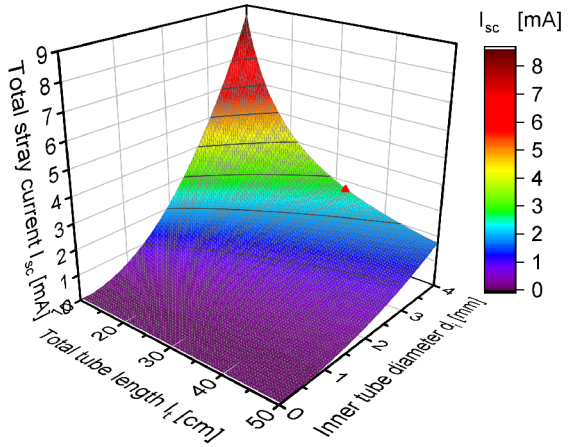

Figure 4.7: Effect of total tube length and inner tube diameter on total stray current between two AWE cells for $i_d = 100\,mA/cm^2$ and $i_s = 500\,mA/cm^2$. Conditions of experimental setup are marked at $l_t = 32.25\,cm$ and $d_i = 4\,mm$ (red triangle).

4.3 Equivalent circuit stray current modeling

To estimate the stray currents in the HT system, an ECM has been developed for parallel flow cells with a common electrolyte supply. Details of the ECM are given in Section 2.3.2. First, the ECM with two flow cells was fed and validated using the experimental results from Section 4.2. Subsequently, the ECM was stepwise extended to 16 cells and the effect of the number of cells N, the tube resistance R_t and the ratio of the manifold resistance R_m to the tube resistance R_t was investigated.

4.3.1 Model validation

To validate the ECM results, the output of the 2-cell model (cf. Figure 2.4b) was compared with the previously published experimental results. For this purpose, the model was fed with experimental input data. The relevant ionic resistances of the cell and tube connections were ob-

tained in the course of the previously described study performing electrochemical impedance spectroscopy ($R_c = 0.144\,\Omega$, $R_t = 410\,\Omega$). As operated in the experiment, $cell_s$ was modeled in steady state with a current density $i_s = 100\,mA/cm^2$. The current density of the dynamic cell i_d was increased stepwise up to $500\,mA/cm^2$. Both the model results (red line) and experimental data (black squares) are depicted in Figure 4.8. The experimental results revealed a linear correlation of the stray current I_{sc} with the current density i_d, as the potential difference between parallel electrolysis cells is mainly affected by the current-dependent ohmic voltage drops of the cells (cf. Figure 4.6). The model results fit the experimental data well, with a deviation of 4.1 % at $500\,mA/cm^2$, confirming the validation of the model.

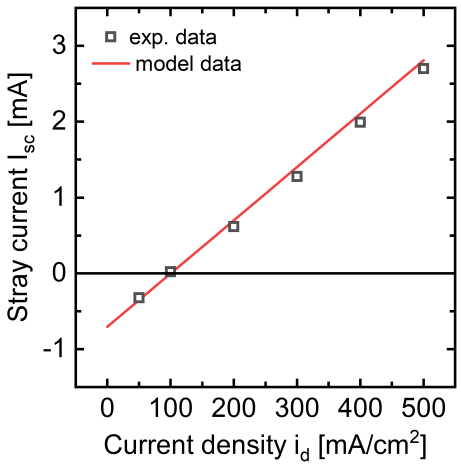

Figure 4.8: Validation of equivalent circuit model of two parallel cells. Comparison of estimated stray current (red line) with experimentally determined stray currents (black squares) between two commercial cells (Micro Flow Cell® from ElectroCell A/S) operated with AWE.

4.3.2 Model extension

The ECM was stepwise extended up to a total cell number N = 16 in order to investigate the effect of the cell number on the stray current formation. For this purpose, two quantities were analyzed. First, the cell stray cur-

rent $I_{sc,k}$, which equals the sum of all partial cell stray currents of the total four tube connections (inlet and outlet of both half cells) for each individual cell. The control variable k specifies the position index of the cell within the system and takes a value between 1 and N. Second, the total system stray current $I_{sc,system}$ was analyzed. The total system stray current is defined as the sum of the all cell stray currents in the system.

As N was increased, the current densities of the individual cells were systematically distributed. Two different current density distribution schemes were analyzed. First, the current density difference between directly adjacent cells was kept constant at $\Delta i = i_{k+1} - i_k = 100\,mA/cm^2$, whereby an increase in N increases the maximum current density i_N of the boundary cell N. In the second scheme, the current densities of the boundary cells were kept constant at $i_1 = 100\,mA/cm^2$ and $i_N = 1000\,mA/cm^2$, whereby an increase in N decreases the current density difference between directly adjacent cells Δi. The detailed current density distribution of both schemes for all values of N can be found in Table B.1 and B.2 in the appendix.

Figure 4.9a and 4.9b show the cell stray currents $I_{sc,k}$ of each cell for systems with different total cell numbers N of 4, 8, 12, and 16 cells with constant current density difference (Figure 4.9a) and constant boundary cell current densities (Figure 4.9b). Independent of the system size and the current density distribution, the cell stray currents $I_{sc,k}$ are highest in the boundary cells ($k = 1$ and $k = N$). $I_{sc,k}$ decreases toward the central cell positions and approaches zero. The current density i increases from cell to cell as the cell index k increases (cf. Table B.1 and B.2). For the central cells, the potential difference to the higher index cells is balanced by the potential difference to the lower index cells due to the symmetric arrangement of the system. This effect declines towards the boundary cells of the system.

An increase in system size has different effects on the cell stray currents $I_{sc,k}$ depending on the current density distribution scheme applied. The effect on the cell stray currents is greatest for the boundary cells ($k = 1$ and $k = N$). Figure 4.9c shows the boundary cell stray currents $I_{sc,1} = |I_{sc,N}|$

as a function of the total cell number N for a constant current density difference (open black squares) and constant boundary cell current densities (open red circles). For constant $\Delta i = 100\,mA/cm^2$, the boundary cell stray currents first increase with increasing N. For values $N > 5$, no significant further increase can be observed and $I_{sc,1} = |I_{sc,N}|$ approaches roughly

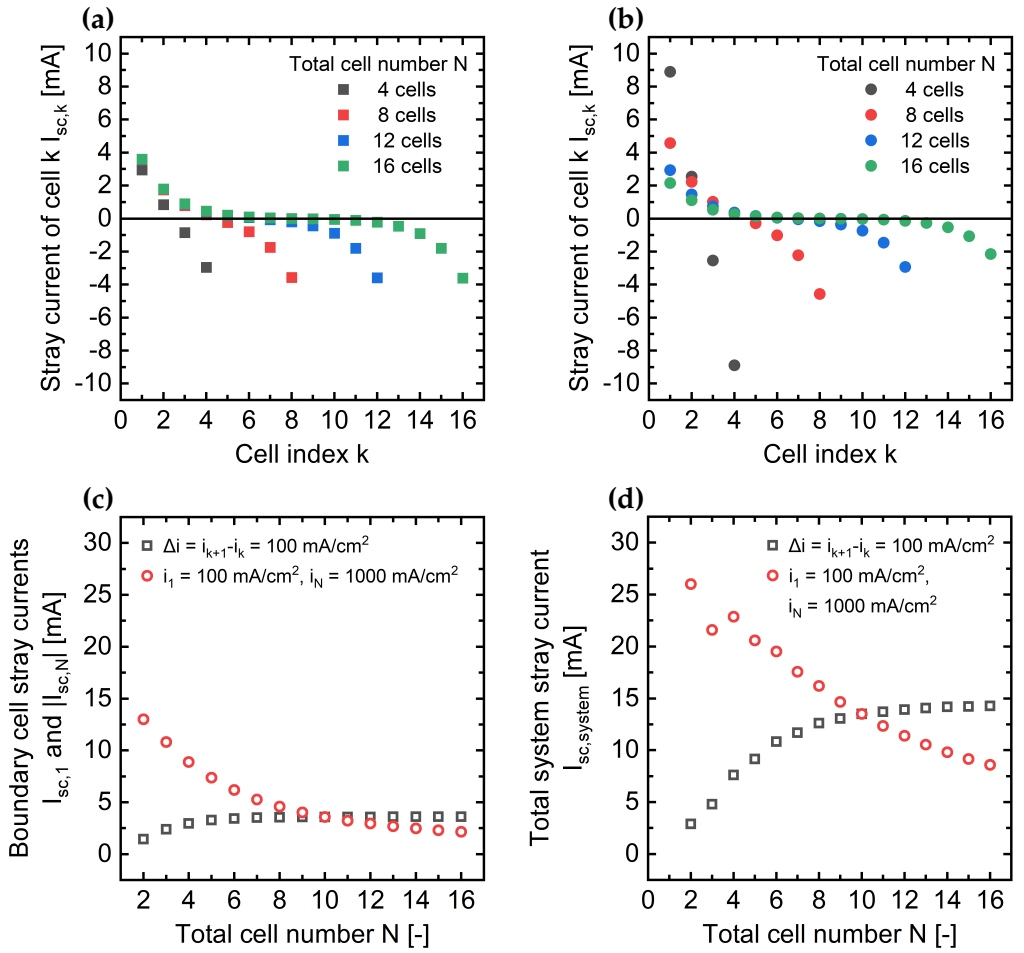

Figure 4.9: Effect of total cell number (a) on cell stray current $I_{sc,k}$ with constant current density difference $\Delta i = 100\,mA/cm^2$, (b) on cell stray current $I_{sc,k}$ with constant boundary cell current densities ($i_1 = 100\,mA/cm^2$, $i_N = 1000\,mA/cm^2$), (c) on boundary cell stray currents $I_{sc,1}$ and $|I_{sc,N}|$ as well as (d) on total system stray current $I_{sc,system}$. Stray currents were estimated with a tube resistance $R_t = 200\,\Omega$ and cell resistance $R_c = 0.144\,\Omega$.

3.6 mA. In contrast, for constant $i_1 = 100\,mA/cm^2$ and $i_N = 1000\,mA/cm^2$ the boundary cell stray currents decrease with increasing total cell number N and reaches about 2.2 mA at N = 16. As N continues to increase, $I_{sc,1} = |I_{sc,N}|$ would approach zero. At N = 10, both current density distribution schemes provide identical operating conditions (cf. Table B.1 and B.2).

The effect of N is most significant on the boundary cells, but can be observed to be attenuated at all other cell positions. The total system stray currents $I_{sc,system}$ for both current density distributions (Figure 4.9d), therefore, show a similar trend as the total number of cells increases. $I_{sc,system}$ initially increases at constant $\Delta i = 100\,mA/cm^2$ (open black squares) and approaches about 14.3 mA for increased values of N. At the same time, $I_{sc,system}$ decreases, if $i_1 = 100\,mA/cm^2$ and $i_N = 1000\,mA/cm^2$, and reaches about 8.6 mA for N = 16. $I_{sc,system}$ would approach zero for very high values of N. $I_{sc,system}$ is notably low for constant boundary cell current densities at N = 3. With this scheme the potential difference between the boundary cells remains constant, but the tube resistance $R_{t,N}$ increases with increasing N (cf. Equation 2.7). Thus, the system stray current decreases when enlarging to 3 cells. Due to symmetry effects, no stray current flows through the central cell if N = 3. With an even total cell number, stray currents flow through all cells, causing an increase in $I_{sc,system}$ as N is further increased from 3 to 4 cells. This effect is most noticeable for large current density differences and the lowest odd total cell number (N = 3). The effect declines with increasing total cell number, but can also be observed attenuated for higher odd values of N.

The results in Figure 4.9 show that the total cell number effects the individual cell stray currents and the total system stray current. An increase in N can have both a positive or negative effect, depending on the previously defined current density distribution. The influence of the total number of cells can therefore not be considered on its own, but must be evaluated together with the applied current densities in the system. Due to the inhomogeneous distribution of the stray cell currents, the boundary cells are affected most severely. This must be taken into account,

particularly with regard to possible stray current implications such as corrosion, faradaic and energy efficiency losses.[69,131]

4.3.3 Stray current reduction in 16-cell model

For a 16-cell system with a common electrolyte feed, there are various options how to design the tube connections. To characterize the tube design, the tube design factor f_d was introduced (cf. Equation 2.8), which describes the ratio of the manifold resistance R_m to the tube resistance between directly adjacent cells R_t. The influence of the tube design factor on the system stray current (Figure 4.10) was analyzed for the current density differences Δi of 20 (blue triangle), 60 (red circle) and 100 mA/cm^2 (black square). The analyses were carried out for a total number of $N = 16$ cells. For the boundary case $f_d = 0$, maximum system stray currents $I_{sc,system}$ of about 37, 111, and 184 mA are observed for 20, 60, and 100 mA/cm^2, respectively. The influence is greatest for low values of f_d leading to a sharp decrease in the total system stray current. As f_d increases, the influence declines and the $I_{sc,systen}$-curves flatten. When $f_d = 1$, the models show minimal stray currents of 2.9 (100 mA/cm^2), 1.7 (60 mA/cm^2) and 0.6 mA (20 mA/cm^2). Furthermore, the data show that a change in current density difference Δi has a proportional effect on the change in system stray current $I_{sc,system}$.

The stray current estimates in Figure 4.10 indicate that the tube design is critical to the magnitude of the total stray current in the system. The manifold resistance R_m between two cells stacks up as the distance between the cells increases (cf. Equation 2.7), protecting the system from very large potential differences between non-adjacent cells. If there is no manifold, all tube channels converge at one point and the tube resistance between all cells is equal ($R_{t,1} = R_{t,2} = .. = R_{t,16}$). In this case, the high potential differences between non-adjacent cells will cause very large stray currents. A discussion of the technical feasibility of a tube design without a manifold ($f_d = 0$) or without channels ($f_d = 1$) is omitted at this point. Figure 4.10 demonstrates that the electrolyte feed of parallel cells should

provide a manifold structure. To avoid very high stray currents, a tube design factor of at least $f_d = 0.2$ is recommended.

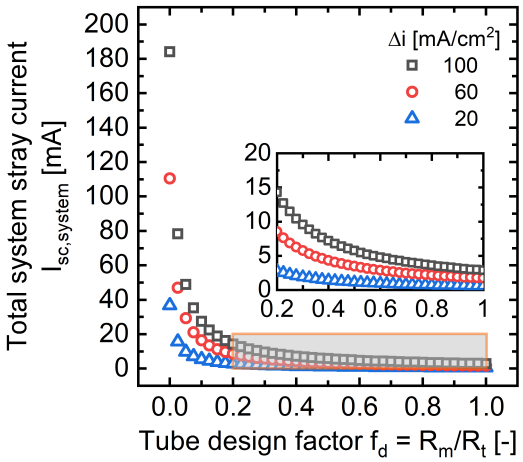

Figure 4.10: Effect of tube design factor on total system stray current. Stray currents were estimated for different current density differences Δi of 20, 60, and 100 mA/cm^2. Equivalent circuit model was built with a total cell number N of 16 cells, tube resistance R_t of 200 Ω, and cell resistance R_c of 0.144 Ω.

In addition to the current density difference Δi and tube design factor f_d, there are further parameters that affect the stray current in systems with parallel cells, such as the tube resistance. The influence on the total system stray current $I_{sc,system}$ was investigated as a function of the tube resistance R_t in the ECM with 16 cells and $\Delta i = 100$ mA/cm^2. Stray currents were estimated for different tube design factors f_d of 0.1, 0.3, and 0.5. Figure 4.11 shows that the total system stray current decreases with increasing tube resistance. R_t describes the tube resistance between directly adjacent cells and is therefore a simplified parameter to describe the complex resistance network in the 16-cell system. Although $I_{sc,system}$ indicates the total stray current of the entire system, $I_{sc,system}$ is inversely proportional to R_t. The inverse proportionality of R_t is maintained when the tube design factor is changed. Thus, an increase in R_t from 200 to 1000 Ω will decrease the system stray current by 80 % from 27.4 ($f_d = 0.1$), 9.6 ($f_d = 0.3$), and 5.6 mA ($f_d = 0.5$) to 5.5, 1.9, and 1.6 mA, respectively.

The total stray current in the 16-cell system could be reduced to less

than 2 mA by increasing the tube resistance Rt, even with high current density differences of 100 mA/cm^2. Increasing R_t is a simple and effective method to significantly reduce the stray currents in the system. Technically, this approach is commonly realized by extending the tube or reducing the tube diameter, which causes other effects such as an increase in pump resistance. Such impacts must be considered when designing the tubing for the common feed of parallel cells. The magnitude of the tube resistance cannot be considered individually, but can only be reasonably defined by taking further system parameters into account.

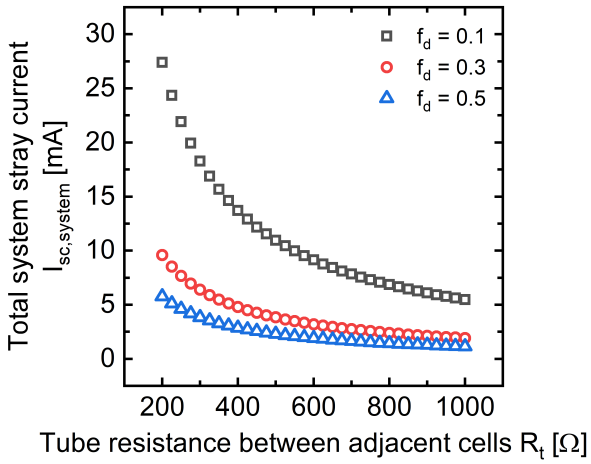

Figure 4.11: Effect of tube resistance on total system stray current for different tube design factors f_d of 0.1, 0.3, and 0.5. Equivalent circuit model was built with a total cell number N of 16 cells, current density difference Δi of 100 mA/cm^2, and cell resistance R_c of 0.144 Ω.

4.4 Summary and impact on system design

In this chapter, the stray current formation was quantitatively investigated for a HT system with 16 parallel, commonly supplied cells. For this purpose, stray currents were first determined experimentally between two flow cells. Based on the experimental results, a newly developed ECM for two parallel cells was fed and the simulation results were successfully validated with a deviation of 4.1 % at 500 mA/cm^2. The ECM

was stepwise extended to 16 cells. Under the operating conditions investigated, an inhomogeneous distribution of the individual cell stray currents was identified, with the highest stray current load on the first and last cell in the system. A total system stray current of up to 184 mA was estimated for the 16-cell system under the conditions selected here. However, if higher current density ranges are applied in the system, the total stray current increases further. It was shown that the number of flow cells N, the tube resistance R_t and the ratio of the manifold resistance R_m to the tube resistance R_t have a major influence on the total stray current. Furthermore, a holistic evaluation of the parameters is required to reduce the stray current. By optimizing these parameters, the estimated stray current in the HT system ECM was reduced to less than 2 mA.

The results of the quantitative studies of stray current formation in the HT system have revealed several drawbacks. Although the total stray current could be reduced to the mA level, this could only be achieved by increasing the total tube resistance. This is typically realized by increasing the tube length or reducing the tube cross section, and is therefore associated with a significant increase in the pumping power required. The results also indicate that the electrical fields of parallel cells influence each other through the ionically conductive connection, causing interferences. This can lead to severe signal noise and alteration of the average current/voltage signal, which is particularly critical when investigating low currents and voltages. Furthermore, a common electrolyte supply would have additional process implications. As the electrolyte of all cells would be continuously mixed with each other, time-resolved detection of liquid products would only be possible for the overall system, not for each individual cell. This is particularly critical when investigating processes with liquid main products, such as CO_2-to-formic acid.

Based on the quantitative study presented, a data-driven decision was made for the system design. With regard to the requirements for the HT system, the discussed disadvantages of a common electrolyte supply predominate. Despite the economic advantages of this design approach, all 32 electrolyte half-cell cycles in the HT system will be separated.

Chapter 5

Stainless steel contamination investigations

5.1 Motivation

Electrolyte contamination can severely impair electrolysis processes. The project partner hte GmbH has extensive experience in the construction of systems using stainless steel components. In contrast to other materials, stainless steel therefore offers economic advantages, particularly shorter design engineering and procurement periods. However, the use of stainless steel components in the electrolyte cycles could lead to contamination of the electrolyte with metal ions through chemical corrosion, which could have a negative impact on the electrolysis processes during operation of the HT system or accelerate the degradation of the system equipment. The purpose of the study presented in this chapter is to quantitatively investigate the contamination risk of different electrolyte solutions in contact with corrosion resistant stainless steels. The experimental results are the basis for a data-supported decision on the use of stainless steel or an alternative material in the electrolyte circuits.

5.2 Experimental investigations of contamination risk

Various electrolyte solutions were selected and continuously recirculated through an austenitic stainless steel pipe over a period of 7 d. For this purpose, AISI 316Ti (EN 1.4571) was selected, which is known for its good corrosion stability[95]. More details on the experimental setup and procedure can be found in Section 2.3.3. Liquid samples of the electrolyte solutions were collected at regular intervals and analyzed using ICP-OES with regard to metal ion concentration of Fe, Ni, Cr, Mo, and Ti. In the following, the results of the most important electrolyte solutions for the operation of the HT system are discussed, i.e. 6 M KOH (AWE and AEM WE)[11], 2 M $KHCO_3$ (CO_2 electrolysis)[132,133] and deionized H_2O (proton exchange membrane water electrolysis)[134]. Other solutions used in electrolysis such as H_2SO_4 (CO_2 electrolysis)[135], NaCl (chlor-alkali electrolysis)[136] and HCl (HCl electrolysis)[137] were additionally tested. The experimental results are shown in the Appendix (Figure C.1 - C.3). Lastly, the potential influence of metal ion contamination in the electrolyte solutions on the electrolysis processes in the HT system when using stainless steel is discussed and finally a data-based material decision is made for the HT system design.

Figure 5.1 shows the metal ion concentration as a function of time in 6 M KOH. Fe ions were already detected in the solution after very short time (Figure 5.1a). The concentration is $1.56 \cdot 10^{-5}$ mol/L after 5 min and increases further to over $2 \cdot 10^{-5}$ mol/L after 1 d. In the following days, the Fe ion concentration increases more slowly and reaches approximately $2.81 \cdot 10^{-5}$ mol/L after 7 d. In comparison, the Ti ion concentration only exceeds the detection limit of the ICP-OES ($1.25 \cdot 10^{-6}$ mol/L in 6 M KOH) after 1 d. The concentration then increases from $2.63 \cdot 10^{-6}$ after 1 d to $6.14 \cdot 10^{-6}$ mol/L after 7 d. Ni, Cr, or Mo ions were not measured in the liquid samples over the entire test period.

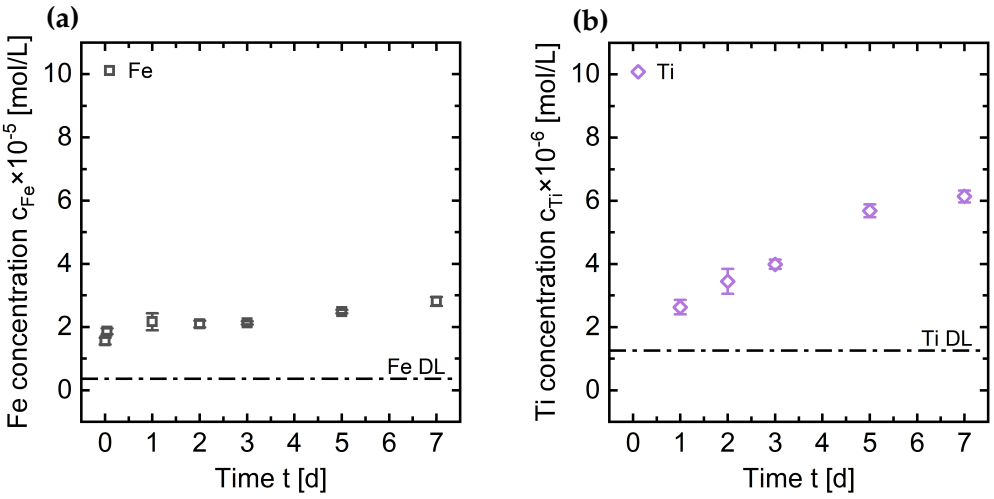

Figure 5.1: Metal ion contamination of (a) iron Fe and (b) titanium Ti in 6 M KOH due to contact with AISI 316Ti (EN 1.4571) stainless steel. Analyzes were conducted with ICP-OES. Fe and Ti detection limit in 6 M KOH is 0.36 and 1.25·10^{-6}mol/L, respectively. Nickel Ni, chromium Cr, and molybdenum Mo ions were not detected.

$KHCO_3$ is a commonly used electrolyte solution in CO_2 electrolysis. In Figure 5.2 the data of the corrosion test on AISI 316Ti with 2 M $KHCO_3$ are depicted. The detection limit of the ICP-OES for Fe ions under these conditions is 3.58·10^{-6} mol/L. After one day, the concentration exceeds the detection limit for the first time with 3.94·10^{-6} mol/L. In the following days, the Fe ion concentration stabilized at approximately 5.6·10^{-6} mol/L. None of the other metal ions Ni, Cr, Mo, or Ti that were analyzed were detected in the solution during the entire duration of the experiment.

Deionized H_2O plays a crucial role in PEM WE as the primary reactant, facilitating the oxidation of H_2O molecules at the anode. The operation of PEM WE is not directly targeted for the HT system, but could be of interest in the future. Moreover, deionized H_2O will be indispensable for rinsing the electrolyte cycles of the system after operation. Therefore, the contamination risk of deionized H_2O by AISI 316Ti was similarly tested (Figure 5.3). The detection limit of the ICP-OES for Fe in H_2O is 0.54·10^{-6} mol/L. It can be seen that a concentration of 0.61 was measured on day 3. After 7 d, approximately 1.07·10^{-6} mol/L Fe ions were

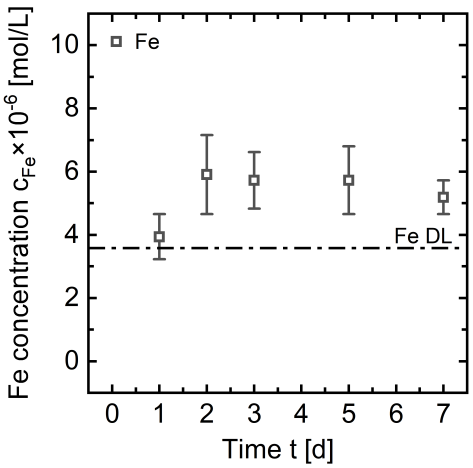

Figure 5.2: Metal ion contamination of iron Fe in 2 M $KHCO_3$ due to contact with AISI 316Ti (EN 1.4571) stainless steel. Analyzes were conducted with ICP-OES. Fe detection limit in 2 M $KHCO_3$ is $3.58{\cdot}10^{-6}$mol/L. Nickel Ni, chromium Cr, molybdenum Mo, and titanium Ti ions were not detected.

detected in the deionized H_2O. In the day 5 sample, no Fe ions were detected. This is probably attributed to the fact that the Fe ion concentration is close to the detection limit of the ICP-OES during this experiment, which in turn additionally exhibits a system-related error tolerance. No further analyzed ions could be detected in the deionized H_2O during the test period.

For further discussion of the risk of contamination in electrolysis operation when using AISI 316Ti in the electrolyte cycles of the HT system, the ion concentrations after 7 d of all analyzed metals for all tested solutions are shown collectively in Figure 5.4. In addition to the electrolytes and deionized H_2O already discussed (Figures 5.1 - 5.3), the results of the additionally tested solutions 2 M NaCl, 2 M H_2SO_4 and 6 M HCl are also presented. The temporal concentration profiles of these solutions can be found in the Appendix (cf. Figure C.1 - C.3). The results indicate that the two acids exhibit the highest corrosion activity with regard to all analyzed metal ions. All metal ions analyzed were detected in both acids. 6 M HCl has a higher corrosion activity and contained concentrations of up to almost 1 mol/L (Fe) after 7 d. It can be observed that Fe ions are

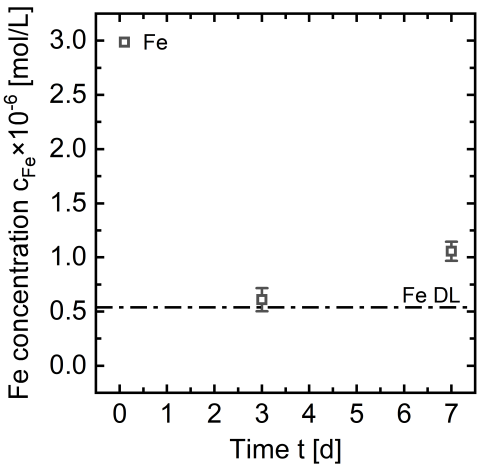

Figure 5.3: Metal ion contamination of iron Fe in deionized H_2O due to contact with AISI 316Ti (EN 1.4571) stainless steel. Analyzes were conducted with ICP-OES. Fe detection limit in deionized H_2O is $0.54 \cdot 10^{-6}$mol/L. Nickel Ni, chromium Cr, molybdenum Mo, and titanium Ti ions were not detected.

present in different concentrations in each solution tested. Among all electrolyte solutions, 2 M $KHCO_3$ shows the lowest Fe ion concentration with $5.2 \cdot 10^{-6}$ mol/L. Even in neutral deionized H_2O about $1.1 \cdot 10^{-6}$ mol/L Fe ions could be detected.

Water electrolysis processes are known to be sensitive to electrolyte impurities impacting cell performance, hydrogen purity and durability. Impurities therefore have a particularly negative effect on the economic efficiency of water electrolysis. However, the influence of explicit metal contamination has hardly been investigated quantitatively.[139] Contamination is most likely much more critical in CO_2 electrolysis due to the complex reaction mechanisms and the large number of possible end products[140,141]. In this context, the deactivation of the CO_2 catalytic property of Cu electrodes by Fe contamination in the electrolyte for CO_2 electrolysis was investigated[138]. The study revealed that even Fe ion concentrations as low as $1 \cdot 10^{-7}$ mol/L (red line in Figure 5.4) have a major negative impact on CO_2 electrolysis product formation. Due to the contamination with Fe, the product formation shifts dramatically towards the by-product H_2. It can be seen that each of the electrolyte solutions

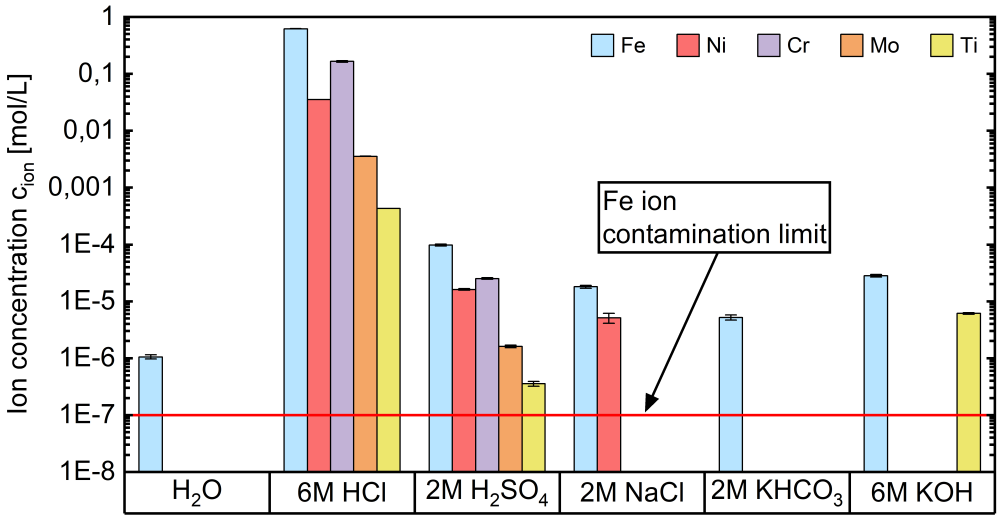

Figure 5.4: Overview of metal ion contamination after 7 d in various electrolyte solutions and deionized H_2O due to contact with AISI 316Ti (EN 1.4571) stainless steel. Analyzes were conducted with ICP-OES. Contamination limit of Fe ions for electrochemical CO_2 reduction (red line)[138].

and deionized H_2O tested has exceeded the limit value for Fe contamination after 7 d. Looking at the temporal concentration curves (Figures 5.1 - 5.3 and C.1 - C.3), it becomes clear that the Fe limit is exceeded by each electrolyte solution already after 1 d or even earlier, and in the case of deionized H_2O after 3 d .

5.3 Summary and impact on system design

In this chapter, the risk of contamination of various metal ions by different electrolytes in contact with austenitic steel AISI 316Ti was quantitatively investigated. The results show that the type and concentrations of metal ions detected over time differ greatly depending on the electrolyte solution. In all electrolyte solutions as well as in deionized H_2O, Fe ion contaminations were measured, which strongly exceeded the Fe contamination limit in previously published studies for CO_2 electrolysis[138]. In addition to alkaline water electrolysis processes, CO_2 electrolysis will be

an important research focus with the HT system. The use of stainless steel components such as AISI 316Ti in the electrolyte cycles of the system must therefore be avoided.

Based on the experimental study presented, a data-driven decision was made for the system design. Despite the economic advantages of stainless steel, all components in contact with the electrolyte in the system will be made of inert polymers wherever possible.

Chapter 6

High-throughput test system

Parts of this chapter have been published in

Dogan, Deniz, et al. "A Well-Advanced High-Throughput Test System for Electrocatalytic Screening Applications Under Industrial Relevant Conditions - A Perspective to Accelerate Electrolysis Research and Development." Electrochemical Science Advances (2024): https://doi.org/10.1002/elsa.202400015.

The author contributions are shown in the list of publications on page vii.

6.1 System design approach

The developed HT system is designed to accelerate testing under industry-relevant conditions and to provide a high system variability, data comparability as well as reproducibility. This also required the development of a new electrochemical HT flow cell (cf. Chapter 3). To meet all requirements, the system design is based on four key principles: parallelization, automation, modularization, and standardization. These key principles guided the development process of the entire system and are described in more detail in the following sections.

The HT approach is realized in the developed system through parallel screening. The parallel operation of up to 16 HT flow cells simultaneously will significantly reduce the screening time compared to conventional setups.

All important process and electrochemical parameters are controlled or measured fully automated. The high degree of automation allows systematically programmed test protocols to be executed without human interaction. This improves reproducibility and comparability, further minimizes screening time and creates ideal conditions for the implementation of advanced statistical design of experiment strategies.

The developed HT system has a modular design, which can be adapted to changing research requirements, enabling the screening of a wide range of applications and processes for maximum variability.

The use of standardized components for the system significantly improves the reproducibility and comparability of the generated data. Furthermore, standardization of documents and test protocols will also play an important role.

6.1.1 High-throughput test system

The developed HT system consists of different system module racks (Figure 6.1). Due to the modular design, the configuration of the system can be adapted to the individual research requirements.

The gas and analytic rack consists of gas modules for the supply of N_2 and CO_2 process gases as well as the gas chromatograph (GC). Furthermore, it provides corresponding GC gas supply infrastructure for the automated measurement of gaseous product samples supplied by the product selection and reactor support rack.

The liquid preparation and waste rack consists of pumps, two large electrolyte feed tanks for anode and cathode, respectively, as well as a large waste tank on the bottom of the rack. By an automated electrolyte management system, electrolyte with defined conductivities for both anode and cathode can be automatically prepared, refilled, distributed to individual feed tanks in the reactor racks and disposed in a waste tank at the end of its usage. This way the operator does not get in contact with the electrolyte throughout the operation of the HT system.

In the product selection and reactor support rack, the gaseous product streams of each electrochemical cell are selected in a multiport valve and sequentially sent to the GC for online analysis. The other streams are passed to the exhaust. This module also contains a humidification section for the gas feed.

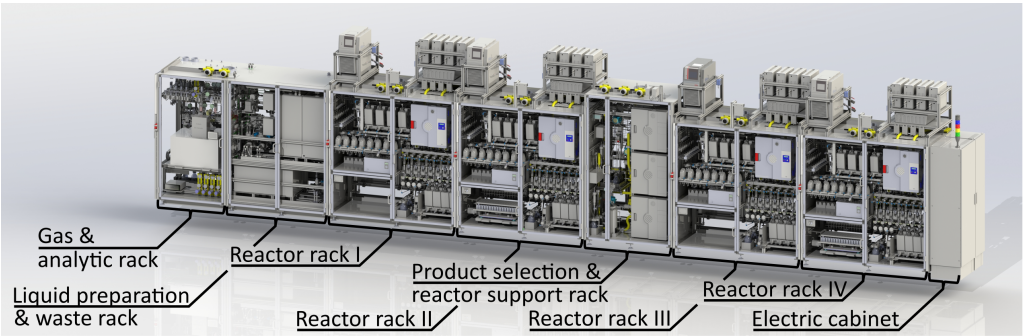

Figure 6.1: 3D layout of the 16-fold parallelized high-throughput test system for electrolysis processes.

The entire HT system comprises a total number of 16 of the developed HT flow cells. The flow cells are operated within the reactor racks I - IV, each containing four electrolyzers. The distribution over four individual reactor racks allows the parallel operation of only 4, 8, or 12 cells and

the setting of different process parameters in each reactor rack. A highly simplified flow sheet for a single cell is depicted in Figure 6.2. Each cell has an individual anolyte and catholyte feed tank. The feed tanks are automatically filled with the prepared electrolytes from the large storage tanks of the liquid preparation and waste rack. Two operating modes are available for the electrolyte flow. In single-pass mode, the electrolyte flows from the feed tank through the electrolyzer and phase separator directly to the waste tank. In recycle mode, the electrolyte returns to the feed tank after phase separation to recycle the electrolyte solutions. The electrolyte cycles of all 32 half cells are fully separated. Hereby, liquid products can be enriched in recycle mode, which facilitates the detection of liquid products close to the detection limit. Furthermore, the emergence of stray currents within the system is prevented (cf. Chapter 4).[2] The diaphragm pumps enable cell-specific flow rates in the range

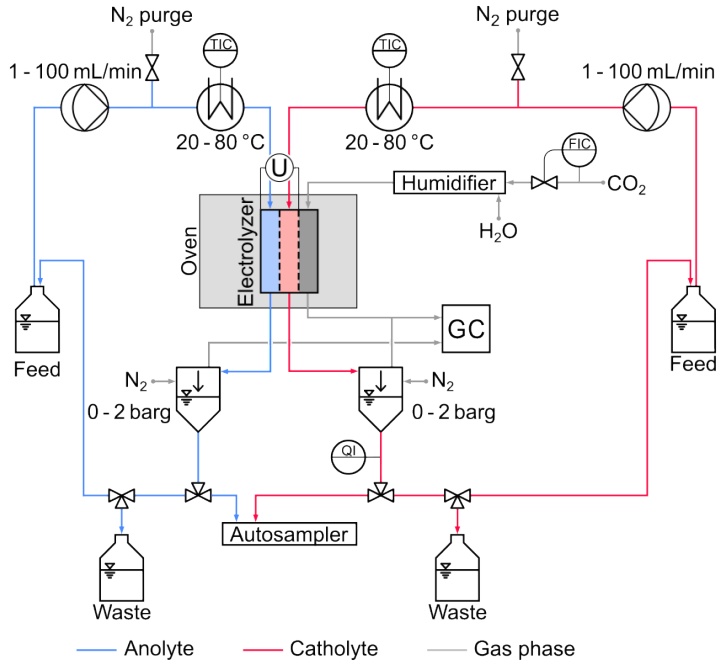

Figure 6.2: Simplified flow sheet of the HT system for one electrolyzer cycle. Abbreviations: temperature indicator controller (TIC), flow indicator controller (FIC), and quality indicator (QI). QI indicates the conductivity sensor. The depicted symbols are according to ISO 10628-1.

of 1 to 100 mL/min. Each electrolyte stream can be preheated in a heat exchanger up to 80 °C before it is pumped through the flow cell. For optimum temperature control, each reactor rack has a cell oven that heats the cell housing, all cell connectors and supply pipes to the pre-defined process temperature. Additionally, the cells can be connected to a thermostat, enabling active heating or cooling via the current collectors inside the cells. The process pressure in the HT system can be set in the range from 0 to 2 barg. The pressure is controlled individually for each half cell. For the use of gas diffusion electrodes, a gas feed can additionally be fed to the flow cell. This is particularly important when performing CO_2 electrolysis in the system where a CO_2 feed is required. Both the anolyte and catholyte product streams are equipped with individual phase separators downstream of the flow cell. An autosampler enables automated liquid sampling for offline liquid analyses after phase separation. The gaseous product phases are conveyed to the product selection rack for online GC analysis. The online GC enables one measurement every 8 min, resulting in a measurement interval of approximately 2 h/cell for the 16-fold system. The use of online GC analyses and ex-situ liquid analyses are indispensable for the planned system operation with CO_2 electrolysis processes[142].

Each reactor rack is equipped with a multi-channel potentiostat from Metrohm AG. Four channels of each multi-channel potentiostat are equipped with a bipotentiostat module and a 10 A Booster for high current experiments. For improved EIS scans two of 16 potentiostats are equipped with a FRA32M impedance module. Further modules can be retrofitted into the multi-channel potentiostats depending on the application requirements. The fully automated HT system is controlled by the hteControl4™ software from hte GmbH. A new interface to the NOVA© software package was developed for the system and implemented in hteControl4™. Together with the new interface, it is possible to create automated feedback loops and perform parameter adjustments for all process and electrochemical parameters in parallel operation mode.

The system must be designed to operate with chemically various elec-

trolytes, as it will be used to investigate different processes (AWE and CO_2 electrolysis)[11,142,143]. To prevent metal ion contamination due to chemical corrosion of steel components in the electrolyte circuit, all system components in contact with the electrolyte (pipes, valves, sensors, etc.) are therefore made of inert polymers (cf. Chapter 5).

6.1.2 4-cell system prototyping and validation

A prototype was built with a single reactor rack, providing four cells in parallel operation (cf. Section 6.1.1). The purpose of performing preliminary tests on the HT prototype was to test the technological practicability and basic functions. Thereby, issues or necessary optimizations to the system, cell or software could be identified and resolved at an early stage. In addition, the prototype was used to validate the reproducibility of the results generated with four cells operating in parallel. For this purpose, all cells were operated under nominally identical conditions, i.e. with AWE in zero-gap configuration using Ni meshes and Zirfon UTP 220 in 6 M KOH.

Figure 6.3 shows the results of the 4-fold reproducibility test. First, polarization curves up to 500 mA/cm^2 (scan rate 50 mA/s and step size 20 mA) were performed in all cells (Figure 6.3a). The current density range was selected based on state-of-the-art KPIs of AWE[24]. Since the shape and values of the measured polarization curve depend on the reaction kinetics, ohmic resistance, and mass transport losses, this method is well suited to derive first conclusions on the reproducibility[144]. The voltages of cell 2 and cell 3 show minimal deviation over the entire current density range and thus excellent reproducibility. The average cell voltage at 500 mA/cm^2 is 2.471 V with a standard deviation of 14.7 mV. Deviations from this value are -20.1, 1.9, -3.0 and 21.1 mV for cell 1, cell 2, cell 3, and cell 4 respectively. Figure 6.3a shows a higher onset potential in cell 4, which shifts the voltage curve marginally upwards. The polarization curve of cell 1, on the other hand, has a lower slope leading to slight deviations at high current densities. Figure 6.3b shows a

subsequent chronopotentiometry at 100 mA/cm^2 for 1 h. The data show a negligible deviation between cell 1, cell 2 and cell 3 at 100 mA/cm^2, however, a shift of about 25 mV for cell 4, confirming the observations described above.

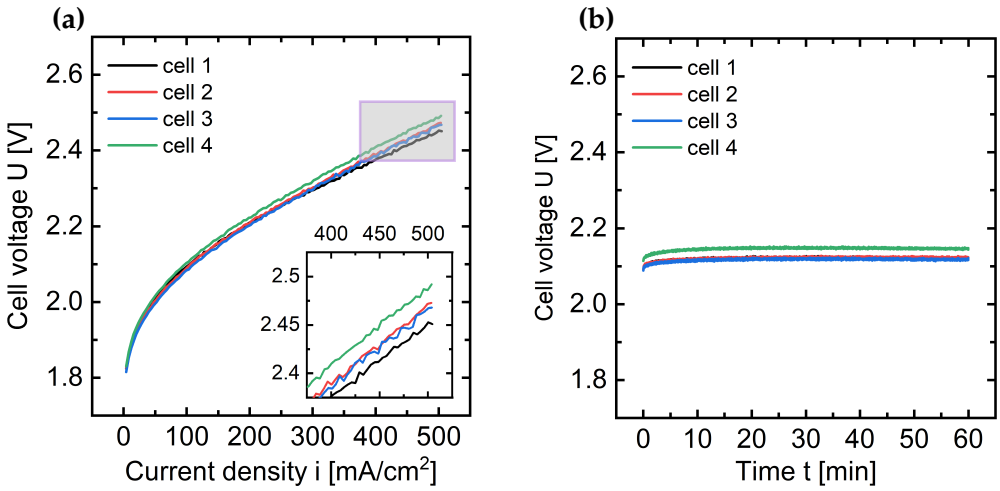

Figure 6.3: Reproducibility test with the 4-cell HT prototype under nominally identical conditions. All cells were operated with alkaline water electrolysis in zero-gap configuration using Ni meshes and Zirfon UTP 220 in 6 M KOH at 20 °C. (a) Polarization curves were recorded with a scan rate of 50 mA/s and a step size of 20 mA. (b) Chronopotentiometries were performed at 100 mA/cm^2 for one hour.

Ti grade 5 tends to form a characteristic passivation layer on the surface. Passivation layers increase the contact resistance for the electrons at the phase transitions and therefore required onset overvoltage.[116–118] This was already observed during the single cell validation phase (cf. Chapter 3.2. The deviating results for cell 1 and cell 4 are therefore potentially related to the passivation layers on the surface of the current collectors. Two approaches could address this issue. First, the current collectors can be manufactured from other materials (e.g. nickel alloy or stainless steel) that have a lower tendency to build a passivation layer on the surface. Second, the current collector surfaces can be coated with a thin layer of precious metal (e.g. Au on the cathode and Pt on the anode) or other materials with sufficient conductivity. A detailed discus-

sion of the two approaches to modifying the current collectors in order to optimize the efficiency and comparability of the HT cell can be found in Chapter 3.3.

The temperature control units of the 4-cell prototype were not under operation during the prototype experiments. Without active control, temperature fluctuations in the laboratory or external energy inputs (e.g. from pumps, neighboring cells, or waste heat of other devices) can cause temperature deviations between the individual electrolyte cycles. This might affect the results measured with the 4-cell prototype. With commissioning of the multifactorial temperature control (cf. Section 6.1.1), temperature fluctuation-related errors in the final HT system should be precluded.

All cells were operated under nominally identical conditions. However, other effects such as slight variations in electrode activity or differences in electrode spacing due to local overlap of electrode and gasket are still theoretically possible. Such material or experimental deviations would also influence the reproducibility of the results. The results presented highlight the challenge of ensuring high reproducibility under nominally identical conditions. The reproducibility of the data can be further improved with the measures discussed.

6.2 Design of experiments

The previous sections have discussed, how the four key principles, i.e. parallelization, automation, modularization, and standardization (cf. Section 6.1), were implemented in the HT environment. In order to exploit the full potential of HT experimentation, both experimental design and data analysis must be automated and streamlined to close the circle of a self-consistent, highly accelerated screening workflow (Figure 6.4). The full automation, process control, online analysis, and feedback loops of the HT setup (cf. Section 6.1.1) improve the availability, reproducibility, and cost-effectiveness of electrolyzer data considerably.

On the other hand, the parameter space of the degrees of freedom, which determine the performance of the electrolyzer, is high-dimensional, complex, and very often correlated. This parameter space comprises process parameters (temperature, pressure, electrolyte properties and flow rate), electrochemical parameters (current, voltage, electrode potential), and cell component parameters (electrodes, membranes, porous transport layers). Even with the introduced HT system, the feasible amount of generated data is still too small for a systematic screening of the parameter space and orders of magnitude below the required big data for machine learning approaches for data analysis and system modeling. However, this is where the adaptive, statistic design of experiments (DoE) approach holds a lot of potential.

DoE reduces experimental data with statistical methods, extracts the maximum amount of information from the data, and determines the optimal set of parameters for new experiments to be conducted. A DoE approach requires three things: First, a defined research goal, second, one or multiple descriptors, and third, a defined parameter space. Based on the research goal, two different areas of application for DoE are defined. The objective is either to optimize the experiment or to gain maximum information about the process throughout the parameter space corresponding to the exploration-exploitation dilemma in decision making with minimal experimental effort. The latter case strives to elucidate the mechanisms of the experiment and to describe them with mathematical models. In both cases one or multiple descriptors, which describe the performance of the experiment in a robust, concise way, are required to quantify either the optimality or characteristic features of the process.[145–147]

In the context of our electrochemical HT approach, iterative DoE strategies are the method of choice. Based on data collected from experiments in previous iterations of the DoE approach, DoE determines the most promising experiment (or set of experiments) to be conducted next in order to reach the research goal, such as optimizing important KPI's (cf. Figure 1.1), in the most efficient way. By exploiting previous knowledge and making an informed decision based on statistical probabilities,

adaptive DoE strategies surpass systematic, sequential as well as random sampling and scale orders of magnitude better with the dimensionality of the parameter space.[148–150] More recently, the coupling of DoE with large language models (LLMs), such as GPT-4, has been demonstrated. Simultaneously to active learning from the experiments conducted, the DoE is enabled to exploit the vast resources of both interdisciplinary and domain knowledge by LLMs. While additional care has to be taken with respect to the risks of hallucinations by LLMs and the limited comparability of previous literature knowledge with the current, innovative cell design, LLMs promise a significant step towards fully autonomous self-driving labs for electrochemical high-throughput screening.[151–153] The combination of DoE strategies with the developed HT system will amplify their individual potentials. Together they have the potential to accelerate the research and development process of new technologies while minimizing the required resources. DoE will be an indispensable tool of the HT system and guarantee its optimal use for maximum gain and output.

6.3 Research potential

6.3.1 Acceleration

One of the main objectives in developing the presented HT system is the acceleration of electrolysis research activities. In a conventional single-cell setup, the individual standardized workflow steps are carried out sequentially (Figure 6.4a). Due to the complexity of the parameter space in electrocatalysis, the workflow typically must be iterated several times, which is exceedingly time-consuming. Hereby, the operator laboriously works his way through the parameter space and slowly gains a deeper understanding of the material or process. The advantage of a parallelized HT system combined with a DoE approach over a one-dimensional sequential workflow is clear and becomes particularly attractive when a large number of parameter combinations need to be varied (cf. Section 6.2). By implementing DoE, a HT system can fully exploit its ac-

celeration potential compared to one-dimensional strategies. The DoE workflow for a parallelized n-fold HT system is shown in Figure 6.4b.

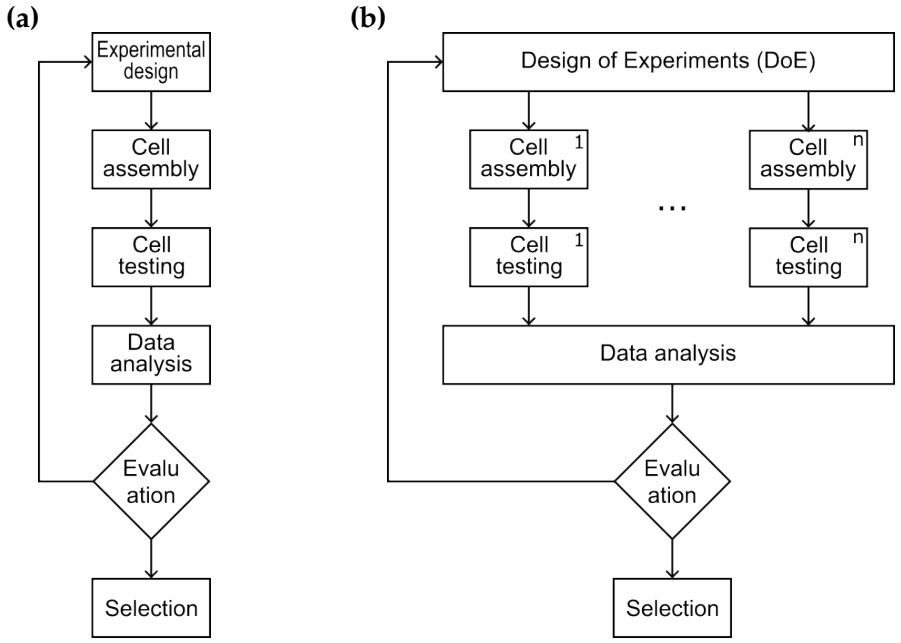

Figure 6.4: Workflow for (a) a one-dimensional sequential single-step experimentation approach and (b) a DoE workflow implemented in a HT system with n parallelized cells.

Figure 6.5 exemplifies the temporal comparison of two comparative studies that yield equal amount of experimental data. It shows the total time required to carry out the entire workflow once in a 16-fold HT system (Figure 6.4b) compared to 16 times in a single-cell setup (Figure 6.4a), based on a duration of 100 h per experiment. The estimated time required for the experiment design, cell assembly and data analysis is based on practical experience. For the estimated time frames, it was considered that experiment design, cell assembly and data analysis can only be carried out within working hours. The experiments (cell testing) can run 24 h/d without the presence of the operator. Experiment design takes the same time for both workflows, regardless of the system. During cell assembly and data evaluation, synergies can already lead to little time savings when using the HT system. The most significant time savings

are clearly achieved by carrying out the cell tests in parallel. The example calculation for a test period of 100 h results in a total time saving of approximately 86 %. The demonstrated comparison shows the great acceleration potential through considerable time savings when operating a 16-fold HT system. However, studies in a 16-fold system require careful experiment planning to make optimal use of the system's capacity and thus exploit its full acceleration potential (cf. Section 6.2).

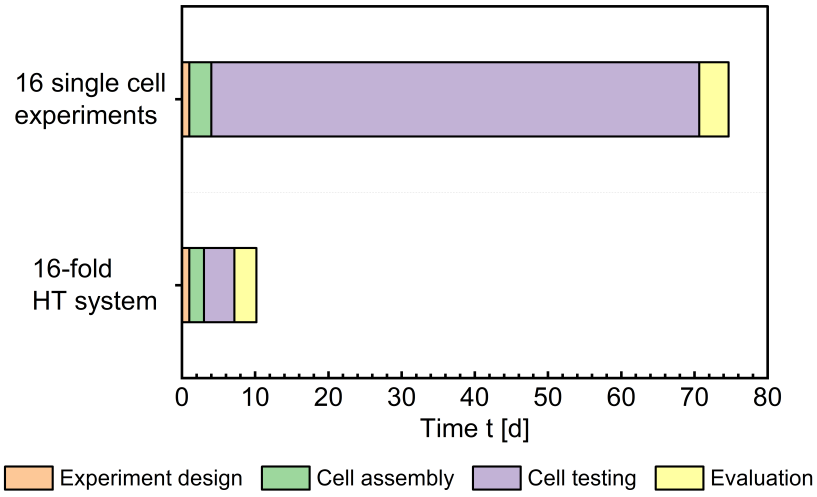

Figure 6.5: Comparison of workflow timeframes for 16 iterations of a 100 h experiment in a single cell setup vs. 16 cells running for 100 h in a 16-fold HT system. The calculation is based on a 8 h work day. Non-working days were not considered for the calculations.

6.3.2 Variability

High variability is one of the key characteristics of the introduced HT system, which distinguishes it from previous, mostly application-specific HT platforms. The system is intended to enable research into a wide range of research applications and the operation of various electrocatalytic processes.

Application variability

The most important applications are component screening as well as process and electrochemical parameter screening. In the case of component screening, different variants of a component are assembled into the flow cells. The modular design of the flow cell enables the assembly of all components commonly used in electrochemical research (cf. Chapter 3.1). Different variants of a component can be tested simultaneously under identical, precisely adjustable process and electrical parameters. The high level of comparability and reproducibility of the system ensures that nominally equal test parameters result in identical test conditions (cf. Section 6.1.2). Therefore, reliable and high-quality data can be generated, allowing any performance disparities observed during screening procedures to be directly attributed to the components themselves.

In contrast, parameter screening involves testing of identical components in all flow cells. Due to the high degree of automation and the sophisticated sensor and controller equipment of the HT system, most of the process and electrical variables of the complex parameter space can be controlled automatically. Therefore, the parameter space can be efficiently screened for the predefined set of components. The aim of parameter screening can be either the exploration of the parameter space or the discovery of optimum process parameters (cf. Section 6.2).

The HT system can be used in many other applications. Maintenance and replacement of degraded system components are very costly. To minimize these costs, system lifetime is one important KPI for industrial application (cf. Figure 1.1). Accelerated stress testing is a suitable method to efficiently and quickly induce aging of system components, thus enabling lifetime investigations, e.g. in the development of new materials at an early stage. The high degree of system automation provides ideal conditions for well-defined accelerated stress testing procedures.

Currently, electrolyzers can still be operated at a constant load due to the availability of fossil fuels. The constant availability of the energy carrier will end with the expansion and transition to renewable energies.

Future electrolysis systems must therefore be able to operate well under dynamic loads. The behavior under transient operation is another important KPI (cf. Figure 1.1) that must be considered during process development. Transient operation can be easily investigated with the developed HT system due to the sophisticated potentiostat setup.

Standard operation of the HT system involves the use of 16 single flow cells. The modular subdivision into four reactor racks allows the electrical coupling of the cells within one rack. With minor modifications to the cells, the current collectors of neighboring cells can be electrically interconnected via bipolar plates. Thereby, up to four single cells could be transformed into one bipolar short stack. This would provide the unique opportunity to test parallelized bipolar short stacks in a highly automated HT environment.

Process variability

One further important objective was to cover a wide range of different processes. Primarily, the system will be run with water and CO_2 electrolysis. For water electrolysis, the focus is mainly on AWE and AEM WE, while for CO_2 electrolysis, the focus is on the CO_2-to-CO, to-formic acid, and to-C_{2+} processes. Beyond this, the system can be used to investigate other processes such as proton exchange membrane water electrolysis or organic electrochemistry. With minor system modifications, it is technically possible to switch to other electrochemical systems such as redox flow batteries. However, any practicable process change must be accompanied by thorough cleaning procedures in order to avoid contamination from previous processes. The high process variability is facilitated by various aspects.

Different electrolysis processes require various cell concepts. The modular design of the flow cell enables its adaptability to all common cell concepts and, thus, ensures a high degree of process variability. Process variability also requires the HT system to be operated with different electrolytes, including solutions with high chemical corrosion activity.

To avoid contamination, all system components in contact with the electrolyte during operation are made of chemically inert polymers (cf. Chapter 5). Most commonly investigated electrolyte solutions can therefore be used in the system.

For various electrolysis processes toxic (e.g. CO) or flammable gases (e.g. H_2) are required as feedstock or are generated as product. An appropriate gas management to prevent the formation of dangerous concentrations of toxic or flammable gases is therefore important. All feed and product gases are released directly to the exhaust (no recirculation). Furthermore, the HT system is installed in an enclosure, in which the air is continuously circulated and vented to the exhaust. Therefore, no gas leaks into the laboratory. In addition, sensors for the most important hazardous gases are located inside the enclosure to detect dangerous gas concentrations. In the case of a gas leakage in the system, the detection signal triggers appropriate safety measures depending on the hazard level.

Chapter 7

Conclusion

Economically viable electrolysis technologies will play an important role in the future energy system. However, the complexity of electrolysis technologies and their high-dimensional electrochemical parameter space poses significant challenges to the development of electrolysis processes. Innovative high-throughput test platforms have the potential to serve as an ideal tool to efficiently accelerate process development in such a complex and high-dimensional research environment. However, existing high-throughput test systems have so far provided only limited solutions, as they either support only abstract experimental conditions or have been specifically designed for a single application or process.

This work focused on the development of an innovative high-throughput test system designed to accelerate the research and development of electrolysis processes. The project was carried out as an industrial collaboration between the Institute of Energy Technologies – Fundamental Electrochemistry (IET-1, Jülich, Germany) and hte GmbH (Heidelberg, Germany). The system enables the parallel testing of 16 electrolysis flow cells under industrially relevant conditions and meets all technical requirements for the operation of various electrolysis processes and applications. The aim of this project is to introduce a paradigm shift in high-throughput electrochemistry research by overcoming the key limitations of prior technologies with the system developed.

The extensive sensor and controller equipment enables precise monitoring and control of all relevant process and electrochemical parameters. The high level of automation minimizes the need for manual intervention, further accelerating screening procedures and enhancing the comparability of the generated results between the parallel operated cells. The system has been designed in accordance with industry standards to facilitate technology transfer toward commercial application and improve data comparability with both literature and industrial benchmarks. It is specifically designed for research on all relevant low-temperature water electrolysis and CO_2 electrolysis processes.

During the system engineering phase, various technical work packages were derived, planned, and scientifically investigated as part of this thesis.

- Characterization, validation, and optimization of the newly developed high-throughput flow cell,
- investigation of stray current formation in the high-throughput test system in case of a common electrolyte supply for parallel cells,
- investigation of metal ion contamination risk through austenitic stainless steel components in the electrolyte circuit, and
- validation of system operation on a 4-fold prototype of the high-throughput test system.

The completion of these work packages contributed to the progress of the project and the generated data provided the basis for important system design decisions.

A new electrolysis flow cell was specially developed for the high-throughput test system to meet all scientific and operational requirements. This development was carried out in collaboration between hte GmbH (Heidelberg, Germany), Fraunhofer Institute for Microengineering and Microsystems (IMM, Mainz, Germany), and Institute of Energy Technologies – Fundamental Electrochemistry (IET-1, Jülich, Germany).

The electrolysis cell was experimentally characterized and validated as part of this thesis. Initial modifications were implemented and potential future optimizations were discussed to improve cell performance and comparability in parallel operation. The characterization and validation processes focused on alkaline water electrolysis and anion exchange membrane water electrolysis, testing the cell in finite-gap and zero-gap configurations using various methods. Validation tests revealed an exceptionally high ohmic resistance, attributed to a high contact resistance caused by a surface passivation layer and increased electrical resistance of the Ti grade 5 current collectors. By implementing a four-terminal sensing method via the electrical contact frame attached to the inside of the cell housing, the operating cell voltage in zero-gap alkaline water electrolysis was reduced by 337 mV to 2.42 V (500 mA/cm^2, 20 °C), representing a 12.2 % improvement in cell performance. Comparable performance optimizations using the four-terminal sensing were observed in other processes and at higher operating temperatures. Implemented modifications to the cell primarily focused on the current collectors, including the redesign of the flow field from multiple parallel channels to a single meandering channel. The meandering channel ensures that the entire fluid flows past the active electrode. This modification simplifies the determination of conversion rates. Additionally, the current collectors were coated with Pt and Au to reduce contact resistances. These precious metal coatings were experimentally validated using anion exchange membrane water electrolysis, achieving an all-time best performance of 2.19 V at 2 A/cm^2, corresponding to a 260 mV reduction (10.6 % improvement) in cell voltage compared to measurements with uncoated current collectors. The reduction in contact resistance due to the precious metal coatings will also increase the comparability of the results in parallel operation. Additional modifications were proposed and discussed to further optimize the performance and comparability of the second generation of the developed electrolysis flow cell. These include using alternative materials for the current collectors, reducing the electrode distance of the finite-gap configuration, and implementing additional electrical

connections specifically provided for the application of a four-terminal sensing.

The quantitative investigation of stray currents in a 16-cell high-throughput test system in case of a common electrolyte supply revealed critical insights into its formation behavior and implications for the design of the electrolyte supply system. The results of experimentally determined stray currents between two commercial flow cells formed the base for validating a newly developed equivalent circuit model. The model validation showed a tolerable deviation in estimated stray currents compared to the experimental data of 4.1 % at 500 mA/cm^2. This model was subsequently extended to a 16-cell system, where an inhomogeneous distribution of stray currents was observed with the highest stray current loads identified in the first and last cell. Under the investigated conditions, the total system stray current reached up to 184 mA. The stray currents could increase further at higher current density differences between the flow cells of the system. Key influencing factors included the number of flow cells N, tube resistance R_t, and the ratio of manifold resistance R_m to tube resistance R_t. By optimizing these parameters, the stray current was successfully reduced to less than 2 mA in the 16-cell equivalent circuit model. However, the study also highlighted several challenges. Stray current reduction to minimal levels required an increase in tube resistance, which would lead to a significant rise in pumping power due to increased tube length or reduced cross-section. Additionally, electrochemical interference between parallel cells caused signal noise and altered current/voltage signals, particularly problematic for low-current and low-voltage studies. Furthermore, a common electrolyte supply would introduce process implications, since a time-resolved detection of liquid products for individual cells would not be possible. Although it would offer economic advantages, the technical disadvantages of a common electrolyte supply outweigh these benefits. To prevent stray current interferences and to meet the stringent requirements of the high-throughput test system for precision, reproducibility, and process control, the electrolyte supply system was designed with 32

fully separated half-cell electrolyte circuits.

The risk of metal ion contamination due to chemical corrosion of austenitic steel in contact with various electrolyte solutions was experimentally investigated to assess the suitability of stainless steel components within the electrolyte circuit of the high-throughput test system. The results demonstrate that the type and concentration of metal ions detected over time vary significantly depending on the electrolyte solution. In all tested electrolyte solutions and deionized H_2O, Fe ion contaminations were observed after 7 d that exceeded the Fe concentration limit of 0.1 µmol/L reported in previous CO_2 electrolysis deactivation studies. Therefore, despite the economic and technical advantages of stainless steel, all components in direct contact with the electrolyte are made from inert polymers to prevent contamination, avoid process interferences, and ensure long-term stability of the high-throughput test system.

Finally, the system operation was successfully tested and validated using a 4-fold prototype of the high-throughput test system. For this purpose, standard electrochemical test methods were conducted in four parallel operated flow cells under nominally identical conditions, utilizing alkaline water electrolysis in zero-gap configuration. In addition to system validation, overall good comparability of the results was achieved, with a standard deviation of only 14.7 mV at 500 mA/cm^2 and an average cell voltage of 2.47 V. Comparability is expected to improve further in the final 16-fold system due to subsequently implemented modifications to the flow cell design and the integration of active temperature control.

Future work will focus on the operation of the high-throughput test system with CO_2 electrolysis. This will require initial testing of CO_2 electrolysis in the developed flow cell as single-cell experiments. Once these preliminary tests are completed, the process can be scaled up and tested in the final system with up to 16 cells operating in parallel. This will enable the validation of important cell and system functionalities that could not be addressed during the water electrolysis validation experiments conducted in the course of this thesis. This includes technical challenges

such as the flow cell assembly with gas diffusion electrode, the integration of a CO_2 feed gas into the system, precise differential pressure control between gas and liquid phase, gas phase analysis, and automated liquid sampling.

Appendix A

High-throughput flow cell

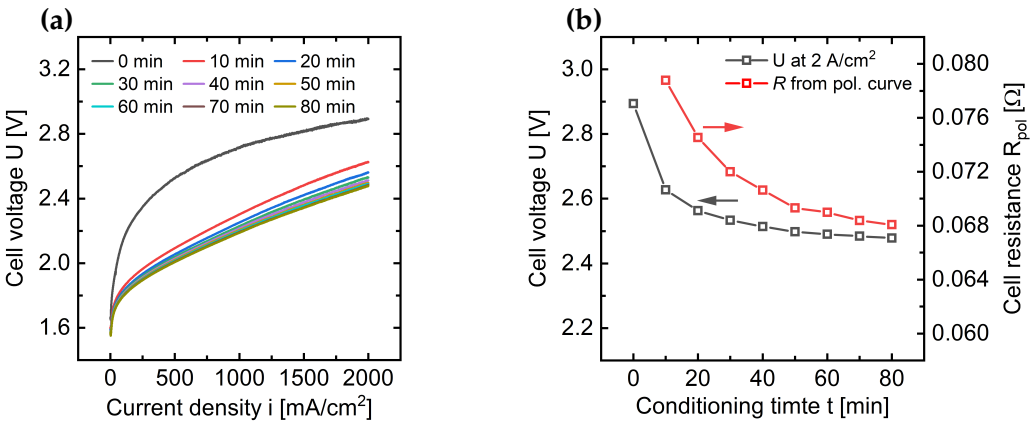

Figure A.1: The effect of conditioning time on cell performance tested with zero-gap AEM WE. (a) Polarization curves as well as (b) cell voltage U at 2000 mA/cm^2 and cell resistance R derived from polarization curves. Cell conditioning was conducted at 1000 mA/cm^2. Measurements were conducted at 20 °C and 1 barg with 40 ml/min at the site of the project partner hte GmbH.

Table A.1: Roughness factor f_R of smooth Ni foil calculated based on reduction peak of an anodic cyclic voltammetry scan (Ni(III) to Ni(II) transition) for different scan rates v.

v [mV/s]	I_{cat} [A·V]	Q_{cat} [mC]	f_R
5	148.43	29.69	14.1
10	241.52	24.16	11.5
15	325.20	21.68	10.3
20	411.89	20.59	9.81

Appendix B

Stray current investigations

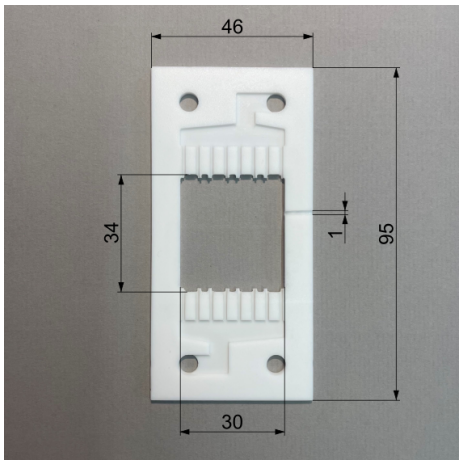

Figure B.1: Photo of the flow field with a 1 mm wide groove. The flow field has a thickness of 1.5 mm. All dimensions are in mm.

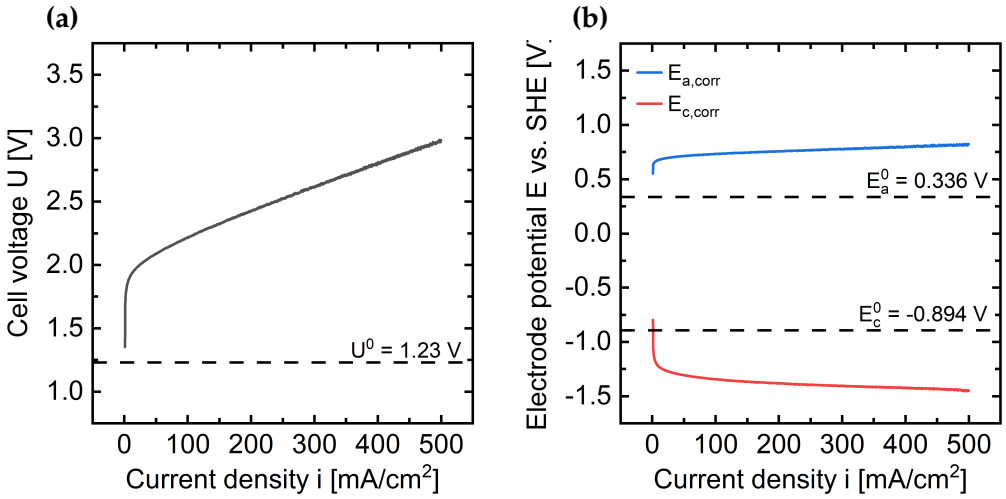

Figure B.2: (a) Cell voltage U as well as (b) anode and cathode electrode potential E vs. SHE (b) as a function of current density i. Experiment conducted in a commercially available Micro Flow Cell® purchased from ElectroCell A/S with AWE at 25 °C. Data were recorded using a linear scan (scan rate = 1 mA/s, step size = 2 mA). Dashed lines indicate the standard cell voltage of the overall reaction $U^0 = 1.23$ V as well as standard electrode potentials of the oxygen evolution reaction $E_a^0 = 0.336$ V and the hydrogen evolution reaction $E_c^0 = -0.894$ V for AWE.

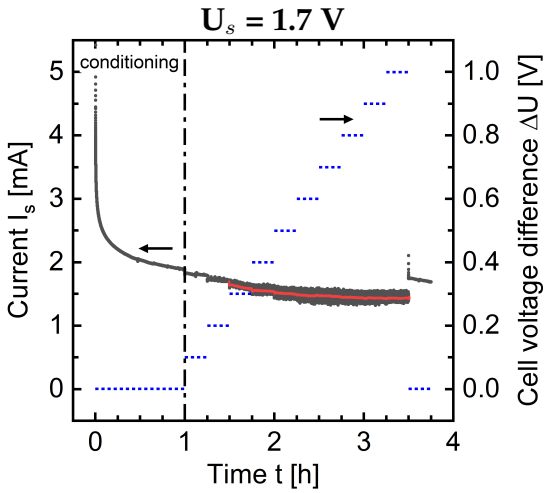

Figure B.3: Effect of deliberately increased cell voltage difference $\Delta U = U_d - U_s$ on cell current I_s. Repeat measurement at elevated start voltages $U_s = U_d = 1.7\,V$. I_s (left axis) at a constant cell voltage $U_s = 1.7\,V$ at all times with moving average (red line) and ΔU (right axis) are depicted as a function of time t. $Cell_d$ voltage U_d was increased by $\Delta U_d = \Delta U = 0.1\,V$ every 15 min starting from $U_d = U_s = 1.7\,V$ up to $U_d = 2.7\,V$. After 3.5 h ΔU was reset to 0 V.

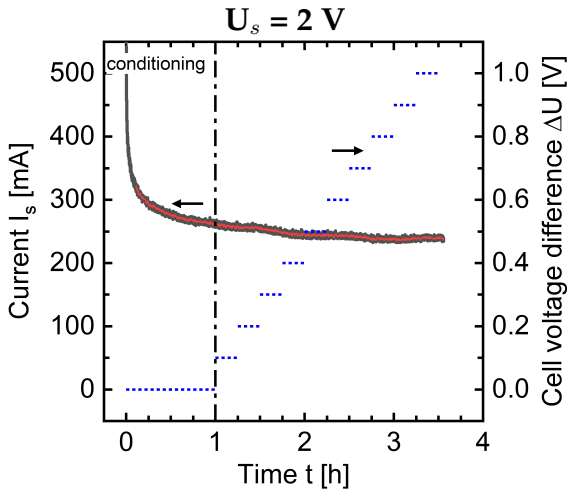

Figure B.4: Effect of deliberately increased cell voltage difference $\Delta U = U_d - U_s$ on cell current I_s. Repeat measurement at elevated start voltages $U_s = U_d = 2\,V$. I_s (left axis) at a constant cell voltage $U_s = 2\,V$ at all times with moving average (red line) and ΔU (right axis) are depicted as a function of time t. $Cell_d$ voltage U_d was increased by $\Delta U_d = \Delta U = 0.1\,V$ every 15 min starting from $U_d = U_s = 2\,V$ up to $U_d = 3\,V$.

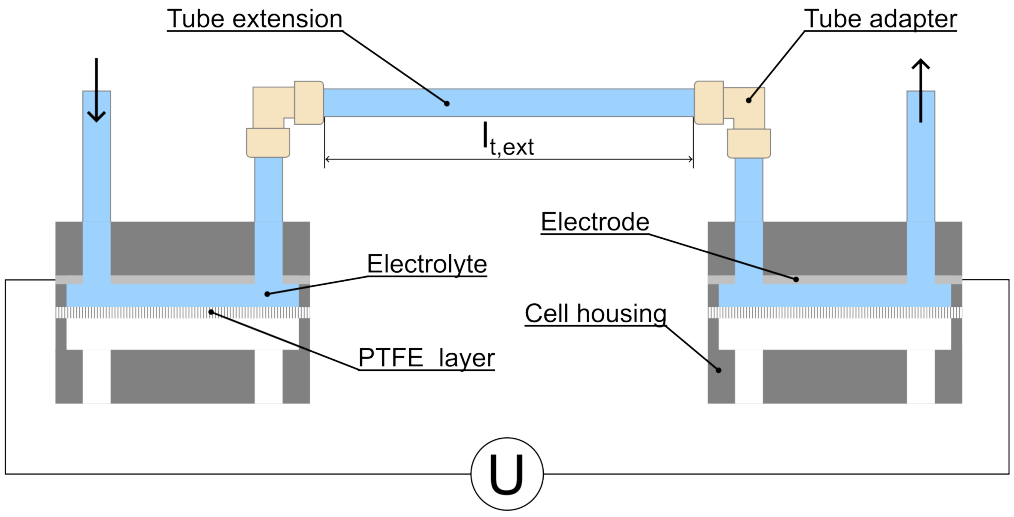

Figure B.5: Experimental setup to determine the ionic tube resistance R_t as a function of the length of the installed tube extension $l_{t,ext}$. Tube extensions with defined lengths $l_{t,ext}$ of 10, 20, and 30 cm were installed between both cells. R_t was measured with potentiostatic electrochemical impedance spectroscopy.

Additional charge transfers due to gas crossover

It is hypothesized that the hydrogen and oxygen crossover through the Zirfon Perl UTP 500 separator leads to an additional charge transfer that affects the measurement of the potential difference between adjacent electrodes ΔE_{aa} and ΔE_{cc} at low current densities in the dynamic cell.

A specific hydrogen crossover through the Zirfon separator of approximately $10^{-10}\,\mathrm{mol/cm^2/s}$ is estimated independent of the current density[127,154]. For simplicity, the crossover of oxygen molecules is not calculated in the following. It can be assumed that the oxygen crossover is significantly lower than that of hydrogen, since the molecules are larger and therefore less mobile. Furthermore, the charge transfer effect of the oxygen crossover is in the same direction as of the hydrogen crossover. The following equation can be used to calculate the total hydrogen crossover for each cell.

$$J_{H_2} = j_{H_2} \cdot A = 10^{-10}\,\frac{\mathrm{mol}}{\mathrm{cm^2 \cdot s}} \cdot 10\,\mathrm{cm^2} = 10^{-9}\,\frac{\mathrm{mol}}{\mathrm{s}} \tag{B.1}$$

J_{H_2}	Total hydrogen crossover per cell
j_{H_2}	Area specific hydrogen crossover
A	Area of Zirfon separator

It is further assumed that due to the catholyte flow, the dissolved hydrogen molecules in the catholyte are mixed within the electrolyte reservoir before participating in the hydrogen crossover. Therefore, at very low current densities in the dynamic cell ($i_d = 10\,\mathrm{mA/cm^2}$) it can be assumed that most of the crossover hydrogen molecules were originally formed in the static cell operating at $100\,\mathrm{mA/cm^2}$. As a simplification, it can be assumed that the fractions for $i_d = 10\,\mathrm{mA/cm^2}$ and $i_s = 100\,\mathrm{mA/cm^2}$ can be calculated as shown below. Equation B.2 becomes less valid with increasing current densities due to the smaller ratio of dissolved hydrogen molecules and very small hydrogen gas bubbles compared to the current density.

$$x_s = \frac{i_s}{i_s + i_d} = \frac{100\frac{mA}{cm^2}}{100\frac{mA}{cm^2} + 10\frac{mA}{cm^2}} = 0.91 \tag{B.2}$$

$$x_d = \frac{i_d}{i_s + i_d} = \frac{10\frac{mA}{cm^2}}{100\frac{mA}{cm^2} + 10\frac{mA}{cm^2}} = 0.09 \tag{B.3}$$

x_s Hydrogen crossover fraction originating from static cell
x_d Hydrogen crossover fraction originating from dynamic cell
i_s Current density static cell $i_s = 100\,\mathrm{mA/cm^2}$
i_d Current density dynamic cell $i_d = 10\,\mathrm{mA/cm^2}$

Similar to the catholyte reservoir, the dissolved crossover hydrogen from both cells is mixed in the anolyte reservoir, before being oxidized at the anode. Due to the very high overpotential for hydrogen oxidation at the anode in both cells, half of the hydrogen dissolved in the anolyte is oxidized in each cell.

$$\begin{aligned} J_{H_2,s-d} = \frac{(x_s - x_d) \cdot J_{H_2} \cdot n}{2} &= \frac{(0.91 - 0.09) \cdot 10^{-9}\,\frac{\mathrm{mol}}{\mathrm{s}} \cdot 2}{2} \\ &= 8.2 \cdot 10^{-10}\,\frac{\mathrm{mol}}{\mathrm{s}} \end{aligned} \tag{B.4}$$

$J_{H_2,s-d}$ Hydrogen transferred from the cathode of the static cell towards the anode of the dynamic cell
j_{H_2} Area specific hydrogen crossover
A Area of Zirfon separator

Using Faraday's law, this hydrogen crossover from the cathode of the static cell to the anode of the dynamic cell can be converted into an electric current of 0.16 mA.

$$I_{H_2,s-d} = J_{H_2,s-d} \cdot F \cdot z = 8.2 \cdot 10^{-10} \frac{\text{mol}}{\text{s}} \cdot 96485 \frac{\text{C}}{\text{mol}} \cdot 2 = 0.16\,\text{mA} \tag{B.5}$$

$I_{H_2,s-d}$	Effective current transferred by the hydrogen crossover
F	Faraday constant
z	Number of exchange electrons

Due to several assumptions in the calculation, this value should only be considered as an order of magnitude estimate. However, when this value is compared to the calculated stray currents shown in Figure 4.6, the relationship becomes clearer. When operating the dynamic cell at $10\,\text{mA/cm}^2$, a total shunt current of approximately $0.6\,\text{mA}$ was observed. If this is perturbed by an additional asymmetrical current through the hydrogen crossover in the order of $0.16\,\text{mA}$, deviations in the potential difference as shown in Figure 4.2 can be expected.

Total Number of cells (N)	Cell index (k)															
	1	2	3	4	5	6	7	8	9	10	11	12	13	14	15	16
2	100	200														
3	100	200	300													
4	100	200	300	400												
5	100	200	300	400	500											
6	100	200	300	400	500	600										
7	100	200	300	400	500	600	700									
8	100	200	300	400	500	600	700	800								
9	100	200	300	400	500	600	700	800	900							
10	100	200	300	400	500	600	700	800	900	1000						
11	100	200	300	400	500	600	700	800	900	1000	1100					
12	100	200	300	400	500	600	700	800	900	1000	1100	1200				
13	100	200	300	400	500	600	700	800	900	1000	1100	1200	1300			
14	100	200	300	400	500	600	700	800	900	1000	1100	1200	1300	1400		
15	100	200	300	400	500	600	700	800	900	1000	1100	1200	1300	1400	1500	
16	100	200	300	400	500	600	700	800	900	1000	1100	1200	1300	1400	1500	1600

Table B.1: Current density distribution in (mA/cm^2) with constant cell-to-cell current density difference $\Delta i = 100\,mA/cm^2$ for increasing total number of cells N.

Total Number of cells (N)	Cell index (k)															
	1	2	3	4	5	6	7	8	9	10	11	12	13	14	15	16
2	100	1000														
3	100	550	1000													
4	100	400	700	1000												
5	100	325	550	775	1000											
6	100	280	460	640	820	1000										
7	100	250	400	550	700	850	1000									
8	100	229	357	486	614	743	871	1000								
9	100	213	325	438	550	663	775	888	1000							
10	100	200	300	400	500	600	700	800	900	1000						
11	100	190	280	370	460	550	640	730	820	910	1000					
12	100	182	264	345	427	509	591	673	755	836	918	1000				
13	100	175	250	325	400	475	550	625	700	775	850	925	1000			
14	100	169	238	308	377	446	515	585	654	723	792	862	931	1000		
15	100	164	229	293	357	421	486	550	614	679	743	807	871	936	1000	
16	100	160	220	280	340	400	460	520	580	640	700	760	820	880	940	1000

Table B.2: Current density distribution in (mA/cm^2) with constant current densities of the boundary cells $i_1 = 100\,mA/cm^2$ and $i_N = 1000\,mA/cm^2$ for increasing total number of cells N.

Appendix C

Stainless steel contamination investigations

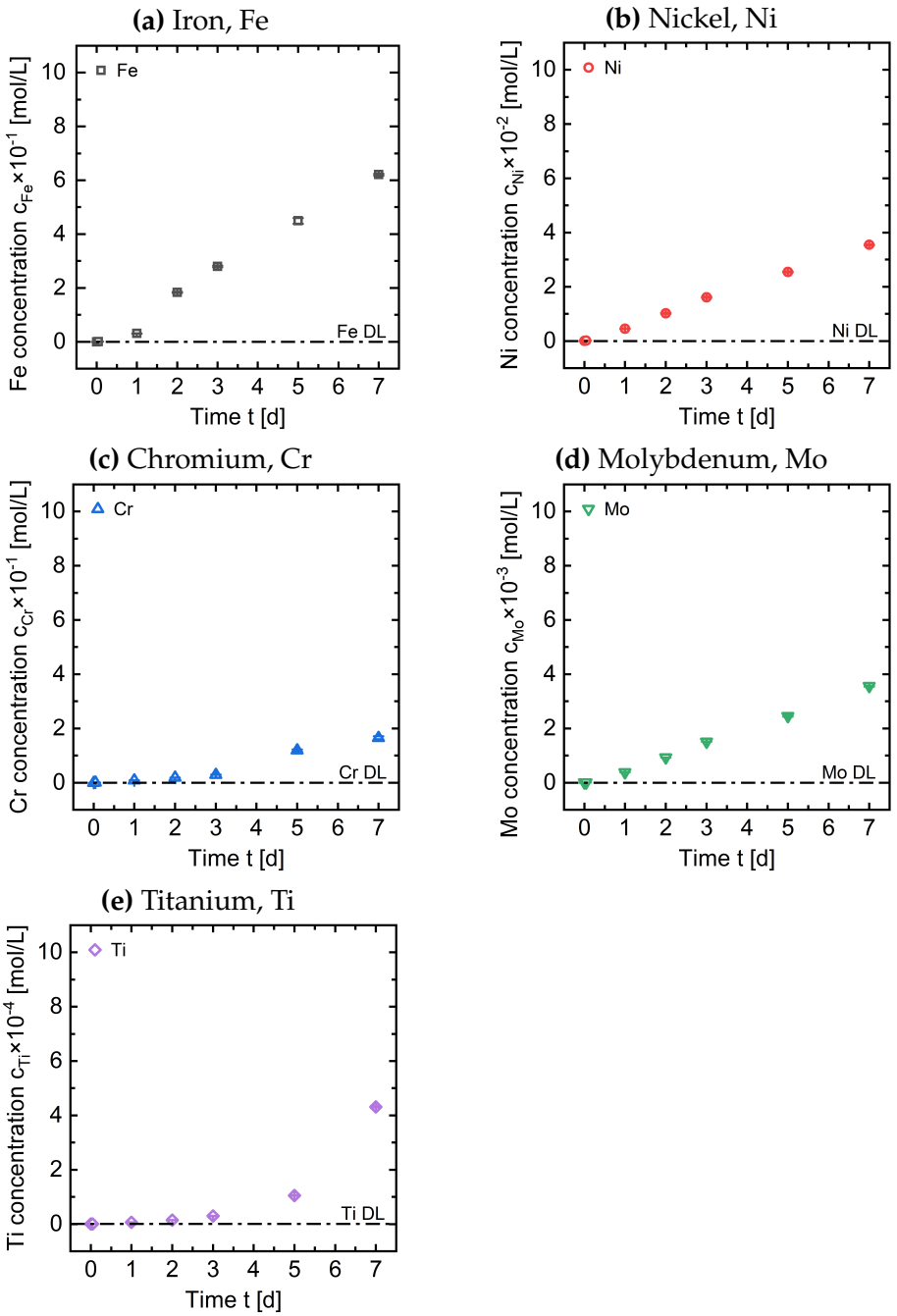

Figure C.1: Metal ion contamination of (a) iron Fe, (b) nickel Ni, (c) chromium Cr, (d) molybdenum Mo, and (e) titanium Ti in 6 M HCl due to contact with AISI 316Ti (EN 1.4571) stainless steel. Analyzes were conducted with ICP-OES. Fe, Ni, Cr, Mo, and Ti detection limits in 6 M HCl are $5.4{\cdot}10^{-7}$, $6.8{\cdot}10^{-7}$, $9.6{\cdot}10^{-7}$, $4.2{\cdot}10^{-7}$, and $2.1{\cdot}10^{-7}$ mol/L, respectively.

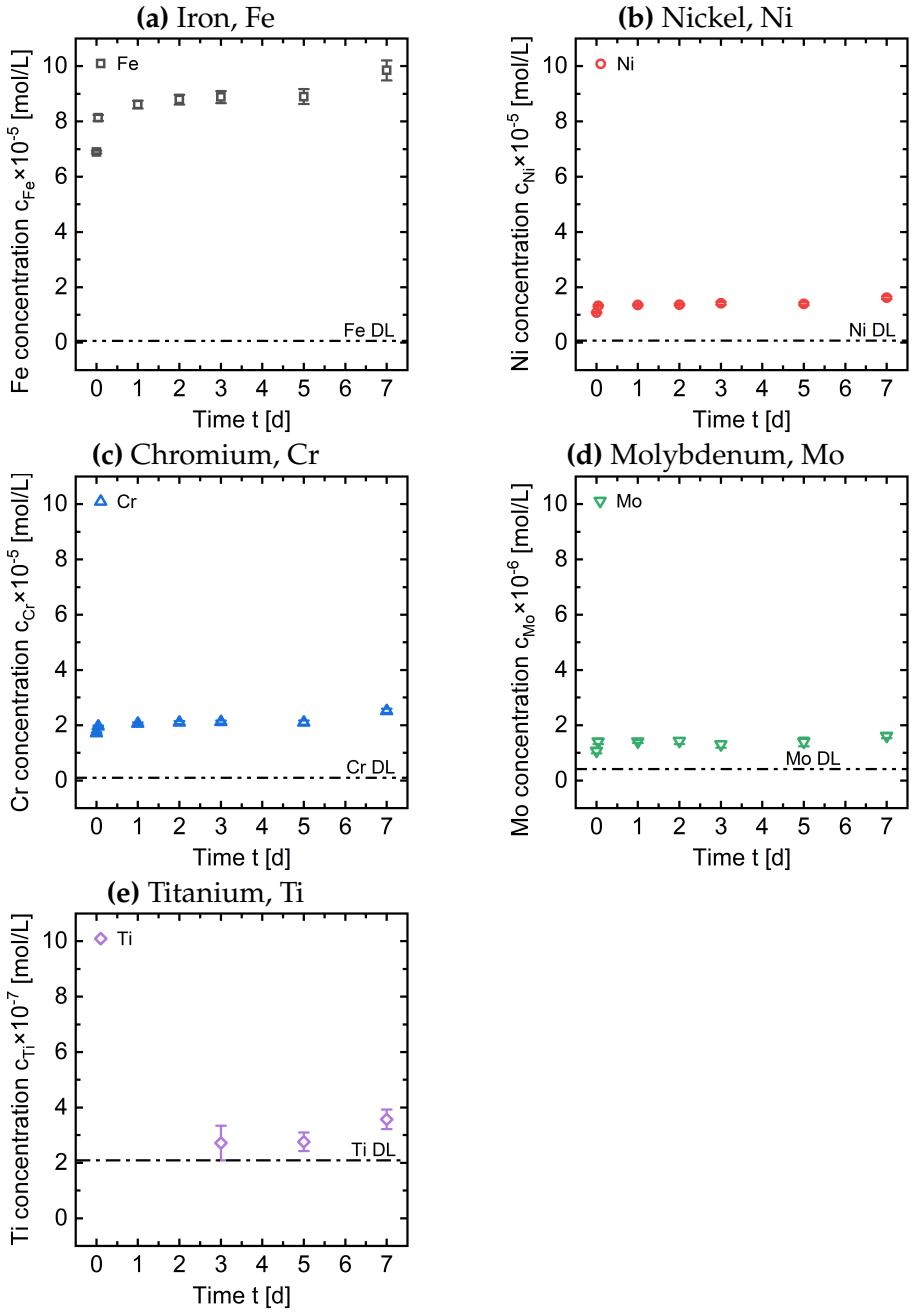

Figure C.2: Metal ion contamination of (a) iron Fe, (b) nickel Ni, (c) chromium Cr, (d) molybdenum Mo, and (e) titanium Ti in 2 M H_2SO_4 due to contact with AISI 316Ti (EN 1.4571) stainless steel. Analyzes were conducted with ICP-OES. Fe, Ni, Cr, Mo, and Ti detection limits in 2 M H_2SO_4 are $5.4{\cdot}10^{-7}$, $6.8{\cdot}10^{-7}$, $9.6{\cdot}10^{-7}$, $4.2{\cdot}10^{-7}$, and $2.1{\cdot}10^{-7}$ mol/L, respectively.

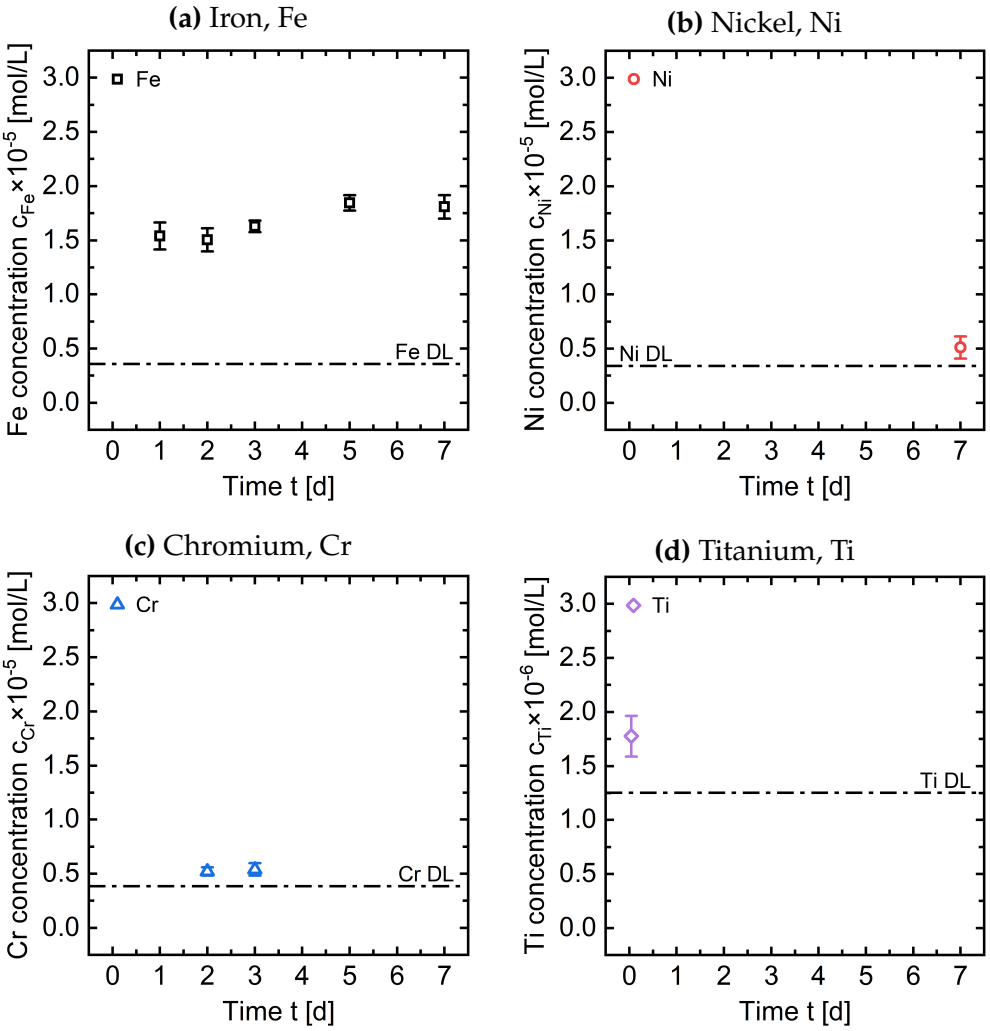

Figure C.3: Metal ion contamination of (a) iron Fe, (b) nickel Ni, (c) chromium Cr, and (d) titanium Ti in 2 M NaCl due to contact with AISI 316Ti (EN 1.4571) stainless steel. Analyzes were conducted with ICP-OES. Fe, Ni, Cr, and Ti detection limits in 2 M NaCl are $3.6{\cdot}10^{-6}$, $3.4{\cdot}10^{-6}$, $3.8{\cdot}10^{-6}$, and $1.3{\cdot}10^{-6}$ mol/L, respectively.

Bibliography

[1] D. Dogan, B. Hecker, X. Hou, I. Dessel, A. Müller, G. Wasserschaff, S. S. Köcher, V. Karyofylli, H. Kungl, H. Tempel, R.-A. Eichel, *Electrochemical Science Advances* **2024**.

[2] D. Dogan, B. Hecker, B. Schmid, H. Kungl, H. Tempel, R.-A. Eichel, *Electrochimica Acta* **2024**, *500*, 144767.

[3] A. Müller, F. Schneider, F. Huber, M. Dejmek, G. Wasserschaff, O. Püttmann, J. Fechtmann, D. Zahlmann, C. Hose, F. Eversheim, F. Huber, B. Hecker, D. Dogan, H. Tempel, R.-A. Eichel, P. Löb, C. Hofmann, A. Ziogas, H. Krost, C. Kröger, S. Haug, S. Coenen in Conference Proceedings - The Role of Catalysis for the Energy Transition, *Vol. 3*, **2022**, pp. 104–121.

[4] I. Dessel, D. Dogan, R.-A. Eichel, B. Hecker, C. Hofmann, F. Huber, A. Jakob, H.-J. Kost, P. Löb, A. Müller, et al., *Chemie Ingenieur Technik* **2024**.

[5] M. F. Rabbi, J. Popp, D. Máté, S. Kovács, *Energies* **2022**, *15*, 8126.

[6] R. Asha Rani N, T. Laishram, S. Bal, *Nanomaterials and Energy* **2023**, *12*, 100–109.

[7] International Renewable Energy Agency, World Energy Transitions Outlook 2024: 1.5°C Pathway, `https://www.irena.org/-/media/Files/IRENA/Agency/Publication/2024/Nov/IRENA_World_energy_transitions_outlook_2024.pdf`, Abu Dhabi, **2024**.

[8] International Renewable Energy Agency, A quality infrastructure roadmap for green hydrogen, https://www.irena.org/-/media/Files/IRENA/Agency/Publication/2024/Nov/IRENA_Quality_infrastructure_roadmap_green_hydrogen_2024.pdf, Abu Dhabi, **2024**.

[9] A. J. Shih, M. C. Monteiro, F. Dattila, D. Pavesi, M. Philips, A. H. da Silva, R. E. Vos, K. Ojha, S. Park, O. van der Heijden, et al., *Nature Reviews Methods Primers* **2022**, *2*, 84.

[10] M. Paidar, V. Fateev, K. Bouzek, *Electrochimica acta* **2016**, *209*, 737–756.

[11] S. Grigoriev, V. Fateev, D. Bessarabov, P. Millet, *International Journal of Hydrogen Energy* **2020**, *45*, 26036–26058.

[12] D. Hua, J. Huang, E. Fabbri, M. Rafique, B. Song, *ChemElectroChem* **2023**, *10*, e202200999.

[13] S. A. Lee, J. Kim, K. C. Kwon, S. H. Park, H. W. Jang, *Carbon Neutralization* **2022**, *1*, 26–48.

[14] J. DeAngelo, I. Azevedo, J. Bistline, L. Clarke, G. Luderer, E. Byers, S. J. Davis, *Nature communications* **2021**, *12*, 6096.

[15] S. Nitopi, E. Bertheussen, S. B. Scott, X. Liu, A. K. Engstfeld, S. Horch, B. Seger, I. E. Stephens, K. Chan, C. Hahn, et al., *Chemical reviews* **2019**, *119*, 7610–7672.

[16] Y. Hori, K. Kikuchi, S. Suzuki, *Chemistry letters* **1985**, *14*, 1695–1698.

[17] I. E. Stephens, K. Chan, A. Bagger, S. W. Boettcher, J. Bonin, E. Boutin, A. K. Buckley, R. Buonsanti, E. R. Cave, X. Chang, et al., *Journal of Physics: Energy* **2022**, *4*, 042003.

[18] S. Overa, B. H. Ko, Y. Zhao, F. Jiao, *Accounts of chemical research* **2022**, *55*, 638–648.

[19] J. Wu, Y. Huang, W. Ye, Y. Li, *Advanced Science* **2017**, *4*, 1700194.

[20] J. Schneider, H. Jia, J. T. Muckerman, E. Fujita, *Chemical Society Reviews* **2012**, *41*, 2036–2051.

[21] S. Liang, N. Altaf, L. Huang, Y. Gao, Q. Wang, *Journal of CO2 Utilization* **2020**, *35*, 90–105.

[22] J. Qiao, Y. Liu, J. Zhang, *Electrochemical reduction of carbon dioxide: fundamentals and technologies*, CRC press, **2016**.

[23] H. Tüysüz, *Accounts of Chemical Research* **2024**, *57*, 558–567.

[24] International Renewable Energy Agency, Green Hydrogen Cost Reduction: Scaling up Electrolysers to Meet the 1.5 °C Climate Goal, `https://www.irena.org/-/media/Files/IRENA/Agency/Publication/2020/Dec/IRENA_Green_hydrogen_cost_2020.pdf`, Abu Dhabi, **2020**.

[25] S. Sebbahi, A. Assila, A. A. Belghiti, S. Laasri, S. Kaya, S. Rachidi, A. Hajjaji, et al., *International Journal of Hydrogen Energy* **2024**, *82*, 583–599.

[26] R. I. Masel, Z. Liu, H. Yang, J. J. Kaczur, D. Carrillo, S. Ren, D. Salvatore, C. P. Berlinguette, *Nature nanotechnology* **2021**, *16*, 118–128.

[27] A. J. Martín, G. O. Larrazábal, J. Pérez-Ramírez, *Green Chemistry* **2015**, *17*, 5114–5130.

[28] H. Shin, K. U. Hansen, F. Jiao, *Nature Sustainability* **2021**, *4*, 911–919.

[29] T. Muster, A. Trinchi, T. Markley, D. Lau, P. Martin, A. Bradbury, A. Bendavid, S. Dligatch, *Electrochimica Acta* **2011**, *56*, 9679–9699.

[30] A. K. Schuppert, A. A. Topalov, I. Katsounaros, S. O. Klemm, K. J. Mayrhofer, *Journal of The Electrochemical Society* **2012**, *159*, F670.

[31] D. A. Pereira, J. A. Williams, *British journal of pharmacology* **2007**, *152*, 53–61.

[32] R. Potyrailo, K. Rajan, K. Stoewe, I. Takeuchi, B. Chisholm, H. Lam, *ACS combinatorial science* **2011**, *13*, 579–633.

[33] P. Strasser, A. Hagemeyer, A. F. Volpe, *High-throughput Screening in Heterogeneous [ie Chemical] Catalysis*, Wiley-VCH, **2004**.

[34] A. G. Wills, S. Charvet, C. Battilocchio, C. C. Scarborough, K. M. Wheelhouse, D. L. Poole, N. Carson, J. C. Vantourout, *Organic Process Research & Development* **2021**, *25*, 2587–2600.

[35] H. Chen, Y. Mo, *Synthesis* **2023**, *55*, 2817–2832.

[36] C. Martens, B. Schmid, H. Tempel, R.-A. Eichel, *Green chemistry* **2023**, *25*, 7794–7806.

[37] B. H. Gerroll, K. M. Kulesa, C. A. Ault, L. A. Baker, *ACS Measurement Science Au* **2023**, *3*, 371–379.

[38] J. L. Hitt, Y. C. Li, S. Tao, Z. Yan, Y. Gao, S. J. Billinge, T. E. Mallouk, *Nature Communications* **2021**, *12*, 1114.

[39] D. Guevarra, J. A. Haber, Y. Wang, L. Zhou, K. Kan, M. H. Richter, J. M. Gregoire, *Electrocatalysis* **2022**, 1–10.

[40] E. Reddington, A. Sapienza, B. Gurau, R. Viswanathan, S. Sarangapani, E. S. Smotkin, T. E. Mallouk, *Science* **1998**, *280*, 1735–1737.

[41] M. G. Sullivan, H. Utomo, P. J. Fagan, M. D. Ward, *Analytical Chemistry* **1999**, *71*, 4369–4375.

[42] C. J. Warren, R. C. Haushalter, L. Matsiev, Method for creating and testing a combinatorial array employing individually addressable electrodes, US Patent 6,187,164, **2001**.

[43] J. S. Cooper, P. J. McGinn, *Applied Surface Science* **2007**, *254*, 662–668.

[44] R. Hahn, M. Ferch, K. Tribowski, N. A. Kyerematen, K. Hoeppner, K. Marquardt, K.-D. Lang, W. Bock, *Microsystem Technologies* **2019**, *25*, 1137–1149.

[45] W. Markle, B. Speiser, C. Tittel, M. Vollmer, *Electrochimica Acta* **2005**, *50*, 4916–4925.

[46] E. Lindner, Z.-L. Lu, H. A. Mayer, B. Speiser, C. Tittel, I. Warad, *Electrochemistry communications* **2005**, *7*, 1013–1020.

[47] T. Siu, W. Li, A. K. Yudin, *Journal of Combinatorial Chemistry* **2000**, *2*, 545–549.

[48] C. Ley, S. Z. Çekiç, S. Kochius, K.-M. Mangold, U. Schwaneberg, J. Schrader, D. Holtmann, *Electrochimica Acta* **2013**, *89*, 98–105.

[49] J. Rein, J. R. Annand, M. K. Wismer, J. Fu, J. C. Siu, A. Klapars, N. A. Strotman, D. Kalyani, D. Lehnherr, S. Lin, *ACS Central Science* **2021**, *7*, 1347–1355.

[50] C. Gütz, B. Klöckner, S. R. Waldvogel, *Organic Process Research & Development* **2016**, *20*, 26–32.

[51] A. Juneau, M. Abdolhosseini, C. Rocq, H. D. Pham, M. Pascall, R. Z. Khaliullin, S. Canesi, E. McCalla, J. Mauzeroll, *ChemElectroChem* **2024**, e202400193.

[52] I.-W. G. C. KG, IKA e-Hive Electrochemistry Kit, `https://www.ika.com/de/Produkte-LabEq/Electrochemistry-Kit-pg516/IKA-e-Hive-40004945/`, Accessed: 2025-01-08.

[53] I.-W. G. C. KG, IKA Carousel Electrochemistry Kit, `https://www.ika.com/de/Produkte-LabEq/Electrochemistry-Kit-pg516/IKA-Carousel-20017512/`, Accessed: 2025-01-08.

[54] I.-W. G. C. KG, IKA Screening System Package 6 Zellen, `https://www.ika.com/de/Produkte-LabEq/Screening-System-pg913/Screening-System-Package-(6-Zellen)-40003631/`, Accessed: 2025-01-08.

[55] I.-W. G. C. KG, IKA Screening System Package 8 Zellen, `https://www.ika.com/de/Produkte-LabEq/Screening-System-pg913/Screening-System-Package-(8-Zellen)-40003642/`, Accessed: 2025-01-08.

[56] R. Liu, E. S. Smotkin, *Journal of Electroanalytical Chemistry* **2002**, *535*, 49–55.

[57] Y. Lai, R. J. Jones, Y. Wang, L. Zhou, J. M. Gregoire, *ACS combinatorial science* **2019**, *21*, 692–704.

[58] R. Becker, K. Weber, T. V. Pfeiffer, J. v. Kranendonk, K. J. Schouten, *Catalysts* **2020**, *10*, 1165.

[59] Y. Mo, G. Rughoobur, A. M. Nambiar, K. Zhang, K. F. Jensen, *Angewandte Chemie* **2020**, *132*, 21076–21080.

[60] T. Kose, C. P. O'Brien, J. Wicks, J. Abed, Y. C. Xiao, B. Sutherland, A. Sarkar, S. A. Jaffer, E. H. Sargent, D. Sinton, *Catalysis Science & Technology* **2022**, *12*, 6239–6245.

[61] M. Maril, J.-L. Delplancke, N. Cisternas, P. Tobosque, Y. Maril, C. Carrasco, *International Journal of Hydrogen Energy* **2022**, *47*, 3532–3549.

[62] G. Bender, M. Carmo, T. Smolinka, A. Gago, N. Danilovic, M. Mueller, F. Ganci, A. Fallisch, P. Lettenmeier, K. A. Friedrich, et al., *International journal of hydrogen energy* **2019**, *44*, 9174–9187.

[63] M. H. Barecka, J. W. Ager, *Energy Advances* **2023**, *2*, 268–279.

[64] R. Qi, M. Becker, J. Brauns, T. Turek, J. Lin, Y. Song, *Journal of Power Sources* **2023**, *579*, 233222.

[65] I. Rousar, J. Thonstad, *Journal of applied electrochemistry* **1994**, *24*, 1124–1132.

[66] M. Skyllas-Kazacos, J. McCann, Y. Li, J. Bao, A. Tang, *ChemistrySelect* **2016**, *1*, 2249–2256.

[67] N. M. Delgado, R. Monteiro, J. Cruz, A. Bentien, A. Mendes, *Electrochimica Acta* **2022**, *403*, 139667.

[68] S. Titlbach, C. Futter, M. Lejkowski, A. Lange de Oliveira, S. A. Schunk, *Chemie Ingenieur Technik* **2014**, *86*, 1013–1028.

[69] E. Kaminski, R. Savinell, *J. Electrochem. Soc.;(United States)* **1983**, *130*.

[70] C. Yin, S. Guo, H. Fang, J. Liu, Y. Li, H. Tang, *Applied Energy* **2015**, *151*, 237–248.

[71] A. N. Colli, J. M. Bisang, *AIChE Journal* **2021**, *67*, e17371.

[72] N. Esfandiari, M. Aliofkhazraei, A. N. Colli, F. C. Walsh, S. Cherevko, L. A. Kibler, M. M. Elnagar, P. D. Lund, D. Zhang, S. Omanovic, et al., *Progress in Materials Science* **2024**, 101254.

[73] L. Arenas, C. P. De León, F. Walsh, *Journal of Energy Storage* **2017**, *11*, 119–153.

[74] D. Pletcher, F. C. Walsh, *Industrial electrochemistry*, Springer Science & Business Media, **2012**.

[75] A. N. Colli, H. Girault, *Journal of The Electrochemical Society* **2017**, *164*, E3465.

[76] A. Kuhn, J. Booth, *Journal of Applied Electrochemistry* **1980**, *10*, 233–237.

[77] V. M. Schmidt, *Elektrochemische Verfahrenstechnik: Grundlagen, Reaktionstechnik, Prozessoptimierung*, John Wiley & Sons, **2012**.

[78] Y. Tsou, *Transactions of the Electrochemical Society* **1942**, *82*, 353.

[79] P. R. Prokopius, Model for calculating electrolytic shunt path losses in large electrochemical energy conversion systems, tech. rep., Lewis Research Center, National Aeronautics and Space Administration, **1976**.

[80] J. Burnett, D. Danly in AIChE Symp Ser, *Vol. 8*, **1979**, p. 13.

[81] G. Codina, A. Aldaz, *Journal of applied electrochemistry* **1992**, *22*, 668–674.

[82] G. Codina, J. Perez, M. Lopez-Atalaya, J. Vasquez, A. Aldaz, *Journal of Power Sources* **1994**, *48*, 293–302.

[83] M. Katz, *Journal of the Electrochemical Society* **1978**, *125*, 515.

[84] G. McLean, T. Niet, S. Prince-Richard, N. Djilali, *International Journal of Hydrogen Energy* **2002**, *27*, 507–526.

[85] J. A. Schaeffer, L.-D. Chen, J. P. Seaba, *Journal of power sources* **2008**, *182*, 599–602.

[86] G. Zhou, L.-D. Chen, J. P. Seaba, *Journal of Power Sources* **2011**, *196*, 8180–8187.

[87] F. Wandschneider, S. Röhm, P. Fischer, K. Pinkwart, J. Tübke, H. Nirschl, *Journal of Power Sources* **2014**, *261*, 64–74.

[88] Q. Ye, J. Hu, P. Cheng, Z. Ma, *Journal of Power Sources* **2015**, *296*, 352–364.

[89] P. Pirotskii, N. Shvetsov, *Measurement Techniques* **1961**, *4*, 993–995.

[90] I. Roušar, V. Cezner, *Journal of the Electrochemical Society* **1974**, *121*, 648.

[91] H. Fink, M. Remy, *Journal of Power Sources* **2015**, *284*, 547–553.

[92] E. Henquín, J. Bisang, *Journal of applied electrochemistry* **2007**, *37*, 877–886.

[93] E. Henquín, J. Bisang, *Journal of Applied Electrochemistry* **2008**, *38*, 1259–1267.

[94] M. Boivineau, C. Cagran, D. Doytier, V. Eyraud, M. .-. Nadal, B. Wilthan, G. Pottlacher, *International journal of thermophysics* **2006**, *27*, 507–529.

[95] M. Finšgar, I. Milošev, *Corrosion science* **2010**, *52*, 2430–2438.

[96] C. Schroer, O. Wedemeyer, J. Novotny, A. Skrypnik, J. Konys, *Journal of nuclear materials* **2011**, *418*, 8–15.

[97] Y. J. Son, S. Kim, V. Leung, K. Kawashima, J. Noh, K. Kim, R. A. Marquez, O. A. Carrasco-Jaim, L. A. Smith, H. Celio, et al., *ACS Catalysis* **2022**, *12*, 10384–10399.

[98] K. S. Barros, M. C. Martí-Calatayud, T. Scarazzato, A. M. Bernardes, D. C. R. Espinosa, V. Pérez-Herranz, *Advances in Colloid and Interface Science* **2021**, *293*, 102439.

[99] M. A. Pellitero, S. D. Curtis, N. Arroyo-Curras, *ACS sensors* **2021**, *6*, 1199–1207.

[100] J. Ho, D.-L. Piron, *Journal of applied electrochemistry* **1996**, *26*, 515–521.

[101] M. E. Lyons, M. P. Brandon, *Journal of Electroanalytical Chemistry* **2010**, *641*, 119–130.

[102] S. Hernandez-Aldave, E. Andreoli, *Catalysts* **2020**, *10*, 713.

[103] M. R. Kraglund, PhD thesis, Department of Energy Conversion and Storage, Technical University of Denmark, **2017**.

[104] J. Haverkort, H. Rajaei, *Journal of Power Sources* **2021**, *497*, 229864.

[105] C. G. Zoski, *Handbook of electrochemistry*, Elsevier, **2006**, p. 16.

[106] J. Kai, R. Saito, K. Terabaru, H. Li, H. Nakajima, K. Ito, *Journal of The Electrochemical Society* **2019**, *166*, F246.

[107] M. Bonanno, K. Müller, B. Bensmann, R. Hanke-Rauschenbach, D. Aili, T. Franken, A. Chromik, R. Peach, A. T. Freiberg, S. Thiele, *Advanced Materials Technologies* **2024**, *9*, 2300281.

[108] A. Govind Rajan, J. M. P. Martirez, E. A. Carter, *ACS Catalysis* **2021**, *11*, 11305–11319.

[109] H. Qiu, K. Obata, Z. Yuan, T. Nishimoto, Y. Lee, K. Nagato, I. Kinefuchi, J. Shiomi, K. Takanabe, *Langmuir* **2023**, *39*, 4993–5001.

[110] A. Taqieddin, R. Nazari, L. Rajic, A. Alshawabkeh, *Journal of The Electrochemical Society* **2017**, *164*, E448.

[111] E. P. Randviir, *Electrochimica Acta* **2018**, *286*, 179–186.

[112] A. C. Garcia, T. Touzalin, C. Nieuwland, N. Perini, M. T. Koper, *Angewandte Chemie International Edition* **2019**, *58*, 12999–13003.

[113] D. S. Hall, C. Bock, B. R. MacDougall, *Journal of The Electrochemical Society* **2013**, *160*, F235.

[114] A. Podobaev, S. Kruglikov, P. Becker, M. Mattiesen, *Protection of metals* **2005**, *41*, 363–368.

[115] J. Wang, Y. Zhao, B. P. Setzler, S. Rojas-Carbonell, C. Ben Yehuda, A. Amel, M. Page, L. Wang, K. Hu, L. Shi, et al., *Nature Energy* **2019**, *4*, 392–398.

[116] H.-Y. Jung, S.-Y. Huang, B. N. Popov, *Journal of Power Sources* **2010**, *195*, 1950–1956.

[117] Y. Liu, S. Huang, D. Wang, H. Zhang, D. Shan, S. Peng, G. Shen, L. Wang, X. Wang, *ACS Applied Materials & Interfaces* **2022**, *14*, 15728–15735.

[118] P. Lettenmeier, R. Wang, R. Abouatallah, B. Saruhan, O. Freitag, P. Gazdzicki, T. Morawietz, R. Hiesgen, A. Gago, K. Friedrich, *Scientific Reports* **2017**, *7*, 44035.

[119] I. Pushkareva, A. Pushkarev, S. Grigoriev, P. Modisha, D. Bessarabov, *International Journal of Hydrogen Energy* **2020**, *45*, 26070–26079.

[120] R. J. Gilliam, J. Graydon, D. Kirk, S. Thorpe, *International Journal of Hydrogen Energy* **2007**, *32*, 359–364.

[121] D. R. Lide, *CRC handbook of chemistry and physics*, *Vol. 85*, CRC press, **2004**.

[122] D. Yang, Y. Tan, B. Li, P. Ming, Q. Xiao, C. Zhang, *Membranes* **2022**, *12*, 306.

[123] H. Khalid, M. Najibah, H. S. Park, C. Bae, D. Henkensmeier, *Membranes* **2022**, *12*, 989.

[124] M. Schalenbach, O. Kasian, K. J. Mayrhofer, *International journal of hydrogen energy* **2018**, *43*, 11932–11938.

[125] P. Fonda, Z. Wang, K. Yamazaki, Y. Akutsu, *Journal of materials processing technology* **2008**, *202*, 583–589.

[126] T. Uchikoshi, Y. Sakka, M. Yoshitake, K. Yoshihara, *Nanostructured materials* **1994**, *4*, 199–206.

[127] P. Trinke, P. Haug, J. Brauns, B. Bensmann, R. Hanke-Rauschenbach, T. Turek, *Journal of The Electrochemical Society* **2018**, *165*, F502.

[128] A. L. Santos, M. J. Cebola, J. Antunes, D. M. Santos, *Sustainability* **2023**, *15*, 11011.

[129] A. N. Colli, H. H. Girault, A. Battistel, *Materials* **2019**, *12*, 1336.

[130] G. Zhang, H. Wang, J. Yang, Q. Zhao, L. Yang, H. Tang, C. Liu, H. Chen, Y. Lin, F. Pan, *Inorganic chemistry* **2018**, *57*, 2766–2772.

[131] R. E. White, C. Walton, H. Burney, R. Beaver, *Journal of the Electrochemical Society* **1986**, *133*, 485.

[132] M. Quentmeier, B. Schmid, H. Tempel, R.-A. Eichel, *ACS Sustainable Chemistry & Engineering* **2024**, *12*, 3876–3885.

[133] V. Theußl, H. Weinrich, C. Heume, K. Dzieciol, B. Schmid, H. Kungl, H. Tempel, R.-A. Eichel, *ChemElectroChem* **2023**, *10*, e202300121.

[134] M. Carmo, D. L. Fritz, J. Mergel, D. Stolten, *International journal of hydrogen energy* **2013**, *38*, 4901–4934.

[135] S. Shen, K. Yang, G. Xu, S. Chen, C. Ortiz-Ledón, J. Duan, *MetalMat* **2024**, e28.

[136] K. Li, Q. Fan, H. Chuai, H. Liu, S. Zhang, X. Ma, *Transactions of Tianjin University* **2021**, *27*, 202–216.

[137] D. Gupta, A. Kafle, K. Garg, S. Mehta, T. C. Nagaiah, *Journal of Materials Chemistry A* **2024**.

[138] Y. Hori, H. Konishi, T. Futamura, A. Murata, O. Koga, H. Sakurai, K. Oguma, *Electrochimica acta* **2005**, *50*, 5354–5369.

[139] H. Becker, J. Murawski, D. V. Shinde, I. E. Stephens, G. Hinds, G. Smith, *Sustainable Energy & Fuels* **2023**, *7*, 1565–1603.

[140] Y. i. Hori, *Modern aspects of electrochemistry* **2008**, 89–189.

[141] Y. Lei, Z. Wang, A. Bao, X. Tang, X. Huang, H. Yi, S. Zhao, T. Sun, J. Wang, F. Gao, *Chemical Engineering Journal* **2023**, *453*, 139663.

[142] B. Endrődi, G. Bencsik, F. Darvas, R. Jones, K. Rajeshwar, C. Janáky, *Progress in Energy and Combustion Science* **2017**, *62*, 133–154.

[143] M. Quentmeier, B. Schmid, H. Tempel, H. Kungl, R.-A. Eichel, *ACS Sustainable Chemistry & Engineering* **2023**, *11*, 679–688.

[144] Y. Chen, F. Mojica, G. Li, P.-Y. A. Chuang, *International Journal of Energy Research* **2017**, *41*, 2365–2373.

[145] V. V. Fedorov, *Theory of optimal experiments*, Elsevier, **2013**.

[146] K. Siebertz, T. Hochkirchen, D. van Bebber, *Statistische versuchsplanung*, Springer, **2010**.

[147] H. Bandemer, A. Bellmann, *Statistische Versuchsplanung*, Springer, **1994**.

[148] H. Robbins, **1952**.

[149] F. Felsen, K. Reuter, C. Scheurer, *Chemical Engineering Journal* **2022**, *433*, 134121.

[150] C. Kunkel, F. Rüther, F. Felsen, C. W. Pare, A. Terzi, R. Baumgarten, E. Gioria, R. Naumann d'Alnoncourt, C. Scheurer, F. Rosowski, et al., *ACS Catalysis* **2024**, *14*, 9008–9017.

[151] Y. Su, X. Wang, Y. Ye, Y. Xie, Y. Xu, Y. Jiang, C. Wang, *Chemical Science* **2024**, *15*, 12200–12233.

[152] Z. Zheng, Z. Rong, N. Rampal, C. Borgs, J. T. Chayes, O. M. Yaghi, *Angewandte Chemie International Edition* **2023**, *62*, e202311983.

[153] D. A. Boiko, R. MacKnight, B. Kline, G. Gomes, *Nature* **2023**, *624*, 570–578.

[154] H. I. Lee, M. Mehdi, S. K. Kim, H. S. Cho, M. J. Kim, W. C. Cho, Y. W. Rhee, C. H. Kim, *Journal of Membrane Science* **2020**, *616*, 118541.

List of Figures

1.1 Optimization potentials (colored areas) of key performance indicators (KPI) for next generation alkaline water (AWE, red squares) and CO_2 to CO (blue circles) electrolyzers. Net charts indicate the technology-specific current status of the individual KPIs on the scale of the targeted optimization goals for: current density, lifetime, energy efficiency, product purity, and transient operation. State-of-the-art values are dimensionless plotted against KPI values expected in the future.[24,27] 5

1.2 Stray current formation through parallel tubing for common electrolyte feed in two different electrochemical systems: (a) electrochemical stack with bipolar plate that galvanically connects two cells, thereby serially building up the total electrochemical stack potential and (b) parallel operating cells that are galvanically isolated with electric fields freely aligned with each other. 9

2.1 Sensing methods applied: (a) two-terminal sensing (2TS), (b) four-terminal sensing via heat exchanger inlet of the current collector ($4TS_{cc}$), and (c) four-terminal sensing via contact frame ($4TS_{frame}$). For clarity, only the working electrode (WE) and sense electrode (S) connections are depicted. 21

2.2 Schematic illustration of different designs of the conductive element. The conductive element is required for four-terminal sensing via the contact frame. 22

2.3 Schematic illustration of experimental setup for potential difference measurements between two electrochemical flow cells. An ionic 4-point measurement was developed by implementing four reference electrodes. Potential differences were measured between neighboring electrodes (green line) to determine stray currents (red line) between parallel operated cells. 24

2.4 Schematic illustration of (a) two parallel, galvanically isolated flow cells with common electrolyte supply and (b) corresponding 2-cell equivalent circuit model. (c) Simplified equivalent circuit model for N parallel cells. 26

2.5 Schematic illustration of experimental setup for investigation of metal ion contamination risk of different electrolyte solutions in contact with stainless steel. The electrolytes were continuously circulated through a AISI 316Ti (EN 1.4571) stainless steel pipe with a contact area $A_{contact}$ of 20 cm^2 at 20 ml/min over 7 d. 29

3.1 Images of the developed high-throughput flow cell: (a) front view, (b) rear view, and (c)+(d) side views. 35

3.2 Image of the opened high-throughput flow cell in (a) finite-gap configuration and (b) zero-gap configuration. Schematic representation of the cross-section in (c) finite-gap configuration and (d) zero-gap configuration. 37

3.3 Effect of diaphragm activation tested with Zirfon UTP 220 and AWE in finite-gap configuration: (a) polarization curves and (b) electrochemical impedance spectroscopy data with activated (24 h pre-saturation in 6 M KOH) and non-activated diaphragm. Measurements were conducted at 20 °C with 6 M KOH and a flow rate of 50 mL/min. Prior to each measurement, the cell was conditioned at 0.5 A for 1 h. Reference data were recorded with a commercial flow cell under comparable conditions[2]. 39

3.4 Effect of flat gasket usage: (a) schematic cross-section with labeled flat gasket and (b) polarization curves with and without flat gasket. Measurements were conducted at 20 °C with a flow rate of 50 mL/min. Prior to each measurement, the cell was conditioned at 0.5 A for 1 h. 41

3.5 Finite-gap AWE tested at elevated operating temperatures. (a) polarization curves, (b) electrochemical impedance spectroscopy data, (c) temperature-dependent cell resistances derived from polarization curves $R_{c,pol}$ and electrochemical impedance spectroscopy results $R_{c,EIS}$, and (d) difference between cell resistance data sets ΔR_c. Measurements were conducted at 20, 40, and 60 °C with 6 M KOH and a flow rate of 50 mL/min. Prior to each measurement, the cell was conditioned at 500 mA/cm^2 for 1 h. 43

3.6 Finite-gap AWE operated in 3-electrode configuration. Cyclic voltammetry (0.2 mV step size) conducted within the (a) cathode potential range and (b) anode potential range at different scan rates of 5, 10, 15, and 20 mV/s. Oxidation and reduction peak-to-peak separation of scans within (c) cathode potential range and (d) anode potential range. Measurements were conducted using Hg/HgO reference electrode and Zirfon UTP 220 in 6 M KOH at 25 °C. 44

3.7 Zero-gap AEM WE tested with different sensing methods: two-terminal sensing (2TS), four-terminal sensing via current collectors ($4TS_{cc}$), and four-terminal sensing via contact frame ($4TS_{frame}$) with conductive element $D_{1,Ni/Ni}$. (a) Polarization curves, (b) electrochemical impedance spectroscopy data, (c) cell resistances derived from polarization curves $R_{c,pol}$, and (d) cell resistances derived from electrochemical impedance spectroscopy data $R_{c,EIS}$. Measurements were conducted at 20 °C with 1 M KOH and a flow rate of 40 mL/min. Prior to each measurement, the cell was conditioned at 1000 mA/cm^2 for 1 h. 47

3.8 Zero-gap AEM WE tested at elevated operating temperatures using $4TS_{frame}$ with conductive element $D_{1,Au/Ni}$. (a) Polarization curves, (b) electrochemical impedance spectroscopy data, (c) cell resistances derived from polarization curves $R_{c,pol}$, (d) and cell resistances derived from electrochemical impedance spectroscopy data $R_{c,EIS}$. Measurements were conducted at 20, 40, and 60 °C with 20 µm PiperION membrane, 1 M KOH, and a flow rate of 40 mL/min. Prior to each measurement, the cell was conditioned at 2000 mA/cm^2 for 1 h. Reference polarization curves were recorded at 60 °C with 1 M KOH and Aemion+™ or Sustainion® membrane[119]. 49

3.9 Zero-gap AEM WE using $4TS_{frame}$ tested different conductive element designs. (a) Polarization curves, (b) electrochemical impedance spectroscopy data, (c) cell resistances derived from polarization curves $R_{c,pol}$, and (d) cell resistances derived from electrochemical impedance spectroscopy data $R_{c,EIS}$. Measurements were conducted at 60 °C with 1 M KOH and a flow rate of 40 mL/min. Prior to each measurement, the cell was conditioned at 2000 mA/cm^2 for 1 h. 51

3.10 Zero-gap AEM WE reproducibility study using $4TS_{frame}$ with D_4. Polarization curve represents the mean of three individual experiments. Measurements were conducted at 60 °C with 1 M KOH and a flow rate of 40 ml/min. Prior to each measurement, the cell was conditioned at 2000 mA/cm^2 for 1 h. 52

3.11 Zero-gap AEM WE PiperION membrane screening using $4TS_{frame}$ with D_4. (a) Polarization curves, (b) electrochemical impedance spectroscopy data, (c) cell resistances derived from polarization curves $R_{c,pol}$, (d) and cell resistances derived from electrochemical impedance spectroscopy data $R_{c,EIS}$. Measurements were conducted with 20, 40, and 60 µm PiperION membrane at 60 °C with 1 M KOH and a flow rate of 40 mL/min. Prior to each measurement, the cell was conditioned at 2000 mA/cm^2 for 1 h. 54

3.12 Zero-gap AWE tested with different sensing methods: two-terminal sensing (2TS), four-terminal sensing via current collectors ($4TS_{cc}$), and four-terminal sensing via contact frame ($4TS_{frame}$) with conductive element D_4. (a) Polarization curves and (b) cell resistances derived from polarization curves $R_{c,pol}$. Measurements were conducted at 20 °C with 6 M KOH and a flow rate of 50 mL/min. Prior to each measurement, the cell was conditioned at 500 mA/cm^2 for 1 h. 55

3.13 Zero-gap AWE tested at elevated operating temperatures using $4TS_{frame}$ with D_4. (a) Polarization curves, (b) electrochemical impedance spectroscopy data, (c) cell resistances derived from polarization curves $R_{c,pol}$, and (d) cell resistances derived from electrochemical impedance spectroscopy data $R_{c,EIS}$. Measurements were conducted at 20, 40, and 60 °C with 6 M KOH and a flow rate of 50 mL/min. Prior to each measurement, the cell was conditioned at 500 mA/cm^2 for 1 h. The reference polarization curve was recorded with a comparable system at 80 °C with 7 M KOH[124]. 57

3.14 Schematic cross-section of PEEK inlays. (a) Original inlay design and (b) modified inlay designs. Modified inlays are provided with a chamfer of 15, 30, or 45°. 59

3.15 Effect of modified PEEK inlays on signal noise with finite-gap AWE. (a) Polarization curves and (b) cell resistances derived from electrochemical spectroscopy data $R_{c,EIS}$. Measurements were conducted with original and modified inlays with different chamfer angles of 15, 30, and 45°at 20°C with 6 M KOH and a flow rate of 50 mL/min. Prior to each measurement, the cell was conditioned at 500 mA/cm^2 for 1 h. 60

3.16 Schematic illustration of (a) original flow field design providing parallel fluid channels and (b) modified flow field design providing a single meandering fluid channel. Modified design prevents fluid in flow field channels to be excluded from the reaction by PEEK inlay (right). 61

3.17 Images of precious metal coatings on the current collectors. (a) Pt was coated on anodic current collector and (b) Au was coated on cathodic current collector. 63

3.18 Precious metal-coated current collectors tested with zero-gap AEM WE using $4TS_{cc}$. Measurements were conducted at 60 °C with PiperION® membrane, 1 M KOH, and a flow rate of 40 mL/min. Prior to each measurement, the cell was conditioned at 2000 mA/cm^2 for 1 h. Reference polarization curves were recorded under comparable conditions at 60 °C with 1 M KOH and Aemion+^{TM} or Sustainion® membrane[119]. 64

3.19 Overview of literature data on electrical resistivity of metals relevant for current collectors in electrochemistry[121,125]. 65

3.20 Schematic cross-sections of finite-gap design. (a) Original housing with 12 mm and (b) modified housing with 2 mm electrode-separator distance. 67

3.21 Effect of modified finite-gap design on cell performance. Cell voltages were estimated for an electrode-separator distance of 5 and 2 mm based on experimental results. Experimental measurement was conducted at 20 °C with 6 M KOH and a flow rate of 50 mL/min. Reference polarization curve was recorded at 25 °C with 6 M KOH[2]. . . . 68

4.1 Effect of deliberately increased cell voltage difference $\Delta U = U_d - U_s$ on cell current I_s. I_s (left axis) at a constant cell voltage $U_s = 1.5$ V at all times with moving average (red line) and ΔU (right axis) are depicted as a function of time t. $Cell_d$ voltage U_d was increased by $\Delta U_d = \Delta U = 0.1$ V every 15 min starting from $U_d = U_s = 1.5$ V up to $U_d = 2.5$ V. After 3.5 h ΔU was reset to 0 V. 76

4.2 Potential difference of adjacent anodes ΔE_{aa} (blue line) and adjacent cathodes $-\Delta E_{cc}$ (red line). Current density i_d of $cell_d$ was stepwise increased from 1 up to 500 mA/cm^2. $Cell_s$ was constantly operated at $i_s = 100$ mA/cm^2. Measurements were conducted at 25 °C. 77

4.3 Schematic representation of the distance-dependent electrochemical potential E(x) for different operating conditions showing measured potential differences between adjacent cathodes (red solid line) and adjacent anodes (blue solid line). The potential distributions are shown for the steady state cell $E_s(x)$ (black solid line: (a) & (b) $i_s = 100\,mA/cm^2$) and dynamic cell $E_d(x)$ (black dashed line: (a) $i_d = 10\,mA/cm^2$ and (b) $i_d = 500\,mA/cm^2$). The potential distribution is composed of the electrode overpotentials I - V. 79

4.4 Potential difference of (a) adjacent anodes ΔE_{aa} and (b) adjacent cathodes ΔE_{cc} at elevated operating temperatures. Current density i_d of $cell_d$ was stepwise increased from 1 up to $500\,mA/cm^2$. $Cell_s$ was constantly operated at $i_s = 100\,mA/cm^2$. Measurements were conducted at 25, 40, and 60 °C. 80

4.5 Ionic tube resistance R_t as a function of (a) tube extension length $l_{t,ext}$ and (b) total tube length l_t at elevated operating temperatures. Ionic tube resistance R_t was experimentally determined for $l_{t,ext}$ values of 10, 20 and 30 cm (a, squares) at 25 °C. Theoretical values of R_t at 25, 40 and 60 °C (b) were calculated based on specific conductivity values ρ of 6 M KOH taken from literature[120]. During the experiment, $R_t = 410\,\Omega$ was measured with the experimental setup (cf. Figure 2.3) of this study (dashed-dotted line). 81

4.6 Total stray current I_{sc} between two commercial cells operated with AWE. Current density i_d of $cell_d$ was stepwise increased from 1 up to $500\,mA/cm^2$. $Cell_s$ was constantly operated at $i_s = 100\,mA/cm^2$. I_{sc} was determined based on ΔE measurements and R_t data at 25, 40, and 60 °C. 83

4.7 Effect of total tube length and inner tube diameter on total stray current between two AWE cells for $i_d = 100\,mA/cm^2$ and $i_s = 500\,mA/cm^2$. Conditions of experimental setup are marked at $l_t = 32.25\,cm$ and $d_i = 4\,mm$ (red triangle). . . 84

4.8 Validation of equivalent circuit model of two parallel cells. Comparison of estimated stray current (red line) with experimentally determined stray currents (black squares) between two commercial cells (Micro Flow Cell® from ElectroCell A/S) operated with AWE. 85

4.9 Effect of total cell number (a) on cell stray current $I_{sc,k}$ with constant current density difference $\Delta i = 100\,mA/cm^2$, (b) on cell stray current $I_{sc,k}$ with constant boundary cell current densities ($i_1 = 100\,mA/cm^2$, $i_N = 1000\,mA/cm^2$), (c) on boundary cell stray currents $I_{sc,1}$ and $|I_{sc,N}|$ as well as (d) on total system stray current $I_{sc,system}$. Stray currents were estimated with a tube resistance $R_t = 200\,\Omega$ and cell resistance $R_c = 0.144\,\Omega$. 87

4.10 Effect of tube design factor on total system stray current. Stray currents were estimated for different current density differences Δi of 20, 60, and $100\,mA/cm^2$. Equivalent circuit model was built with a total cell number N of 16 cells, tube resistance R_t of $200\,\Omega$, and cell resistance R_c of $0.144\,\Omega$. 90

4.11 Effect of tube resistance on total system stray current for different tube design factors f_d of 0.1, 0.3, and 0.5. Equivalent circuit model was built with a total cell number N of 16 cells, current density difference Δi of $100\,mA/cm^2$, and cell resistance R_c of $0.144\,\Omega$. 91

5.1 Metal ion contamination of (a) iron Fe and (b) titanium Ti in 6 M KOH due to contact with AISI 316Ti (EN 1.4571) stainless steel. Analyzes were conducted with ICP-OES. Fe and Ti detection limit in 6 M KOH is 0.36 and $1.25 \cdot 10^{-6}$mol/L, respectively. Nickel Ni, chromium Cr, and molybdenum Mo ions were not detected. 97

5.2 Metal ion contamination of iron Fe in 2 M $KHCO_3$ due to contact with AISI 316Ti (EN 1.4571) stainless steel. Analyzes were conducted with ICP-OES. Fe detection limit in 2 M $KHCO_3$ is $3.58 \cdot 10^{-6}$mol/L. Nickel Ni, chromium Cr, molybdenum Mo, and titanium Ti ions were not detected. 98

5.3 Metal ion contamination of iron Fe in deionized H_2O due to contact with AISI 316Ti (EN 1.4571) stainless steel. Analyzes were conducted with ICP-OES. Fe detection limit in deionized H_2O is $0.54 \cdot 10^{-6}$mol/L. Nickel Ni, chromium Cr, molybdenum Mo, and titanium Ti ions were not detected. 99

5.4 Overview of metal ion contamination after 7 d in various electrolyte solutions and deionized H_2O due to contact with AISI 316Ti (EN 1.4571) stainless steel. Analyzes were conducted with ICP-OES. Contamination limit of Fe ions for electrochemical CO_2 reduction (red line)[138]. 100

6.1 3D layout of the 16-fold parallelized high-throughput test system for electrolysis processes. 105

6.2 Simplified flow sheet of the HT system for one electrolyzer cycle. Abbreviations: temperature indicator controller (TIC), flow indicator controller (FIC), and quality indicator (QI). QI indicates the conductivity sensor. The depicted symbols are according to ISO 10628-1. 106

6.3 Reproducibility test with the 4-cell HT prototype under nominally identical conditions. All cells were operated with alkaline water electrolysis in zero-gap configuration using Ni meshes and Zirfon UTP 220 in 6 M KOH at 20 °C. (a) Polarization curves were recorded with a scan rate of 50 mA/s and a step size of 20 mA. (b) Chronopotentiometries were performed at 100 mA/cm^2 for one hour. 109

6.4 Workflow for (a) a one-dimensional sequential single-step experimentation approach and (b) a DoE workflow implemented in a HT system with n parallelized cells. 113

6.5 Comparison of workflow timeframes for 16 iterations of a 100 h experiment in a single cell setup vs. 16 cells running for 100 h in a 16-fold HT system. The calculation is based on a 8 h work day. Non-working days were not considered for the calculations. 114

A.1 The effect of conditioning time on cell performance tested with zero-gap AEM WE. (a) Polarization curves as well as (b) cell voltage U at 2000 mA/cm^2 and cell resistance R derived from polarization curves. Cell conditioning was conducted at 1000 mA/cm^2. Measurements were conducted at 20 °C and 1 barg with 40 ml/min at the site of the project partner hte GmbH. 127

B.1 Photo of the flow field with a 1 mm wide groove. The flow field has a thickness of 1.5 mm. All dimensions are in mm. 129

B.2 (a) Cell voltage U as well as (b) anode and cathode electrode potential E vs. SHE (b) as a function of current density i. Experiment conducted in a commercially available Micro Flow Cell® purchased from ElectroCell A/S with AWE at 25 °C. Data were recorded using a linear scan (scan rate = 1 mA/s, step size = 2 mA). Dashed lines indicate the standard cell voltage of the overall reaction U^0 = 1.23 V as well as standard electrode potentials of the oxygen evolution reaction E_a^0 = 0.336 V and the hydrogen evolution reaction E_c^0 = -0.894 V for AWE. 130

B.3 Effect of deliberately increased cell voltage difference $\Delta U = U_d - U_s$ on cell current I_s. Repeat measurement at elevated start voltages $U_s = U_d$ = 1.7 V. I_s (left axis) at a constant cell voltage U_s = 1.7 V at all times with moving average (red line) and ΔU (right axis) are depicted as a function of time t. $Cell_d$ voltage U_d was increased by $\Delta U_d = \Delta U$ = 0.1 V every 15 min starting from $U_d = U_s$ = 1.7 V up to U_d = 2.7 V. After 3.5 h ΔU was reset to 0 V. 131

B.4 Effect of deliberately increased cell voltage difference $\Delta U = U_d - U_s$ on cell current I_s. Repeat measurement at elevated start voltages $U_s = U_d$ = 2 V. I_s (left axis) at a constant cell voltage U_s = 2 V at all times with moving average (red line) and ΔU (right axis) are depicted as a function of time t. $Cell_d$ voltage U_d was increased by $\Delta U_d = \Delta U$ = 0.1 V every 15 min starting from $U_d = U_s$ = 2 V up to U_d = 3 V. . . 132

B.5 Experimental setup to determine the ionic tube resistance R_t as a function of the length of the installed tube extension $l_{t,ext}$. Tube extensions with defined lengths $l_{t,ext}$ of 10, 20, and 30 cm were installed between both cells. R_t was measured with potentiostatic electrochemical impedance spectroscopy. 132

C.1 Metal ion contamination of (a) iron Fe, (b) nickel Ni, (c) chromium Cr, (d) molybdenum Mo, and (e) titanium Ti in 6 M HCl due to contact with AISI 316Ti (EN 1.4571) stainless steel. Analyzes were conducted with ICP-OES. Fe, Ni, Cr, Mo, and Ti detection limits in 6 M HCl are $5.4{\cdot}10^{-7}$, $6.8{\cdot}10^{-7}$, $9.6{\cdot}10^{-7}$, $4.2{\cdot}10^{-7}$, and $2.1{\cdot}10^{-7}$ mol/L, respectively. 140

C.2 Metal ion contamination of (a) iron Fe, (b) nickel Ni, (c) chromium Cr, (d) molybdenum Mo, and (e) titanium Ti in 2 M H_2SO_4 due to contact with AISI 316Ti (EN 1.4571) stainless steel. Analyzes were conducted with ICP-OES. Fe, Ni, Cr, Mo, and Ti detection limits in 2 M H_2SO_4 are $5.4{\cdot}10^{-7}$, $6.8{\cdot}10^{-7}$, $9.6{\cdot}10^{-7}$, $4.2{\cdot}10^{-7}$, and $2.1{\cdot}10^{-7}$ mol/L, respectively. 141

C.3 Metal ion contamination of (a) iron Fe, (b) nickel Ni, (c) chromium Cr, and (d) titanium Ti in 2 M NaCl due to contact with AISI 316Ti (EN 1.4571) stainless steel. Analyzes were conducted with ICP-OES. Fe, Ni, Cr, and Ti detection limits in 2 M NaCl are $3.6{\cdot}10^{-6}$, $3.4{\cdot}10^{-6}$, $3.8{\cdot}10^{-6}$, and $1.3{\cdot}10^{-6}$ mol/L, respectively. 142

List of Tables

2.1 Chemicals for electrolyte preparation. 15
2.2 Materials for finite-gap and zero-gap AWE experiments. . 16
2.3 Materials for zero-gap AEM WE experiments. 17
2.4 Gaskets for HT flow cell assembly. 17
2.5 Nominal composition of Ti grade 5 (Ti-6Al–4V) in wt. %.[94] 17
2.6 Materials for stray current experiments. 18
2.7 Composition of AISI 316Ti austenitic steel (EN 1.4571, X6CrNiMo17-12-2) in wt. %.[96] 18

A.1 Roughness factor f_R of smooth Ni foil calculated based on reduction peak of an anodic cyclic voltammetry scan (Ni(III) to Ni(II) transition) for different scan rates v. 128

B.1 Current density distribution in (mA/cm^2) with constant cell-to-cell current density difference $\Delta i = 100\,mA/cm^2$ for increasing total number of cells N. 136
B.2 Current density distribution in (mA/cm^2) with constant current densities of the boundary cells $i_1 = 100\,mA/cm^2$ and $i_N = 1000\,mA/cm^2$ for increasing total number of cells N. 137